University of Nottingham
UK | CHINA | MALAYSIA

Failure analysis and mechanical behaviors of metamaterials

Thesis submitted to the University of Nottingham for the degree of **Doctor of Philosophy, March 2023.**

Akash Singh Bhuwal

14341885

Supervised by

Dr. Walid Tizani
Prof. Ian Ashcroft
Dr. Tao Liu
Prof. Wei Sun

List of publications

Journals Pblications:

1. **A.S. Bhuwal**, T. Liu, I. Ashcroft, W. Sun, (2021). Localization and coalescence of imperfect planar FCC truss lattice metamaterials under multiaxial loadings. *Mechanics of Materials*, Vol. 160, 103996. https://doi.org/10.1016/j.mechmat.2021.103996.

2. **A.S. Bhuwal**, Y. Pang, T. Liu, I. Ashcroft, W. Sun, (2023). Data-driven discovery of quasi-disordered mechanical metamaterials failed progressively. *Journal of the Mechanics and Physics of Solids*, Vol. 175, 105294.

   https://doi.org/10.1016/j.jmps.2023.105294.

3. **A.S. Bhuwal**, Y. Pang, T. Liu, I. Ashcroft, W. Sun, (2023). Creep characterization of Inconel 718 lattice metamaterials manufactured by laser powder bed fusion. *Advanced Engineering Materials*.

   https://doi.org/10.1002/adem.202300643.

International conferences (Not included in thesis)

1. **A.S. Bhuwal**, Y. Pang, T. Liu, I. Ashcroft, W. Sun. (2022). Data-driven design of high ductile metamaterials under uniaxial tension. In

Proceedings *Eighth International Conference on Structural Engineering, Mechanics and Computation (SEMC 2022)*, Cape Town, South Africa. https://doi.org/10.1201/9781003348450

Abstract

In recent years, mechanical metamaterials have been explored for their tunable nature with the continual development of Additive Manufacturing (AM) technologies. As a result, the failure mechanisms of the metamaterials and their mechanical behaviours under different boundary and environmental conditions have been investigated. Firstly, failure mechanisms of AM originated imperfections in the metamaterials have been investigated. In this, three types of imperfection have been considered in the numerical modelling of the metamaterials: distorted struts, missing struts, and strut diameter variation. Then a novel numerical framework was developed to overcome computational difficulties within the existing numerical approaches beyond the elastic region. Three modes of microscopic localisation were observed in metamaterials before failure: crushing band, shear band and void coalescence. The results showed that a clear separation exists between the three modes of localisation depending upon the type and level of defects and loading condition. Under compressive loading, all metamaterials failed due to the crushing band; the distorted lattices are prone to shear band localisation with increased distortion, whereas missing lattices majorly fail due to void coalescence at high missing struts defect.

The study on imperfect metamaterials has suggested that it can exhibit either ductile, damage-tolerant behaviours or sudden, catastrophic failure

mode, depending on the distribution of the introduced disorderliness. Thus a data-driven approach has been developed, combining deep-learning and global optimisation algorithms, to tune the distribution of the disorderliness/ imperfections to achieve damage-tolerant metamaterial designs. A case study on the metamaterial created from a periodic Face Centred Cubic (FCC) lattice has demonstrated that the optimised metamaterials can generate high-quality designs with improved ductility, enabling them to sustain larger deformations without failure at a lower cost to strength and stiffness. This has been validated by an experimental study on an optimised metamaterial design. The results showed that the optimized designs can achieve up to 100% increase in ductility at the expense of less than 5% stiffness and 8-15% tensile strength.

Finally, the creep behaviour of Inconel 718 metamaterial has been investigated at an elevated temperature to understand the effects of the microstructural defects. A Kachanov's damage modelling has been used to predict the creep performance of the metamaterials. The analysis and experimental results indicated that the creep resistance of the metamaterials is dependent on the microstructure and loading conditions. The creep behaviour of the metamaterials is significantly different from that of the bulk material due to their complex microstructure.

Overall, this study contributes to the development of mechanical metamaterials with improved mechanical properties using AM technologies. The neural network-based data-driven methodology offers a promising avenue for designing high-quality metamaterials that are cost-effective and have desirable mechanical properties. The results of this study have significant implications for various applications, including structural engineering, biomechanics, and aerospace engineering, including in understanding and designing for the creep behavior of Inconel 718 metamaterials.

Acknowledgements

Ph.D. study over the past four years has been a truly changing experience for me and it would not have been completed without the support that I received from many people. Thus, I would like to thank these people who provide direct supports to the successful completion of my dissertation.

First and foremost, I would like to express my sincere gratitude to Prof. Wei Sun for making the past 4 years much more enjoyable and keeping me sane throughout the whole process. The study opportunities he has offered me at University of Nottingham are truly invaluable. I also want to give my deepest appreciation to my supervisor Dr. Tao Liu for always being there when I needed his support, reviewing my progress constantly, and guiding me through my PhD studies. He has not only provided me with step-by-step guidance targeting journal publications but also shared the ups and downs of the Ph.D. study with me. I would not have survived my Ph.D. program without his academic, emotional and financial supports. I would also like to extend my thanks to my supervisors Prof. Ian Ashcroft and Dr. Walid Tizani for providing all the supports and resources needed at the University. Additionally, a special thanks to Dr. Yong Pang for assisting me on experimentation part, with his support the work become much easier to complete.

Finally, I would like to say a heartfelt thanks to my parents and wife. My personal developments would not have been possible without their supports, loves and cares from my family. I wish my parents and wife can accept this dissertation as a gift for their enduring love.

Contents

List of Tables

List of Figures

Abbreviations

2D Two dimensional.

3D Three dimensional.

AM Additive Manufacturing.

ANN Artificial Neural Networks.

BCC Body Centred Cubic.

CAD Computer Aided Design.

CFD Computational Fluid Dynamics.

CNN Convolutional Neural Networks.

DIC Digital image correlation.

DMLS Direct Metal Laser Sintering.

EDM electrical discharge machining.

EDS Energy-dispersive X-ray spectroscopy.

FCC Face Centred Cubic.

FE Finite Element.

FEA Finite Element Analysis.

FFNN feed-forward neural networks.

H-S Hashin-Shtrikman.

LPBF Laser powder bed fusion.

LTS local tensile strain.

LVDT linear voltage differential transformer.

MSE Mean Square Error.

PBCs periodic boundary conditions.

QTM Quasi-disordered Truss metamaterial.

ReLU rectified linear activation function.

RNN recurrent neural networks.

RVE Representative Volume Element.

SA Simulated Annealing.

SDD silicon drift detector.

SEM Scanning Electron Microscopy.

SLM Selective Laser Melting.

SMP Shape Memory Polymer.

TBS Two bar specimens.

Nomenclature

$(\xi_1^i, \xi_2^i, \xi_3^i)$	local coordinates of i^th node
(x_1^i, x_2^i, x_3^i)	global coordinates of i^th node
α	degree of irregularity for nodal perturbation
β	random variable of uniform distribution probability distribution
η	degree of irregularity for missing struts
γ	degree of irregularity for strut thickness
κ	yield offset of parent material
λ_i	stretches and quantiles for loss function
$\mathbf{B}$	derivatives of shape function
$\mathbf{E}^0$	logarithmic strain tensor
$\mathbf{K}$	macroscopic stiffness tensor
$\mathcal{L}$	loss function
ω	creep damage parameter
$\overline{\rho}$	relative density
$\overline{\sigma_y}$	yield strength of parent material

$\overline{\sigma}$	parent material property stresses
$\overline{\varepsilon}$	parent material property strains
$\overline{E}$	Young's modulus of parent material
$\overline{k}$	spring constant
ρ	stress ratio
Σ	principal stress components
σ	stress vector
σ_{eq}	equivalent stress
σ_{true}, σ_{pred}	true and predicted stress vectors
ε	strains vector
ε_{true}, ε_{pred}	true and predicted strain vectors
A, η, m, M, ϕ, χ, δ	creep material constants
D	damage parameter
d, t	diameter and thickness of a strut
E^b_{eq}	equivalent logarithmic strain inside shear band
E_{eq}	equivalent logarithmic strain
F, G, H, I	Hill's material constants
h	height of a unit cell
J	cost function
L	height of RVE
l	length of a unit cell, neural network layers

n	hardening exponent of parent material
R	reaction force
r	minimum distance between two nodes
T	Triaxiality and Objective function
u_i	displacement vectors, $i \in (1, 2, 3)$
W	width of RVE

Chapter 1

Introduction

1.1 Background and Motivation

Over the last decade, Additive Manufacturing (AM) has advanced rapidly and begun to play an essential role in the production of metamaterials with complex microstructures. The metamaterials have materials properties close to the theoretical limits or far beyond that of conventional bulk materials. However, engineers face the difficult task of determining which optimised structure can meet the actual requirements of advanced devices and equipment in extreme service environments involving multi-physical coupling despite complex multi-physics constraints, specific availability of manufacturing processes, and material property limitations.

Recently, interest in manufacturing periodic or lattice structures has continuously increased due to highly customised properties. A lattice structure, also known as a cellular structure, is a three-dimensional arrangement of struts or beams that form a repeating pattern. The struts or beams can be made of a variety of materials, including metal, plastic, or even foam.

Before the advancement of AM, other orthodox manufacturing technologies like investment casting, deformation forming, brazing etc., are studied to produce periodic lattice geometries. Limitations of such techniques include the fitness of the structures and the actual cell geometry [19]. AM technologies have been developed over the years to produce three-dimensional objects directly from a digital model by adding materials without specialised tooling. Direct Metal Laser Sintering (DMLS) or Selective Laser Melting (SLM) can produce fine surface geometries like roughness value at 50 microns lattice structures using AM process for metal alloys. Because of this unique quality allows for tailored mechanical, thermal and biological properties in the diffusion of lattices, trusses, and periodic materials could be found [20]. In conjunction with lightweight properties, lattice structures also provide impact resistance, non-conducting heat properties and electromagnetic wave absorption [21–27].

The metamaterial design is an excellent choice for applications (see Figure 1.1) that require maximum stiffness while retaining lightweight, energy absorption [28], and high specific strength [29]. It applies to structural, functional, or ergonomic parts [30], as well as biomedical [31], thermal [32], and material properties improvement [33]. Commercial applications of metamaterials are also dependent on industrial preferences, such as a simple topology fabricated with different technology can exhibit fluctuated mechanical properties, and the same trend holds true for other lattice structure permeates such as height, unit size, fabrication materials, and post-processing. These structures have been boosted by commercial applications in a variety of fields, including for a patient-specific implant that not only recovers its structure under applied load but also exhibits adequate stiffness with surrounding tissues [34], as well as maintaining the stiffness of metallic medical implants to the bone [35]. As a result, these structures

were used to allow fluid in topology while avoiding stress shielding [36], as well as to facilitate osseointegration (the direct structural and functional connection between the living bone and surface of a load-bearing implant) via a large surface area to volume ratio [37].

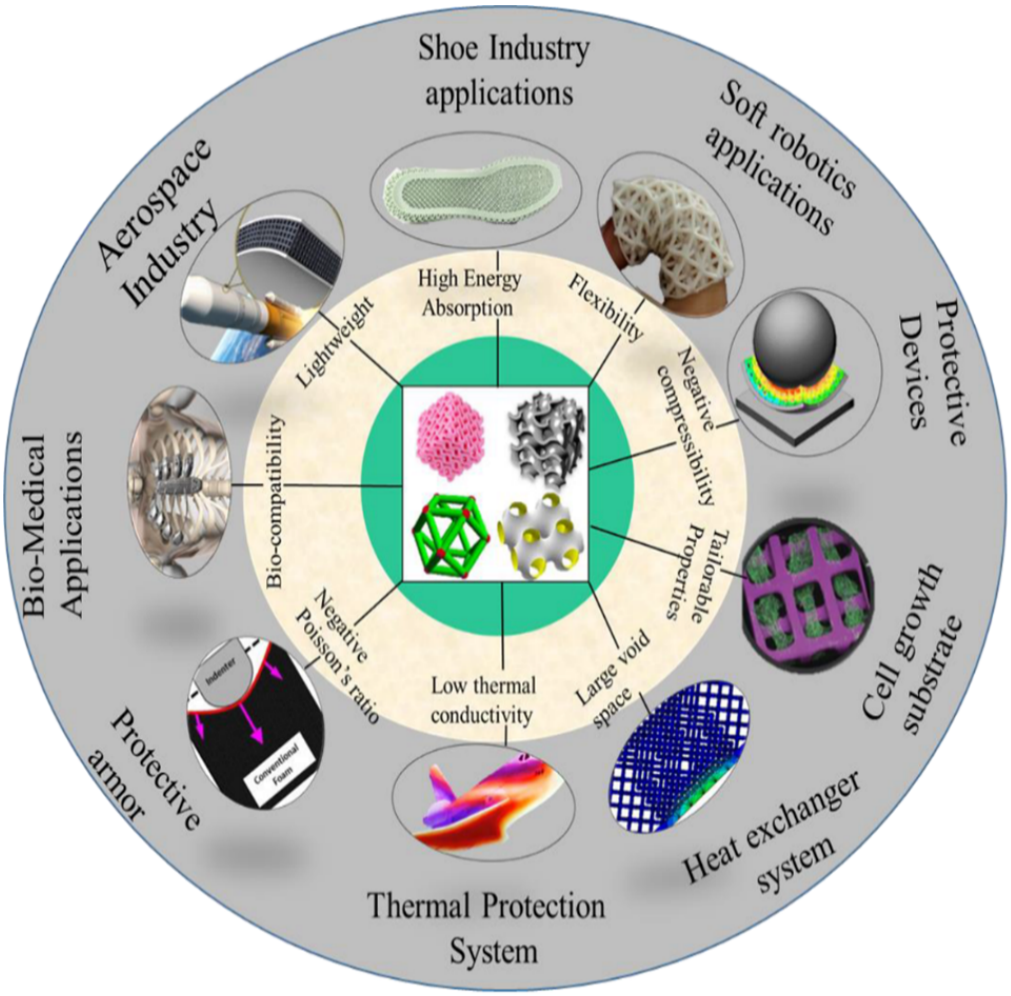

Figure 1.1: General applications of mechanical metamaterials [1]

Over the past years, the failure mechanisms, damage, and creep behaviours in metamaterials have been an extensively researched topic. The growth of damage in a lattice structure under remote loading is known to affect the mechanical performance of the material. Therefore, a better understanding of the failure mechanisms and mechanical characteristics is crucial to improve metamaterial designs. Furthermore, the mechanical behaviour of metamaterials containing disorderliness/defects is particularly important.

For example, metamaterials commonly fail due to geometrical/dimensional defects, surface defects, microstructure defects and mechanical defects such as holes, cracks and porosity. Therefore, it is essential to understand their effects on the general mechanical characteristics of the metamaterials.

This research project endeavours to fill the existing knowledge gap by exploring the reasons for failure and examining the mechanical behaviour of truss-lattice metamaterials subjected to various loading conditions. This thesis aims to investigate the impact of multi-axial loadings on metamaterials, notably after introducing disorders/defects into their structure. A neural network model is then introduced to enhance the mechanical performance of these metamaterials. Finally, the creep behaviour and failure mechanism of the metamaterial have been explored due to microstructure defects.

1.2 Objectives

This study aims to understand failure mechanisms and mechanical behaviors of the metamaterials. For our study, truss lattice metamaterials have been taken for investigation. The study can be classified into below categories:

- To numerically investigate macroscopic elastic-plastic behaviour and failure mechanisms of truss metamaterials with defects under multi-axial loading.
- To develop a data-driven framework to optimise the distribution of disorderliness to achieve damage tolerance metamaterial designs with the increase in ductility at the minor expense of stiffness and tensile

strength.

- To understand the creep behaviour and effects of microstructures of the metamaterials manufactured by Three dimensional (3D) printing technology. Inconel 718 has been investigated as parent material at an elevated temperature.

1.3 Thesis overview

Chapter 2 - The literature review provides an overview of the mechanical properties of metamaterials. Common metamaterials structures are described, including auxetic, origami & kirigami, multistable, topological and combinatorial metamaterials.

Chapter 3 - The methodology chapter provides an overview of the investigation of the mechanical properties of mechanical metamaterials developed using AM technologies. This chapter briefly describes the research design and procedures used to answer the research questions or hypotheses, also objectively discusses about limitations.

Chapter 4 - The localisation and coalescence chapter overviews failure mechanisms of imperfect planar Face Centred Cubic (FCC) metamaterial under multi-axial loading. Three types of imperfection are considered in the numerical modelling: distorted struts, missing struts, and strut diameter variation. The chapter highlights modes of microscopic localisation in perfect and imperfect lattices before failure: crushing band, shear band and void coalescence, and presents numerical evidence that a clear separation exists between the three modes of localisation depending upon the type and level of defects, as well as the stress triaxiality. This chapter serves as the foundation to implement the disorderliness of lattice struts to enhance

the mechanical properties of the metamaterials.

Chapter 5 – A neural network based methodology is developed. I have created Quasi-disordered Truss metamaterial (QTM) by introducing spatial coordinate perturbations or strut thickness variations to the perfect, periodic truss lattices. This chapter explains that the QTMs can exhibit either ductile, damage-tolerant behaviours or sudden, catastrophic failure mode, depending on the distribution of the introduced disorderliness. Furthermore, a data-driven approach has been developed, combining deep-learning and global optimisation algorithms, to tune the distribution of the disorderliness to achieve damage-tolerant QTM designs.

Chapter 6 - To understand the creep behavior of Laser powder bed fusion (LPBF) Inconel 718, Body Centred Cubic (BCC) metamaterials were fabricated for creep test at 650 ℃, and a Kachanov's damage model has been developed to predict the creep performance of the metamaterials under different loading conditions. Additionally, microstructural characterisation has been performed with Scanning Electron Microscopy (SEM) to identify critical microstructure defects affecting the failure mechanisms and creep behaviors of the metamaterials.

Chapter 7 - A summary and discussion of the key findings from the thesis and suggested future work to develop the field of mechanical metamaterials further.

Chapter 2

Literature Review

2.1 Mechanical properties of metamaterials

Metamaterials are designed materials that are made of both natural and artificial components, hence providing unique combinations of physical characteristics. These features can be found in nature since metamaterials are constructed materials mostly inspired by nature. Because of their exceptional mix of features, metamaterials may be used in a wide range of applications, including bio-medical industries, protective devices as energy dissipator devices, and many more [38] (see Figure 1.1). The structure of the material and the constituent/parent materials are the two primary components that make up metamaterials. Depending on metamaterial designs, the structure of the material may vary from simple lattices to intricate networks of linked pieces [39].

The mechanical characteristics of a metamaterial are often what defines it, and these qualities are influenced by the sort of component materials employed, the structure of the material, and the production method. The

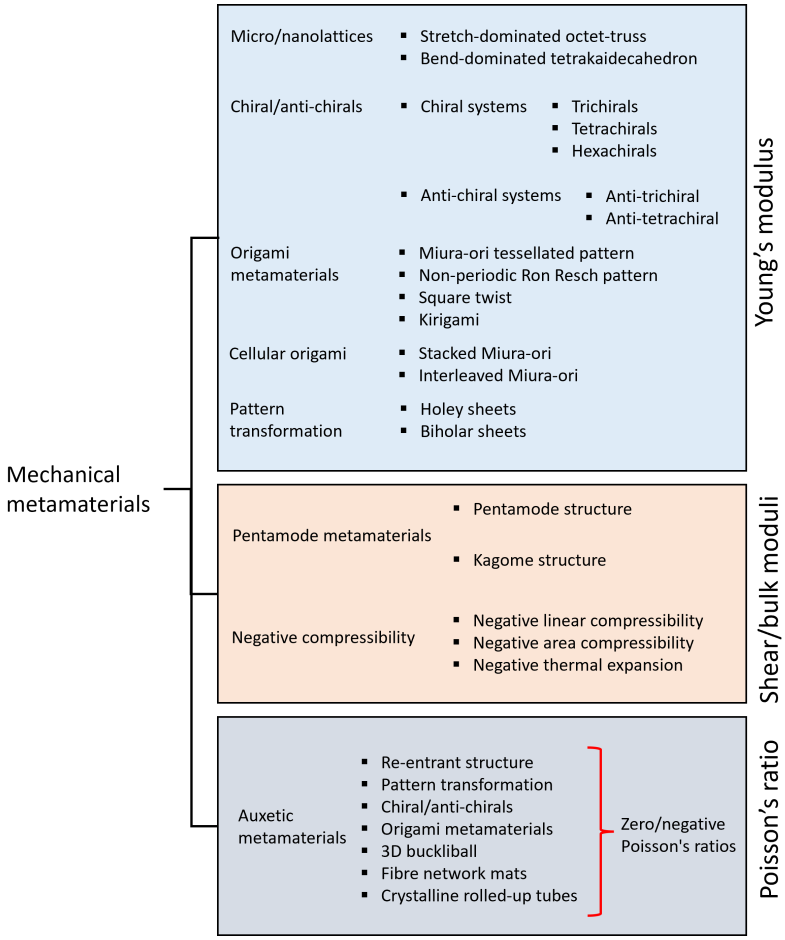

Figure 2.1: Basic classification of mechanical metamaterials [2]

static properties and the dynamic properties of metamaterials are the two primary categories that may be used to classify the mechanical characteristics of metamaterials [40]. The behavior of a material in response to external demands that are held constant is referred to as its static properties, while the behavior of a material in response to external stresses that vary over time is referred to as its dynamic properties. In addition, the mechanical characteristics of metamaterials can also be broken down into three distinct classifications, namely, stiffness, toughness, and strength. The capacity of a material to resist deformation is referred to as its stiffness, its ability to absorb energy is referred to as its toughness, and the ability of a material to resist fracture is referred to as its strength [41]. Some metamaterials are classified based on their bulk material properties,

as illustrated in Figure 2.1 [2].

The mechanical characteristics of metamaterials have been the subject of investigation in a number of research published in academic journals. For instance, Yazdani Sarvestani et al., (2018) conducted research on a metamaterial that was made up of graphene and carbon nanotubes, and they evaluated its mechanical characteristics [42]. According to the findings of the research, the metamaterial demonstrated stiffness and toughness close to theoretical limits in addition to a high strength-to-weight ratio. These characteristics make the metamaterial appropriate for use in applications involving bio-medical and protective armor designs. In addition, the influence of the material structure on the mechanical characteristics of metamaterials was explored in a research that was carried out by Mohsenizadeh et al., (2018) [43]. According to the findings of the research, the structure of the material may be altered to change the mechanical characteristics of metamaterials. This allows the mechanical properties of the material to be tailored to particular applications in order to get the best possible results.

The range of values for the mechanical characteristics of natural materials is rather particular and constrained. Poisson's ratio is a good illustration of this point. Poisson's ratio is positive for the vast majority of the man-made and natural materials that are known to exist, with a few significant exceptions [44]. In addition, the physical and mechanical characteristics of the vast majority of naturally occurring materials are intertwined with one another. For instance, the elastic modulus or density of some classes of materials, such as the majority of cellular materials, is connected to one another via the use of a power law [45]. Porosity is the result of this relationship. The design space and the practical uses of natural materials are both restricted as a result of these limits. It is thus desirable to design materials that might show a set of physical and mechanical characteris-

tics selected for any application by the designer. The goal of mechanical metamaterials is to do exactly this.

In many cases, metamaterials are constructed from micro-architectures that have been thoughtfully planned out in order to provide a particular combination of desirable mechanical characteristics. Because the mechanical characteristics of metamaterials are reliant on their structure at the micro and nanoscales, the development of metamaterials simplifies the rational construction of the structure at the micro and nanoscales that is responsible for giving birth to the required mechanical qualities. metamaterials fall somewhere in the middle of the spectrum between pure natural materials, which have their own inherent mechanical properties, and large-scale structures, which are characterised by extremely design-specific structural features [46]. Pure natural materials have their own inherent mechanical properties. When seen at the micro and nano scales, the behavior of metamaterials is more like to that of structures. However, when taken as a whole, the homogenised behavior of metamaterials is very similar to that of materials. The homogenised macro-scale qualities are, of course, extremely reliant on the micro/nano-scale structure. This structure might be built in such a way that the resultant metamaterials display a unique, rare, or previously unheard-of variety of mechanical and physical properties [47].

In the beginning, optics and electromagnetism were the primary fields of use for metamaterials. Because of this, the word "meta-material" is frequently thought to apply specifically to "optical and magnetic metamaterials." In recent years, a new idea known as "mechanical metamaterials" has surfaced, although researchers have just scratched the surface of its potential applications [48]. Certain categories of mechanical metamaterials have been extensively researched and characterised over many decades. For instance, the notion of auxetic materials, which are materials that have a Poisson's

ratio that is negative, has been recognized to scientists for many decades, and particular instances of such components have been seen, manufactured, tested, and published (Figures 2.1 and 2.2). Recent research has led to the discovery of numerous other classes of metamaterials, each of which possesses an unusual collection of mechanical properties [49]. This discovery was made possible by a methodical investigation into the potential range of mechanical characteristics that could be acquired through the geometrical design of micro- and nano-architectures.

Extreme materials are described as materials that are exceedingly stiff in some forms of deformation, while still being extremely flexible in other modes. Milton and Cherkaev first presented the concept of extreme materials in 1995. The eigenvalues of elasticity tensor are either extremely big (that is, they approach infinity) or very tiny [50]. These eigenvalues dictate the behavior of extreme materials under any particular mode of stress and may be either very large or very minuscule (i.e. approach zero). When an eigenvalue is extremely tiny, it implies that the material is particularly yielding (less stiff) when it is deformed in the direction (also known as the eigenvector) that corresponds to that specific eigenvalue [51]. Therefore, it is possible to classify extreme materials according to the number of extremely tiny eigenvalues that the elasticity tensor has assigned to each of them. It is referred to as a unimode when an extreme meta-material only has one eigenvalue that is very tiny. It is referred to as having bimode, trimode, quadramode, and penta-mode, depending on the number of extremely tiny eigenvalues that it possesses: two, three, four, or five. The researchers Milton and Cherkaev demonstrated that extreme materials could be fabricated by using certain combinations of two phases, one of which was extremely soft and the other of which was highly rigid [50]. The extreme materials may then be coupled to produce materials with any specified

elasticity tensor that meets the conventional thermodynamics admissibility conditions. This would be possible because of the extreme nature of the materials. This is an important finding since in relation to composite materials, which could combine of two or more materials that results in better properties, one might simply utilise 3D printing methods to produce any material with positive definite viscoelastic tensors simply by incorporating void space with such a stiff 3D-printed material. This would allow one to create any material with cumulative distribution elasticity tensors [50]. Composite materials could also integrate very compliant as well as very stiff materials. In the research that has been done on extreme materials, there have been a special focus on two sub-types: penta-mode metamaterials and dilational materials (3D isotropic auxetics with an ultimate Poisson's ratio of -1). Both of these sub-types fall within the category of extreme materials [51].

Penta-mode metamaterials possess five extremely tiny eigenvalues, which indicates that they are highly compliant in 5 out of 6 primary directions (Figure 2.2). In other words, they are designed to have a finite bulk modulus but relatively insignificant shear modulus. This results in a bulk modulus that is much higher than their shear modulus [52]. The capacity of penta-mode metamaterials doesn't really change as a consequence of stress, which is equivalent to stating that Poisson number of metamaterials is 0.5. This is because very high values of the bulk modulus indicate that the volume does not change [53]. Because of its behavior, which is analogous to that of fluids, penta-mode metamaterials are often referred to as "meta-fluids." Very tiny quantities of the shear modulus indicate that perfect penta-mode metamaterials would soon flow away [54].

In 1995, Milton and Cherkaev suggested a particular design of penta-mode metamaterials. In this design, beams with a certain sort of variable cross-

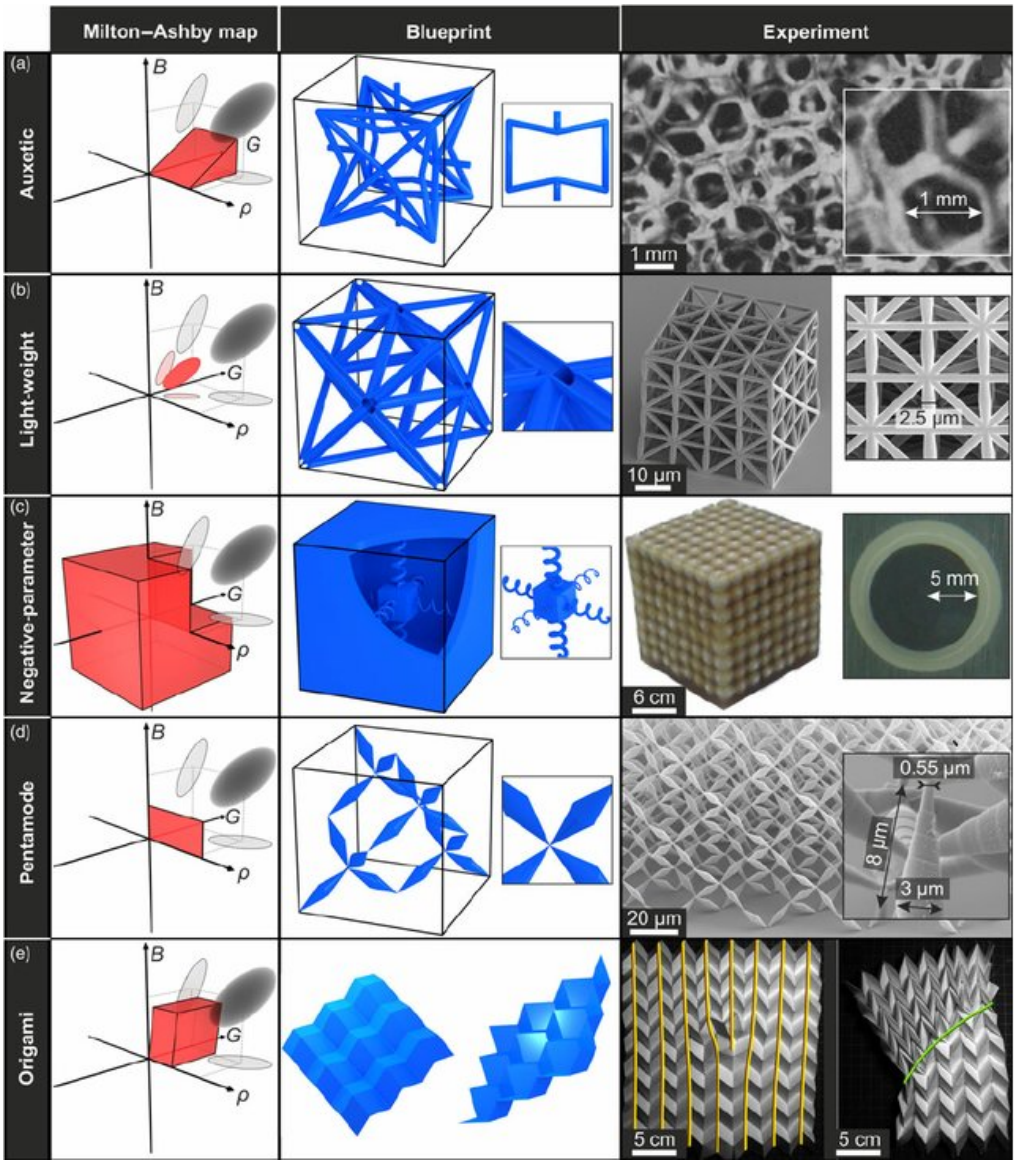

Figure 2.2: Overview on mechanical metamaterials. The five rows illustrate (a) auxetic, (b) light-weight, (c) negative-parameter, (d) penta-mode, and (e) Origami mechanical metamaterials [3].

section, namely two conical beams linked to one another at their bases, were organised in a diamond-type crystalline lattice [44]. It was not until 2012 that Wegener and his colleagues employed 3D printing methods to construct and test estimates of penta-mode metamaterials using polymers. This was the first time that this particular form of penta-mode crystalline lattice has been produced. Because the apex of the cone in actual realisations of penta-mode metamaterials has a finite diameter, as opposed to

having zero radii in the ideal penta-mode, the 3D printed metamaterials first at micro- or macro-scale are also all estimations of the perfect penta-mode metamaterials [55]. This is due to the fact that the ideal penta-mode has a diameter of zero. It has also been claimed that generalisations of penta-mode metamaterials may be applied to circumstances in which the material is anisotropic and to Bravais microstructures other than diamond.

Any stress that is moving through the lattice structure must be transmitted via the apexes of the cones in order for it to be considered properly transferred. This is a special feature of lattice structures that are based on penta-mode metamaterials. Therefore, expanding the size of the cone has only a marginal impact in terms of improving the toughness of the lattice structure [45, 56]. However, expanding the diameter of cone has a considerable impact on the mass density of the crystalline lattice. It is consequently possible to separate the mass concentration of penta-mode metamaterials from their stiffness. This is in contrast to the vast majority of porous materials or lattice structures, both of which exhibit a power law connection between the mass and the young's modulus of the framework. This relationship is referred to as an Ashby plot [57].

Because of their unique set of features, penta-mode metamaterials are a promising candidate for a variety of different uses. For instance, they might be used for the purpose of guiding elastodynamic waves in certain directions in order to accomplish the same results as optical cloaking but for acoustic waves [58]. When designing porous systems biology scaffolds, where the pore diameter as well as porosity have implications in terms of cell adhesion, cell nutrition/oxygenation, as well as percentage of tissue regeneration, it is useful to be able to change the elastic modulus as well as mass density (or permeability) of penta-mode metamaterials independently from each other [59]. This makes penta-mode metamaterials helpful for spreading the

design space. Furthermore, it is possible to build lattice structures for any positive definite stiffness tensor by mixing penta-mode metamaterials inside the same lattice structure. This may be done by combining the structures. As a result, penta-mode metamaterials may serve as a generic framework for the design and AM of metamaterials. This is especially helpful when it comes to developing materials that have a complicated distribution of different mechanical characteristics [58]. The complicated dispersion of the mechanical characteristics might have been caused by, for instance, the use of topology optimisation methods.

It is essential to understand that the penta-mode meta-material with which Milton and Cherkaev came up with their structure is not the only kind of penta-mode meta-material. A gel is a totally distinct kind of penta-mode material. Gels are characterised by their ability to be readily distorted in any given direction, while at the same time showing a high resistance to changes in volume when subjected to hydrostatic pressure [60]. Granular materials are still another kind of illustration.

The scope of materials that may have a negative Poisson's ratio extends beyond only dilational materials. In point of fact, the term "auxetic material" refers to any material that has a negative Poisson ratio. The etymology of the word "auxetic" may be traced back to the Greek word "auxeis", which meaning "to multiply and grow." As per Weeger et al., (2019) [61], Evans was the first person to use this word to characterise materials which expand in a direction that is perpendicular to the direction in which they are being loaded with tensile stress. Auxetic materials are among the metamaterials that have received the greatest research attention. A recent publication of an outstanding review study has been made available, and it addresses the many features of auxetic materials and the qualities that they possess. Because they are able to spread stress over a greater area of the material,

auxetic materials, in general, and dilational materials, in particular, have enhanced resistance against damage [61]. This is due to the fact that auxetic materials have the capacity to dilate. Montgomery et al., (2021) [60] provided a summary of the beneficial properties of auxetic materials, like enhanced indentation resistance and improved acoustic properties, and debated the areas in which auxetic materials are applied, such as a "efficient filter membrane with varying permeability, connectors, shape memory materials, and acoustic dampers". Cabras and Brun also discussed the areas in which auxetic materials are applied [62, 54].

Negative metamaterials include metamaterials that have negative moduli, like the minus bulk modulus or the negative elastic modulus. Examples of these include the minus bulk modulus and the negative elastic modulus. When it comes to the mechanical behavior of metamaterials, displaying negative moduli represents an entirely new level of oddity compared to what has observed up to this point in the research. This is due to the fact that up until this point, we have made the assumption that the flexibility tensor ought to be positive definite [58]. This implies that the bulk modulus as well as the shear modulus ought to be positive. Since many years ago, this requirement has been regarded as the appropriate specifications for an elasticity matrix to be deemed thermodynamically acceptable by the majority of researchers investigating continuum mechanics. The theory of thermodynamics that underpins this condition asserts that materials with negative deformation or negative stiffness are thermodynamically unstable [60]. However, in a wide range of experimental circumstances, the existence of materials with negative deformation or negative rigidity was demonstrated. If the stability of these materials can be assured, then a wide variety of uses may be possible for them. According to Bertoldi et al., (2017) [63] argument, even if a material with negative elastic modulus

that is unconstrained would not be stable, a material that is confined and has negative moduli might very well be stable. They contended that the elasticity vector of constrained components is not required to be favourably definite in order for it to be stable. This is because the prerequisites for the stability and the solution's uniqueness in the scenario of constrained components are strong ellipticities. Compressibility may be broken down into three categories: line, region, and volumetric compressibility. The most comprehensive definition of compressibility takes into account all three categories [64]. The line, area, & volume compressibilities of a material are each characterized by the variation in the lengths, the area, as well as the volume of the material when subjected to hydrostatic pressure in that specific order. A material is said to have negative compressibility when, in reaction to hydrostatic pressure, the material shows an expansion. It is possible for the material to have a negative lengths, area, or volume compressibility; this is something that is determined by the amount of dimensions across which the expansion happens [65]. Compressibility in length and area may be allowed even within the usual setting of thermodynamic limitations, despite the fact that the thermodynamic arguments against the negative compressibility primarily apply to the volume deformation.

The recent discovery of weak negative compressibility in methanol monohydrate, a relatively simple molecular crystal that exhibits negative linear elastic modulus along with negative as well as anisotropic thermal expansion, is one example of the identification of crystallites with negative line as well as area compressibility.

In addition to crystals, there are a few additional systems that display negative compressibility and may be broken down into four primary groups according to this property. The first group of these materials has a negative compressibility because the architecture of the cellular structures

gives them that characteristic. Lattice structures formed from an extended hexagonal dodecahedron, for instance, are examples of three-dimensional topologies that demonstrate negative Poisson's ratio or negative deformability. Another example is hexagonal honeycombs, which display negative linear deformability in two dimensions [66]. There is also a negative linear compressibility seen in tetragonal beam configurations. The combination of two different materials that each have their own unique set of mechanical characteristics is what gives the second group of metamaterials with minus deformation its unique quality. Chatterjee et al., (2021) [57] have provided an illustration of one such engineered material in their presentation. The same group of researchers came up with the idea for a truss-like structure that would be made of many different materials. The structure that has been presented has a negative linear compressibility, and in certain instances, it even demonstrates a negative area or volumetric compressibility. Specific limitations are the root cause of the negative compressibility shown by the third group of these types of materials. Most lately, researchers have been paying more attention to bulk materials that have the potential to show negative compressibility [42]. Certain kinds of (bi-stable) potentials have the ability to bring about a negative compressibility in the materials in question. In this last group of materials, the most essential thing to keep in mind is that negative deformation is a feature of the base material itself, and not a result of the particular manner in which the material's geometry is arranged [55]. The majority of the study done on this category of material up to this point has been theoretical, subjected to periodicity and neglecting the manufacturing defects.

2.2 Damage tolerant design of metamaterials

When defining the mechanical characteristics of metamaterials, the damage tolerance of the material is a significant element to consider. The capacity of a material to be worked into a desired shape without fracturing or breaking can be defined as damage tolerance. The metamaterials that have a greater damage tolerance also have a higher ductility, strength and stiffness, which makes them more suited for use in applications that need ductility, strength and stiffness [67].

Over the course of the last several decades, a new and distinct category of materials known as metamaterials has been produced. These materials have been developed in a laboratory to display qualities that can also be found in natural cellular materials. They provide a great degree of versatility and may be adapted to meet the requirements of a variety of applications [68]. Metamaterials may be made of metallic or non-metallic components that are organised in a certain pattern in order to generate the effect that is desired.

The domains of photonics, acoustics, and electronics are the ones that make the greatest use of metamaterials in their research and development. Traditional materials are limited in their capacity to control light, sound, and electricity compared to the capabilities of metamaterials, which can do so in a variety of novel ways. They are useful for the production of optical lenses and antennas, as well as for the regulation of sound and the construction of acoustic filters [69]. In addition, the aerospace and automotive sectors make use of metamaterials in order to manufacture lightweight components with high levels of performance.

Both the damage tolerance and the mechanical characteristics of metamaterials are dependent on the particular kind of material that is utilised as well as the arrangement of that material. Metals, ceramics, polymers, and composites are the most common types of components found in metamaterials. Materials that are not metallic, such as polymers, are often simpler to manipulate than metals, and they may be moulded into a variety of intricate designs. On the other side, working with metals is more challenging, but the material's strength and durability are superior. The orientation of the components of a metamaterial is also a factor in its damage tolerance [70]. This is because the orientation of the components may have an effect on how the material reacts when it is stressed.

Since, metamaterials possess favourable mechanical characteristics, and resistant to fatigue and corrosion. They are ideally suited for use in applications that demand long-term dependability. Because of these properties, they may be found in a wide variety of applications [71, 72]. As a result of their ability to be fabricated into lightweight, high-performance components that are also resistant to wear and tear, metamaterials find widespread use in a variety of sectors, including the aerospace industry, the automobile industry, and the medical industry.

Utilizing various manufacturing methods may also increase the applicability of metamaterials. For instance, laser welding and laser engraving are both methods that may be used to link components together, while vacuum forming is a technique that can be used to make intricate designs [73]. When it comes to the creation of components with exact dimensions and forms, other techniques of fabrication such as chemical etching, electroplating, and injection moulding are also relevant options.

In summing up, metamaterials are a special kind of material that belong to

their own class and have a broad variety of advantageous properties. They have a great degree of adaptability, which enables them to be modified to fulfil the requirements of a variety of applications. Because of their excellent damage tolerance characteristics as well as their excellent mechanical qualities, they are well suited for usage in a wide variety of industries. The use of metamaterials in the production of components that have improved performance and dependability is possible if the appropriate manufacturing processes and additives are utilised.

2.3 Role of machine learning

In the body of research on metamaterials, there has also been exploration into the application of machine learning to find optimal design and failure processes in the materials, in addition to investigations into the mechanical characteristics of metamaterials. In the field of artificial intelligence known as machine learning, identifying patterns in data is accomplished via the use of various algorithms [74]. This kind of study may be used in design optimisation of metamaterials and can also be used to examine the impact of various external stresses on the material such as failure process.

Researchers from the University of Amsterdam, AMOLF, and Utrecht University have proven the promise of a class of machine learning algorithms known as Convolutional Neural Networks (CNN) for the construction of sophisticated mechanical metamaterials. Their study, presents two distinct CNN-based approaches that are able to deduce and capture the delicate combinatorial principles that drive the design of mechanical metamaterials [54]. Both of these methods are described below.

Combinatorial design is a method to the creation of metamaterials that

includes deforming and arranging "building blocks" in order to generate metamaterials with the necessary functions. However, traditional physics simulation techniques are not necessarily enough, or will require enormous human power, time and computational processing power, when trying to investigate ideas for bigger unit cells [75]. Therefore, the researchers set out to find a machine learning technique that would make it possible for them to investigate the design space in a much shorter amount of time (see Figure 2.3 [4]).

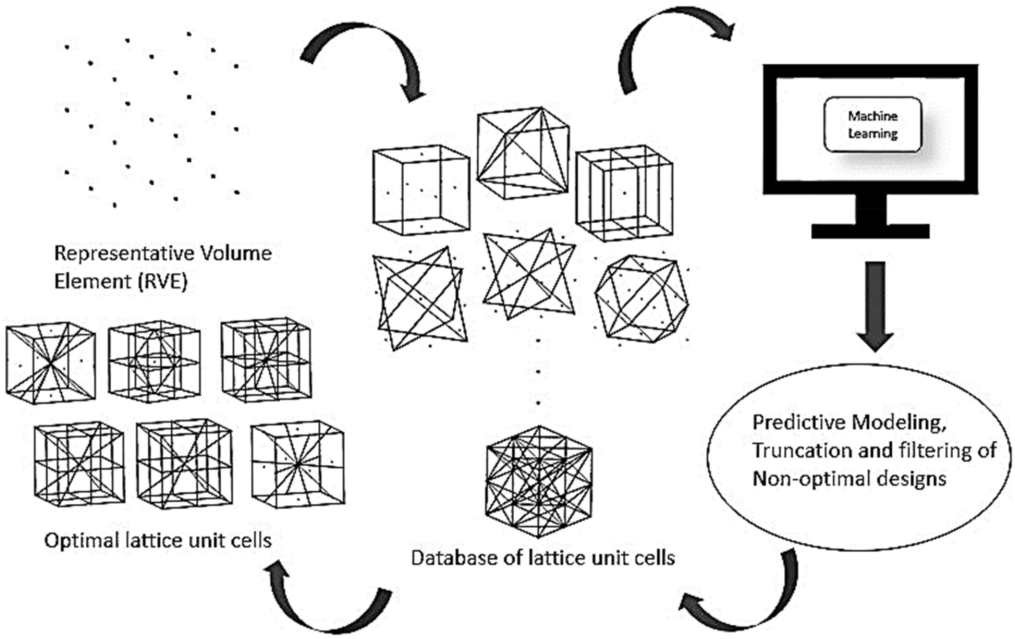

Figure 2.3: Schematic flowchart of optimisation process of unit cells using machine learning [4].

In order for the researchers to effectively train CNNs to handle the creation of complicated metamaterials, they had to overcome a number of obstacles along the way. They came up with a pixel representation that visually conveys the orientation of each constituent building block and refined it [76]. In addition to this, they developed two distinct CNN-based methodologies in order to take into account the enormous metamaterials class imbalance. The researchers want to shift their focus to inverse design in order to discover the optimal design for a certain undertaking, even if

the machine learning approach has not been provided with any samples to study in advance [76].

In general, the findings of the research demonstrate the use of machine learning for examining the design space available for metamaterials and maybe other types of materials, objects, or chemical compounds [54]. In addition to this, it demonstrates the ability of neural networks to effectively solve difficult combinatorial issues.

The use of machine learning to determine failure causes in metamaterials has been the subject of several research that have been published in academic journals. For instance, a metamaterial made out of carbon nanotubes was investigated by Bessa et al., (2019) [77], who utilised machine learning to determine the failure mechanisms present in the material. According to the findings of the research, machine learning may be used to detect the existence of faults in the material and to forecast the beginning of the failure process. In addition, a research that was conducted by Chang et al., (2022) [78] employed machine learning to investigate how the mechanical characteristics of a metamaterial were affected by the application of a variety of external stresses. According to the findings of the research, machine learning may be used to precisely anticipate the behavior of the material under a variety of loading circumstances, which would enable for the material's performance to be maximised.

It should be mentioned that, as in available publications, the majority of the stated recovery ultimate load are based on the findings of sample preparation like cube or cylinder, with just a few outliers that investigate lattice structures. This is something that should be taken into consideration. It is common knowledge that the particular load bearing capacity of a material may be considerably increased if the material is produced into different

structures rather than solid cuboid beams [79, 62]. Some examples of these types of structures are I-beams, T-beams, box-beams, and sandwich beams. Because of this, it is anticipated that the particular recovery stress will be able to be increased when Shape Memory Polymer (SMP) are produced into metamaterials as opposed to when they are in the form of solid SMP structures.

Lightweight metamaterials relate to materials such as cellular structures, thin-walled cell components, auxetic frameworks and composite plate-lattice cells. Due of the multifunctional benefits that these structures provide in mechanical, acoustic, and thermal applications, they have received a significant amount of research. Many research have been done to provide theoretical models in order to predict and study the structural behavior of metamaterials, and these models have been the focus of a lot of those investigations. In the past, mechanically adjustable metamaterials were Three dimensional (3D) printed utilizing just a SMP [61]. These metamaterials were made up of Octet or Kelvin honeycomb unit cells SMP. SMPs that have the potential to be employed in medical devices were used in the designing and printing of auxetic structures that have mechanical characteristics that can be tuned. A metamaterial with a hierarchically organised and strain-dependent solid–solid phase shift was devised with the intention of having applicability in micro-actuators and vise grips, as well as programmable devices. Assessing their mass, buckling load, free vibration, Poisson's ratio, or compression resistance with an abundance of computational and experimental findings has led to the development of a number of further two-dimensional & three-dimensional auxetic structures [80]. The peculiar behavior of auxetic structures, which is caused by the orientation of their structural components, has a number of potential uses in the fields of medicine, athletics, and automotive technology. In order to

improve these metamaterials and attain their optimum performance, the majority of the time, topology optimisation approaches were applied [81]. One of the limitations of optimisation is that it is unable to optimise systems using a single parent design, but there is a large design area for the global optimal solution. This is one of the reasons why topology optimisation is not as popular as it once was. In order to get around this restriction, a number of data-driven structural optimisation and design strategies have been suggested for the development of innovative metamaterials [61]. Inverse design frameworks that make use of Generative Adversarial Networks as well as machine learning multiple regressions have been suggested as a means of exploring a broad range of design space in the direction of the global optimal solution.

The goal of machine learning tools is to learn from a training sample in order to find hidden patterns. These patterns may then be utilised for the categorization or prediction of an untrained dataset with little intervention from humans and processing capacity. The use of machine learning or data analysis frameworks received a significant amount of attention during the identification and optimisation of a variety of newly developed materials, architectures, and technologies. In the process of finding novel porous crystalline materials like zeolites as well as metal organic frameworks, it was shown that machine learning methods are superior to the laborious trial-and-error procedure that is used in experimental or computational analyses [49]. In recent work, to improve wind turbines, a hybrid structural optimisation and design model was created [82]. This model was shown to have the same level of accuracy as more advanced Computational Fluid Dynamics (CFD) models. In order to design multipurpose metamaterials and expedite the design of complex devices for interaction, computing, as well as optical device applications, which would otherwise be unattainable

with traditional physics-based approaches, slope and no-gradient premised automated learning optimal control loops were developed. These loops were used to design multifunctional metamaterials. In the past, researchers have published a few different innovative lightweight metamaterials that have greater compression capacities, buckling loads, naturally higher frequency, and improved impact energy absorptions [83]. Even while a few structures have been anticipated to have excellent shape memory qualities, very few strategies for the selection or optimisation of structures have been examined up to this point. Due to the one-of-a-kind thermomechanical behaviors of SMP metamaterials, the numerical evaluation of these components can be overly complicated, and the experimental results of these materials are time-consuming due to the numerous thermomechanical processes that are required. This is especially true when agglomerates are implicated [53].

When designing a complex structure such as metamaterials, it is important to strike a balance between flexibility and strength so that the structure can accommodate bigger displacements. Within the realm of lightweight structures, we began by contemplating stretch-dominated structures in an effort to strike a compromise between these two competing objectives. FCC structures with disorderliness were investigated for their increased ductility with low expense of strength and stiffness in the plane of the structure. Now, it solves the second criteria by optimising stretch-dominated structures with greater strength or higher ductility. This may be done by using a combination of both.

Even though various lattice components with better strength and stiffness characteristics have previously been offered, there remains a research gap in presenting approaches to investigate a broad range of design space beyond elastic limits. In the past, this research gap has been acknowledged. Although some methods, such as topology optimisation, might result in op-

timum structures, a data-driven method may get us far nearer to the global optimal solution, and, a machine learning based technique can be easily applied to scout the wide range of unexplored design space by by-passing the complex numerical analysis.

2.3.1 Global optimisation algorithms

Many problems in a variety of disciplines can be formulated as optimisation problems; and most of these can be solved by adopting one of two "popular" approaches: divide-and-conquer or hill climbing techniques [84]. In the first approach, the solution is problem-dependent, and typically detailed information about the problem is required in order to develop a solution strategy. Also, not many problems can be subdivided into smaller parts that can be solved separately and then recombined. In the second approach, most hill-climbing algorithms are based on gradient descent methods. These methods suffer from a major drawback of getting trapped in a local minimum. That is, the algorithm may get "trapped" in a valley, from which all paths lead to locally worse solutions, and will never get to an optimal solution that lies outside the valley. The global optimisation algorithms avoid local minima by introducing an element of randomness into the search process. Figure 2.4 gives a summary for global optimisation methods.

Stochastic optimisation algorithms have become very popular in the last decade or two. Unlike the local techniques, where a single design point is updated (typically using gradient information) from one iteration to the next, these algorithms do not require any gradient information and typically make use of a set of design points (generally referred to as a population) to find the optimum design. These methods are typically in-

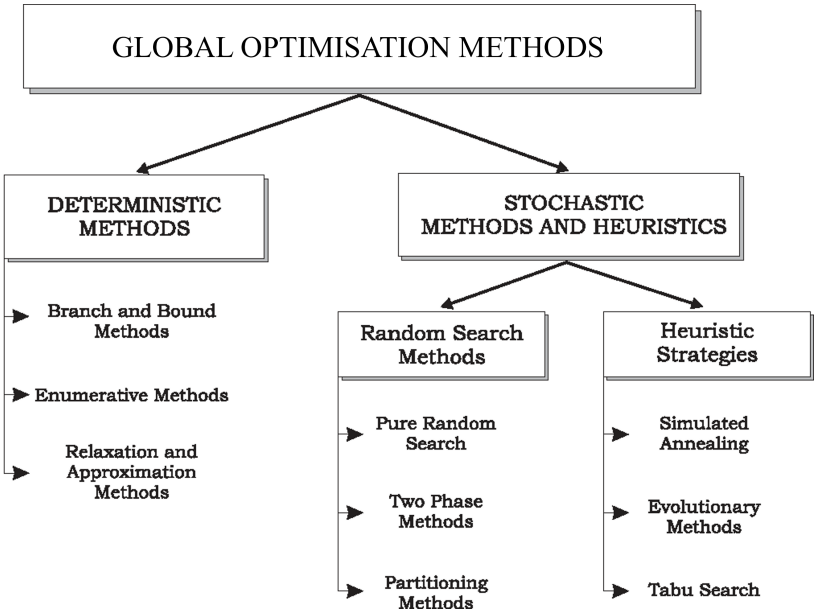

Figure 2.4: A summary of the global optimisation methods

spired by some phenomena from nature and have the advantage of being extremely robust, having an increased chance of finding a global or near global optimum, being easy to implement and being well suited for discrete optimisation problems. A few drawbacks associated with these algorithms are high computational cost, poor constraint-handling abilities, problem-specific parameter tuning and limited problem size.

Currently, two of the most popular stochastic algorithms are Random Search Method [85–88], and Heuristic Strategies, which are motivated by certain analogies with natural phenomena or basic sciences. Other algorithms that fall into Heuristic Strategy category include evolutionary programming [89], genetic programming [90], differential evolution [91], simulated annealing [92], tabu search [93], ant colony optimisation [94], harmony search [95], etc.

An important characteristic of the simulated annealing algorithm is that it does not require specialist knowledge about how to solve a particular problem. This makes the algorithm generic in the sense that it can be used

in a variety of optimisation problems without the need to change the basic structure of the computations. The simulated annealing algorithm (sequential or parallel) has been applied to a wide range of problems. However, there is still great potential in using the simulated annealing algorithm to solve more formidable problems that can be formulated as optimisation problems. There is however, an even greater opportunity: using the simulated annealing algorithm in combination with other stochastic techniques such as neural networks and genetic algorithms to produce more powerful problem solving tools.

2.4 Creep failures

2.4.1 Fundamentals of creep

The characterisation of mechanical properties is essential before AM components can safely be used in beyond static applications. A review of the mechanical properties of metal AM parts was given by Lewandowski et al. [96]. Creep is a time-dependent continuous deformation which occurs at high temperatures (above 0.3-0.4 of melting temperature) and stresses [97, 5]. Therefore, the creep strain (ε) depends on stress (σ), time (t) and temperature (T), resulting in the following relationship: $\varepsilon = f(\sigma, t, T)$ [5]. A brief overview of the different creep mechanisms and micro-mechanisms is discussed below.

There are two main creep mechanisms: diffusional creep and dislocation creep. The creep rate of both mechanisms is limited by diffusion [97, 5]. These mechanisms occur at different temperature and stress ranges and in the intermediate temperature regime, creep deformation can be a mix of the

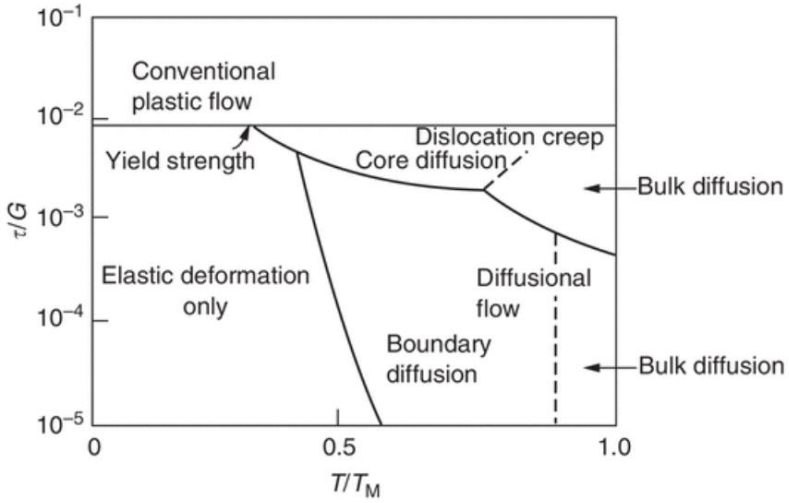

Figure 2.5: Creep deformation mechanisms at different stresses and temperatures (τ is the equivalent shear stress and G is the shear modulus) [5].

both mechanisms [97]. The deformation mechanism diagram (Figure 2.5) summarises the competition between the two mechanisms [5]. Regardless of the mechanism, creep damage, which is material degradation that gives rise to tertiary creep, occurs in specimens [98]. One of the most common type of damage is by loss of internal section with cavitation perpendicular to tensile stress or the growth of a dominant crack, which reduces the section and accelerates the creep rate [98]. Figure 2.6 illustrates this type of cavitation damage and how it corresponds to the creep curve, particularly to the tertiary region.

There are various creep models available for creep. Commonly used models include the Norton Power Law, the damage models and microstructure models. One of the simplest models is the Norton Power Law model which can model the steady state creep rate of materials. This model is dependent mainly on stress and shows close correlation between experiments in prediction for secondary creep rates. However, this model greatly deviates from experiment results for tertiary creep rates. So other models may be better fit, as was the case for Hayhurst et al. [99] who found that a sinh

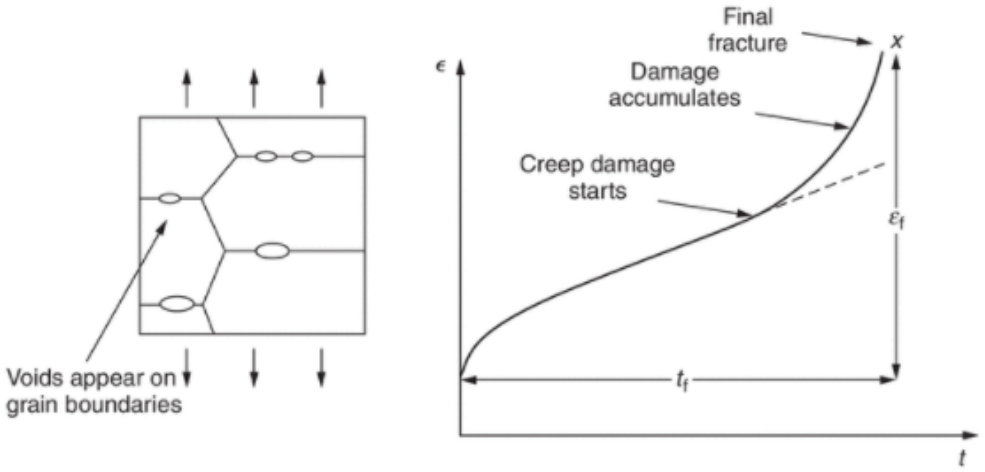

Figure 2.6: Illustration of creep damage due to cavitation and the effects on the creep curve, mainly in the tertiary region [5].

function of stress, rather than the power law was best to describe the strain rate and rupture behaviour of an aluminium alloy.

Damage models take into account damage sustained by the material prior and during creep. The Liu-Murakami model works on the assumption that creep strain rate depends not only on the applied stress, but also takes into account the amount of damage sustained. This model shows a very high correlation in the primary and secondary creep between the experiments and predictions, and a slight deviation is noticed when the material gets into the tertiary creep stage. Therefore, the Liu-Murakami model can be satisfactorily applied across the whole range of creep damage of materials.

Continuum damage models are used to describe damage in materials, such as microvoids or microcracks initiation and propagation until failure. The concept of continuum damage mechanics was firstly introduced by Kachanov [100]. A method to consider the degradation of constitutive properties, integrated with a theory for life prediction is provided by the method of continuum damage mechanics. The original ideas of Kachanov [100], is inspired by the observation that, at temperatures above about half of melting

temperature, grain boundary cavities form with time. The cavities nucleate, grow and eventually coalesce to form a major crack which leads to final creep rupture. This type of model can be very useful in modelling creep where microvoid initiation and coalescence occurs. This can also be even more applicable to LPBF materials which have higher porosities than their conventionally manufactured equivalents.

2.4.2 Creep behavior of metamaterials

In recent years, the equivalent creep strength of cellular or metamaterials has been extensively studied. Gibson and Ashby [101] derived an analytical expression (GA model) to predict the creep rate of honeycombs basing on the assumption that the bending of solid strut perpendicular to the compressive load is the dominant deformation mechanism. The steady creep rate and creep failure time for a closed-cell aluminum foam has been investigated by Andrews et al. [102], and the results indicate that the creep property of foam materials is impacted significantly by the strut dimension and creep parameter. The creep strain rate is affected significantly by the relative density, microstructural imperfection and the creep parameters of solid cell struts [103]. Fan et al. [104] investigated the uniaxial and multiaxial creep behavior of low density open-cell foams and proposed a modified GA model by taking the mass at strut node into account. The analytical model agrees well with the simulation results.

Boonyongmaneerat and Dunand [105] developed a set of theoretical expressions to investigate the creep rate of the metallic foams. The results indicate that the dominant creep deformation mechanisms of the strut transform from bending to shearing, and then to compression as the relative density increases. Lin and Huang [106] investigated the compressive creep

properties of the hexagonal honeycombs and derived a set of formulas to predict the elastic buckling strength and the creep-buckling life. The results show that the solid distribution is dominant influencing factor for the creep-buckling life, and the failure mechanism changes from creep-bending to creep-buckling as the relative density increases. Andrews et al. [101] and Andrews et al. [102] proposed a model to calculate the creep-rupture life of the foams based on the Monkman–Grant relationship. The results indicate that the creep-rupture life can be predicted accurately when the creep rate and creep constants are determined. A creep-rupture model of open-cell foams has been derived Chen and Huang [107]. The results indicate that the creep-rupture time is sensitive to their cell structural imperfection.

Although the creep behavior of the cellular metamaterials has been studied extensively in recent years, how to calculate the creep-rupture and effects of microstructures in creep life due to manufacturing defects is still unclear for the truss lattice structures. Therefore, in this work, I have investigated the creep-rupture failure time of a BCC based truss lattice structure via the Kachanov's damage models. Moreover, how the microstructural defects affect the creep life has been studied fully.

2.5 Research gap

The term "metamaterial" refers to a newly discovered category of man-made materials called "engineered materials." These materials are created to have features that are superior to those found in natural materials. In recent years, metamaterials have attracted a growing amount of interest due to the fact that they are able to alter light, sound, and several other types of energy in ways that were not before feasible. The creation of

metamaterials, which are composed of carefully ordered components or "units" that interact with one another to generate desired behaviors, makes it feasible to do this manipulation [108]. Metamaterials are comprised of "units" that interact with one another. Metamaterials may be engineered to have a variety of features, such as a negative refractive index and the ability to conceal acoustic energy, and they have the potential to be used in a broad variety of contexts.

To develop and optimise metamaterials, however, one often needs an in-depth knowledge of the failure processes and mechanical behaviors of the materials one is working with. This is because of the complicated nature of metamaterials. This work will offer an overview of the study of failure causes and mechanical behaviors of metamaterial designs, with a specific emphasis on two-dimensional metamaterials [109]. The study will also include a particular focus on how disorderliness may be used to create new optimised truss lattice metamaterials.

It is common practice to organise the constituent parts of a metamaterial in a periodic arrangement, which simply means in a pattern that repeats itself. This periodic arrangement of the units enables the metamaterial to exhibit characteristics that are desirable throughout a broad range of applications. Because the properties of the material can be tuned by altering the arrangement of the units, the periodic arrangement also enables the metamaterial to have a high degree of control over the properties that it produces. This is made possible by the fact that the units are arranged in a periodic pattern.

Failure mechanisms are the processes that a material goes through that cause it to not function as it was designed to. The kind of metamaterial, the configuration of the components, and the external stress conditions

all have a role in determining the failure processes of metamaterials. It is impossible to successfully develop and optimise metamaterials without first having a comprehensive grasp of the failure processes involved.

Plastic deformation, mechanical fatigue, and electrical breakdown are the three failure modes of metamaterials that occur the most often. Plastic deformation takes place when a material is exposed to a force that is larger than its yield strength. This causes the material to permanently distort as a result of the stress. Cracks and other damage might appear in the material as a consequence of cumulative strain if the material has been exposed to cyclic loading, which is what causes mechanical fatigue. Electrical breakdown happens when the material in question is exposed to a strong electric field, which ultimately leads to the substance's destruction and failure [110]. Other types of failure processes, such as chemical corrosion and heat failure, are also possibilities in some metamaterial design implementations.

The types of metamaterials, the arrangements of the components, and the circumstances of the external loading all play a role in determining the mechanical behaviors of metamaterials. Both elastic and inelastic mechanical behaviors may be exhibited by metamaterials. These behaviors can be classified according to their respective terms. When a material is exposed to a force and then returns to its original form once the force is withdrawn, the material is said to be exhibiting elastic behavior [77]. When a material is exposed to a force, and when the force is withdrawn, the material does not return to its previous form, then the material is said to be exhibiting inelastic behavior.

The mechanical behavior of metamaterials is often defined by the material's modulus, which is a measure of the material's stiffness and may be thought

of as a measure of the material's resistance to deformation. The modulus of a metamaterial is governed not only by the components that compose it and the order of those elements, but also by the circumstances of the external loading [62]. Metamaterials that have lower moduli have a tendency to be more malleable, whereas those with higher moduli have a tendency to be stiffer and less prone to deformation.

The ductility of a metamaterial is defined by the degree to which a material can sustain plastic deformation under tensile stress before failure, and it may also be used to define the mechanical behavior of a metamaterial. The amount of ductility a metamaterial provides is dependent not only on the kind of element that is used but also on the arrangement of the components and the circumstances of the external loading [80].

According to the study that has been done [55, 111], there are a number of research gaps that need to be filled in order to increase our knowledge of the mechanical characteristics of metamaterials. To begin, there is a need for more investigation into the ways in which the mechanical characteristics of metamaterials are influenced by a variety of various kinds of external loads. In addition, there is a need for more study to be conducted in order to examine the impacts of manufacturing defects on the mechanical characteristics of metamaterials. In conclusion, there is a need for more investigation into failure mechanisms, the use of machine learning to the task of identifying optimised designs and manufacturing defects affecting mechanical characteristics such as creep.

2.6 Summary

In a nutshell, metamaterials are artificial man made materials that are inspired by natural materials. This results in the creation of novel combinations of physical characteristics that has a resemblance in the nature. The mechanical characteristics of a metamaterial are often what defines it, and these qualities are influenced by the sort of component materials employed, the structure of the material, and the production method. In addition, research published in academic journals has investigated the use of machine learning with the goals of determining failure processes in metamaterials and analysing the impacts of various types of external stresses on the material. Finally, the ability to work in a wide range of applications of the metamaterials is an important factor in determining their mechanical properties such as ductility, strength and creep. A number of research gaps have been identified in the existing body of literature, and these gaps need to be addressed in order to improve our understanding of the mechanical properties of metamaterials.

Chapter 3

Methodology

3.1 Introduction

The following section outlines the superficial methodology employed in this study. The main objective of this study is to investigate the failure mechanisms and mechanical behaviors of metamaterials manufactured using AM techniques. The metamaterials under investigation contain various types of defects, which I aimed to quantify and analyze. To achieve this, I used MATLAB and ABAQUS software for metamaterial modeling and simulations. The general outline of the work is shown in Figure 3.1, along with the tools used in this study.

I began by studying the effects of geometrical and dimensional defects on the mechanical behaviors and failure mechanisms of the metamaterials. Specifically, I examined the impact of distorted struts, missing struts, and strut diameter variations on the overall mechanical properties of the material. A novel numerical framework has been developed to overcome computational difficulties such as strut buckling and excessive distortion

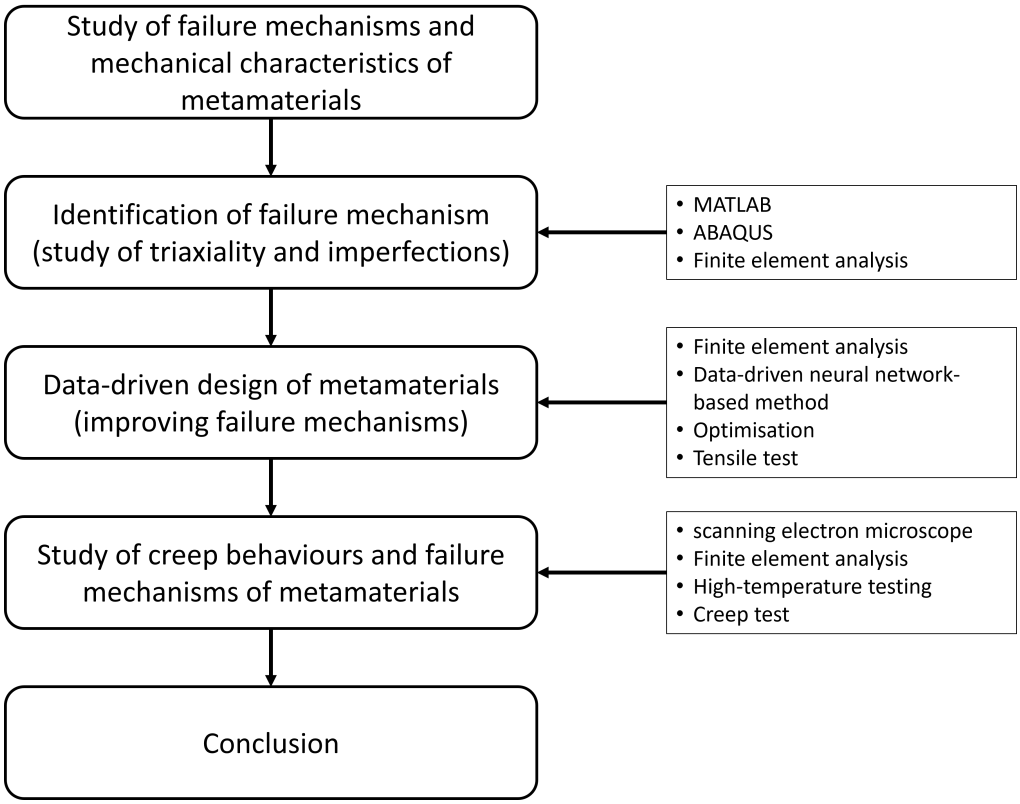

Figure 3.1: Methodology flow chart, summarising the work flow of this study

on lattice metamaterials, beyond the elastic region. The results of the numerical simulations were used to analyse the failure mechanisms of the metamaterials and their mechanical behaviours under multi-axial loading.

Next, I employed a machine learning or Artificial Neural Networks (ANN) based data-driven methodology to optimise the design of the metamaterials and make use of the geometrical inaccuracies to our advantage. By changing the failure mechanisms of the metamaterials, I aimed to increase its ductility while minimizing the loss of stiffness and strength. Then, the experimental testing was conducted to validate the numerical models and to study the mechanical properties of the fabricated metamaterials. The mechanical properties of the metamaterials, such as load-displacement curves till failure, are measured using a universal testing machine.

Finally, I investigated the creep behavior of the metamaterials. I conducted

the tensile test at elevated temperatures (650 ℃) to understand the effects of microstructures on creep resistance. I analyzed the creep behavior of the metamaterials and compared the results under different loading conditions. This study provides valuable insights into the complex micro-structures of the metamaterials and how they affect their mechanical properties.

Overall, this study provides a comprehensive analysis of the failure mechanisms and mechanical behaviors of metamaterials. Our use of AM and data-driven methodology provides new avenues for improving the design of metamaterials and optimising their mechanical properties.

3.2 Limitations

While the methodology used in this study provided valuable insights into the failure mechanisms, mechanical behaviors, and design optimisation of mechanical metamaterials, it is important to acknowledge its limitations. The following are some of the limitations that should be considered when interpreting the results of this study:

- This study focuses mostly on a specific type of stretch dominated deformation mechanism metamaterials Face Centred Cubic (FCC) and Body Centred Cubic (BCC), and the conclusions may not be applicable to other types of metamaterials or other manufacturing techniques.
- The study focused on only three types of imperfections: distorted struts, missing struts, and strut diameter variation. Other types of defects such as surface quality, porosity, and surface cracks, may have different effects on the mechanical behaviors of the metamaterials.

- The data-driven approach I have used to design the metamaterials is based on a limited amount of data, and the performance of the resulting designs may be sensitive to changes in the data set or the training process. Furthermore, the approach assumes that the geometrical defects in the metamaterials can be accurately characterized and controlled, which may not be feasible in practice.

- The study of creep behaviour of metamaterials was conducted at a specific temperature, and the results may not be applicable to other temperature. Further investigations are needed to fully understand the effects of microstructure on the creep behaviour of metamaterials under different environmental conditions. Additionally, the experimental validation of our methodology was limited in scope, and more extensive testing is needed to fully assess the effectiveness and reliability of the approach.

- One limitation of using 2D lattices instead of 3D lattices is the potential loss of accuracy or realism in representing complex spatial relationships. While 2D lattices can be useful for modelling certain mechanical behaviours, they may not fully capture the intricate interactions and dynamics that occur in 3D space.

3.3 Summary

Overall, this methodology provides a comprehensive approach to investigate the failure mechanisms and mechanical behaviors of metamaterials under different conditions and develop improved designs with desirable properties. The methodology employed in this study combines numerical modelling and experimental testing to investigate the mechanical proper-

ties of mechanical metamaterials. The numerical simulations provide a detailed understanding of the mechanical behaviour of the metamaterials under various loading conditions and the effects of defects on their mechanical properties. The experimental testing validates the accuracy of the numerical models and provides insight into the mechanical properties of the fabricated metamaterials. The results of this study contribute to the development of mechanical metamaterials with improved mechanical properties using AM technologies.

Chapter 4

Localisation and coalescence of imperfect planar FCC truss lattice metamaterials under multiaxial loadings

4.1 Introduction

AM technologies have numerous advantages over most traditional manufacturing methods, the most distinct of which is its flexibility to manufacture complex geometries with little or no cost or time penalty [20, 112]. Another advantage is in low volume manufacture, where the lack of moulds or tooling can make AM cost effective, this is especially advantageous for tailored products. AM has spurred recent interest in cellular lattice structures as the technology enables a range of cell types, functional grading and conformity to complex external geometry not achievable with any other manufacturing method [113, 114]. Many researchers are involved in design-

ing complex structures via the use of lattices with different unit cells and relative densities [115]. Köhnen et al. [116] studied plastic deformation behaviour of FCC and hollow spherical lattice structures under tensile, compressive and cyclic loadings. In this study FCC lattices revealed a stretch dominated deformation behaviour, while hollowed spherical lattices revealed bending dominated deformation behaviour. Vigliotti et al. [117] established a nonlinear constitutive model for truss lattice materials. In this study, the influence of Representative Volume Element (RVE) is discussed. The hexagonal and the triangulated lattices were selected as case studies and discrete models compared to the prediction of the continuous model. The results found a good qualitative and quantitative agreement among models. Geng et al. [118] showed differences in the fracture modes of three lattice structures and the evolution processes of damage variables using ductile and shear damage models. Alsalla et al. [119] presented a method for estimating the local failure mechanism of 316 L stainless steel lattice material under uniaxial tensile and three-point bending loads. The results show that the tensile strength and fracture toughness of the lattice structure in different directions are different.

The above research demonstrates research in the design of lattices for AM and both experimental and computational analysis of their mechanical properties and failure modes, however, another important aspect that is less studied is the effect of defects on lattice performance. It is inevitable that additively manufactured lattice structures will contain defects not included in the designed (perfect) geometries [120, 121]. Real truss lattices typically contain material and geometric imperfections that may strongly influence their elastic and plastic responses and failure mechanisms. While predictive models of perfect lattices have been used to evaluate both linear and non-linear responses under applied stress [122, 123], they generally

fall short in capturing the experimentally observed response of imperfect lattices. Liu et al. [124] investigated the effect of geometric defects on the elastic response, damage initiation and evolution of three-dimensional octet and rhombicuboctahedron periodic structures manufactured by Laser powder bed fusion (LPBF) process. Wehmeyer et al. [125] presented analytical and reduced-order numerical solutions to predict post buckling behaviour in cellular structures including the role of geometric imperfections. They provided regime maps that shows lattice strut configurations that lead to permanent deformation after unloading, strut failure and enhanced hysteresis during cyclic loading. Other studies on imperfect lattice structures include [126, 127].

In metallic solids, ductile behaviour, and failure mechanisms such as localisation and void coalescence are the main failure mechanisms impacting structural integrity. The field of ductile fracture has been extensively researched for solid isotropic materials, resulting in more reliable damage models and localisation criteria. An example is the recent work related to stress triaxiality dependency [128–130]. The micro-mechanisms governing ductile shear failure was investigated by Tvergaard et al. [131] using a 2D plane strain numerical cell-model of a single row of equal sized circular cylindrical voids under shearing. As a first, Tvergaard et al. [132] demonstrated that a maximum load bearing capacity for a ductile material was attained in a shear field due to micro-void interaction. Anderson et al. [133] showed that, during shearing, the voids flattened to form micro-cracks, which rotate and elongate until interaction with neighbouring micro-cracks results in coalescence. Failure mechanisms are thereby seen to change with different conditions of stress triaxiality.

The five generic scenarios of localisation and void coalescence failure mechanisms in solids are illustrated in Figure 4.1. Mechanism 1 is localised

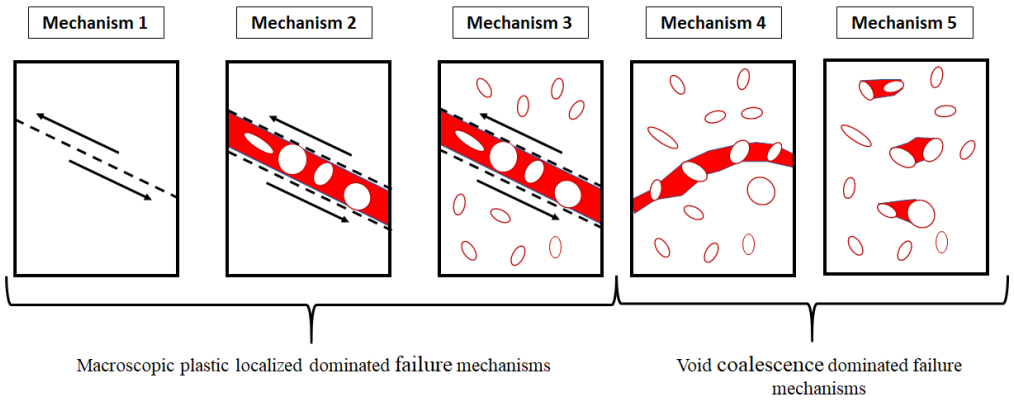

Figure 4.1: Five generic scenarios of ductile fracture in isotropic solid materials [6]

plastic flow failure in pure metals only, Mechanism 2 is void nucleation after macroscopic localisation into shear band, Mechanism 3 is shear band localisation owing to porosity present in the metals, Mechanism 4 is failure by void coalescence or occurrence of localisation and void coalescence simultaneously, and Mechanism 5 is the subset of Mechanism 4, distinguished as cluster localisation of few voids instead of macroscopic localisation extending over many voids. The ductile failure of solids is often related to progressive nucleation, growth, and coalescence of micro-voids and microscopic localisation.

It is proposed that lattice structures may exhibit comparable mechanisms of micro-localisation before final failure depending upon the type of defects and state of stress. It is further proposed that imperfections present in lattices will lead to the onset of microscopic localisation or void coalescence, which may serve as an effective indicator of a material's ductility. This is the precursor to failure and marks the limit that a uniform strain can be imposed on the material. Pursuant of this hypothesis, the effects of triaxiality on imperfect lattices and their failure behaviour are comprehensively studied in this chapter.

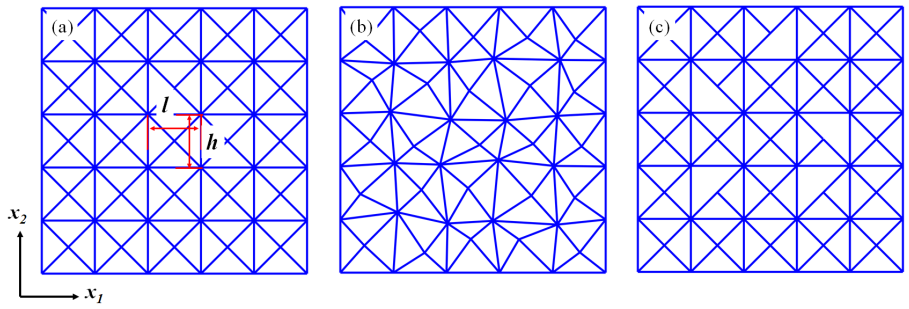

Figure 4.2: Representation of FCC truss lattice metamaterials with and without manufacturing defects (a) perfect lattice, (b) distorted lattice, and (c) missing struts lattice

The chapter is organized as follow. A classification and modelling of lattice defects are presented in Section 4.2 along with possible failure mechanism identified in this chapter. The development of the model, along with numerical implementation is described in Section 4.3. The results of the numerical simulations are presented and discussed in detail in Section 4.4. Section 4.5 contains concluding remarks and suggestions for further research.

4.2 Imperfect lattice structures and failure mechanisms

4.2.1 Classification and modelling of imperfect lattices

Common geometric defects in the manufacture of FCC truss lattice metamaterials through powder bed fusion can be classified into the following categories [134, 135], as shown in Figures 4.2 (a) to (c).

1. **Distorted struts** can be characterized by node deviation from the collinear axis of the as-designed struts [136]. Additionally, some of the

distorted strut cellular geometries are inspired by the natural cellular materials with desired or extreme mechanical properties, this has been discussed later in this work with details. As shown in Figure 4.2 (b), nodal distortion of FCC truss lattices causes misalignment in the attached struts. Modelling of distorted struts was achieved through introducing geometrical perturbation to the nodes of a perfect FCC truss lattice. Let (x_1^i, x_2^i) represent the spatial coordinates of the i^{th} node within a perfect FCC truss lattice. The new position of the node $\left(\overline{x}_1^i, \overline{x}_2^i\right)$ after perturbation can be written as:

$$\overline{x}_1^i = x_1^i + \beta \left(\alpha \sqrt{\frac{l^2 + h^2}{4}} \right) \tag{4.1}$$

$$\overline{x}_2^i = x_2^i + \beta \left(\alpha \sqrt{\frac{l^2 + h^2}{4}} \right) \tag{4.2}$$

where $\beta \quad (-1 \leq \beta \leq +1)$ denotes a random variable following a uniform probability distribution, α the degree of irregularity , and l and h are the lengths of the unit cell in the x_1 and x_2 directions, respectively (see Figures 4.2 (a) and (b)). Romijn and Fleck [137] studied five lattice types, namely Square, Diamond, Hexagonal, Triangular and Kagome, with randomly perturbed nodes in the range of irregularity 0% (perfect lattice) to 50% (extremely imperfect lattice). They showed that the relative density remains the same with perturbed nodes, however, the elastic modulus and fracture toughness are highly sensitive to strut distortion, this also being dependent on the lattice type. In the current chapter, degrees of irregularity of $\alpha = 15\%$ and 30% were chosen, in order to prevent impingement of adjacent nodes of FCC truss lattice and to demonstrate strain localisation and the effects of a stress state beyond the elastic limit.

2. **Missing struts** are modelled to study the effects of absent struts caused by incomplete fusion in the material. It is generally accepted that randomly missed struts widely exist in lattice structures. The missing struts were modelled in this work through randomly removing struts from a perfect lattice, as illustrated in Figure 4.2 (c). Let k denote the number of struts that were removed from a lattice of n struts. The level of the manufacturing defect with missing struts can be quantified through $\eta = k/n$. Su et al. [138] and Chen et al. [139] studied missing strut effects ranging from $\eta = 0\%$ to 10% and showed that the mechanical properties of lattice structures are very sensitive to the quantity of missing struts. In the current chapter, $\eta = 5\%$ and 10% were selected for the numerical study.

3. **Dimensional inaccuracy** can be caused by over-melting or over heating during LPBF, which results into deviations from circular cross-sections to ellipsoidal [140]. Arabnejad et al. [141] studied such variations in strut diameter and noted a variation from 45% reduction to 100% increase in strut diameter. In this chapter, the effect of dimensional inaccuracy on the failure modes of lattices is investigated by the use of three different diameters; $0.5d$, $1.0d$ and $1.5d$ where d is the initial diameter of the struts.

4.2.2 Failure mechanisms

In this chapter, I have discovered five failure mechanisms of FCC truss lattice metamaterials with and without defects as shown in Figure 4.3, that are analogous to well-known failure mechanisms seen in isotropic solids. These are discussed below:

1. **Mechanism 1** occurs for lattices buckling predominantly under compressive loading.

2. **Mechanism 2** is analogous to non-porous solid failure due to plastic localisation in shear band by various possible mechanisms such as dislocation slipping. Following the formation of the plastic localisation inside of band, voids coalesce, leading to final separation. This mechanism occurs due to high stress concentration near a crack tip in solid structures. In lattice structures, lattices with distorted nodes may fail in an analogous fashion due to the abrupt change in load path that this causes.

3. **Mechanism 3** corresponds to the occurrence of localisation prior to void nucleation induced by accumulated porosity. Lattices with localised insufficient powder melting and fusion can may have ineffective joining between some struts, which can be considered as having the same effect on mechanical response as a missing strut. The missing struts act as voids in lattice structures and failure occurs owing to shear band formation or strain localisation.

4. **Mechanism 4** involves nucleation and localisation occurring simultaneously without prior localisation owing to the growth mechanism. In this case, the onset of coalescence dictates the onset of macroscopic localisation and is caused by missing struts. One of the primary objectives of the present chapter is to demonstrate, the different degrees of a particular defect may lead to different failure mechanisms.

5. **Mechanism 5** could be considered as a subcategory of Mechanism 4, i.e. lattices with missing strut defects may have clustering of missing struts which propagates through repeated coalescence. Cluster coalescence will often take place in a region involving a few more closely

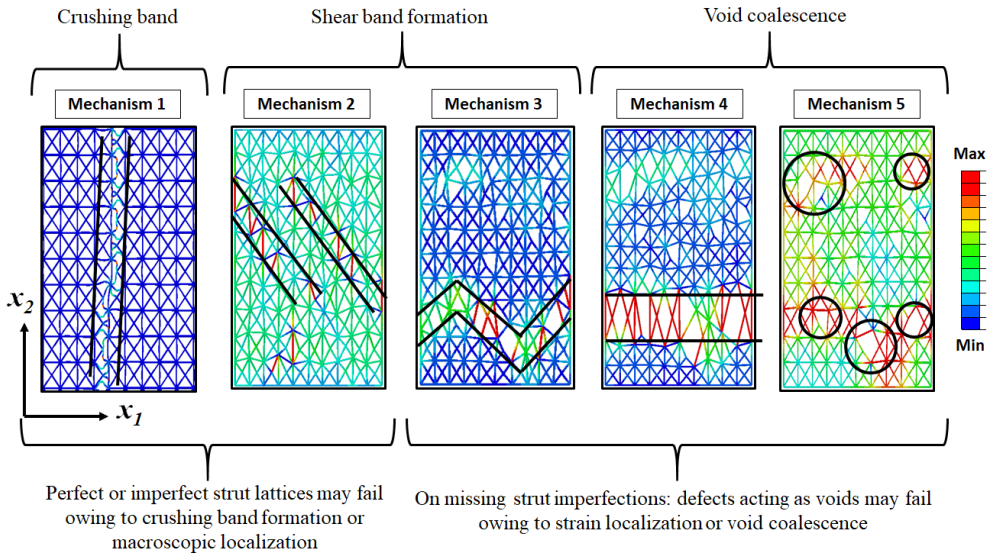

Figure 4.3: Three failure modes subdivided into five generic scenarios of localisation and void coalescence mechanisms observed in lattice structures with and without defects. In Mechanism 1, a perfect lattice is subjected to compressive loading in x_1-direction; In Mechanism 2, an imperfect lattice with 15% distortion is under tension in x_2-direction; In Mechanism 3, a lattice with 5% missing strut is under compression-tension loading with same magnitude in x_1 and x_2 directions, respectively; and In Mechanisms 4 and 5, lattices with 5% missing strut defect are subjected to biaxial tension with different magnitude. The objective of this chapter is to distinguish between failure mechanisms associated to different types of defects in FCC truss lattice metamaterials under multiaxial loadings (default ABAQUS color theme has been used to demonstrate logarithmic strain in struts)

spaced missing struts and/or experiencing large plastic strain.

4.3 Numerical framework

Existing numerical studies [130, 142] on the effects of triaxiality for two dimensional or three dimensional solids have been conducted using an implicit Finite Element (FE) solver such as ABAQUS Standard (Dassault Systemes [143]). The constant triaxiality T was imposed by utilizing a multi-point constraint with the help of user defined subroutines (MPC subroutine in ABAQUS Standard). In the MPC subroutine, user defines constraints to

be imposed between different degrees of freedom of ever-changing boundary conditions, by calculating displacements, iteratively. However, in simulations of complex lattice structures and their post buckling behaviour, the ABAQUS Standard solver may present a convergence issue. To overcome such numerical difficulties, the ABAQUS Explicit solver was employed in the current study. Since the MPC subroutine can not be employed in conjunction ABAQUS Explicit, the following methodology based on constant triaxiality was developed to simulate lattice structures.

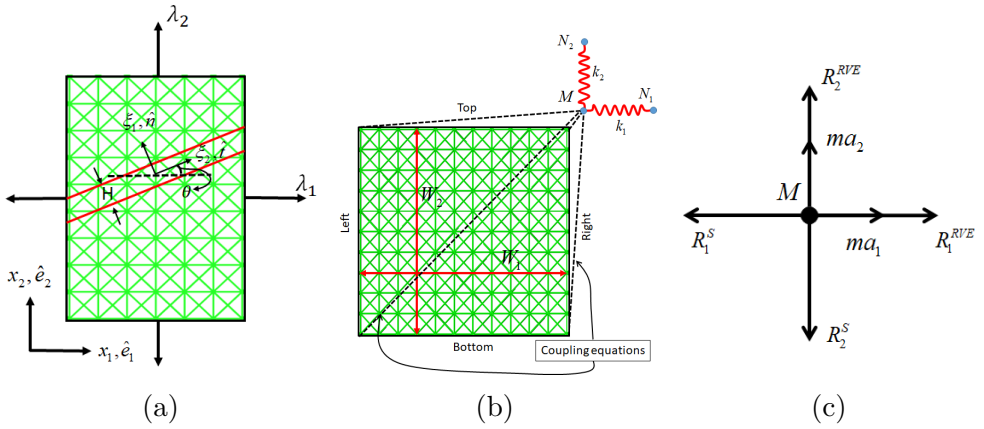

(a) (b) (c)

Figure 4.4: (a) 2-dimensional structure with predefined band subjected to multi-directional stretch, (b) the top, bottom, left and right surfaces of RVE subjected to constraints imposed by a dummy node M, so that the concentrated forces applied to node M by the springs are fully transmitted to the RVE, and (c) the free body diagram of the dummy node M, showing the forces acting on node from RVE ($R_j^{RVE}, j = 1, 2$), spring (R_j^S) and dynamic inertia (ma_j)

Numerical simulations were conducted to investigate FCC truss lattice metamaterials under plane stress as the out-of–plane thickness of a truss lattice is much smaller than the in-plane dimensions and the loads are applied in-plane. Consider the RVE of a FCC truss lattice under the global coordinate system $x_1 - x_2 - x_3$ subjected to in-plane principle stretches λ_1 and λ_2, as shown in Figure 4.4 (a), as well as principle out-of-plane stretch λ_3. The RVE consists of k_1 unit cells and has a bulk volume of Ω ($\Omega = W_1 \times W_2 \times d$) at the deformed configuration. A shear band lo-

calisation containing failed struts may form within the lattice under the stretches. Let ξ_i (i = 1, 2, 3) denote the local coordinate systems that are attached to the band with ξ_1 perpendicular to the shear band, ξ_2 aligned with the longitudinal direction, and ξ_3 aligned with x_3. I introduce vectors $\hat{\mathbf{e}}_i$ aligned with global coordinates x_i; $\hat{\mathbf{n}}$ and $\hat{\mathbf{t}}$ aligned with band local coordinates ξ_1 and ξ_2, respectively. The applied strain components in the remote area parallel to principal axes lead to stress state with principal stress components $(\Sigma_{11}, \Sigma_{22})$, i.e.

$$\mathbf{\Sigma}^0 = \Sigma_{11}\hat{\mathbf{e}}_1 \otimes \hat{\mathbf{e}}_1 + \Sigma_{22}\hat{\mathbf{e}}_2 \otimes \hat{\mathbf{e}}_2 \tag{4.3}$$

The stress triaxiality T and effective stress Σ_{eff}, describing the stress state, can be defined as

$$T = \frac{\Sigma_{11} + \Sigma_{22}}{3\Sigma_{eff}} \tag{4.4}$$

or

$$T = \frac{\text{sign}\,(\Sigma_{22})\,(1+\rho)}{3\sqrt{(\rho^2 + 1 - \rho)}} \tag{4.5}$$

where $\Sigma_{eff} = \sqrt{\frac{1}{2}\left[(\Sigma_{11} - \Sigma_{22})^2 + (\Sigma_{11})^2 + (\Sigma_{22})^2\right]}$ and $\rho = \Sigma_{11}/\Sigma_{22}$.

The numerical simulations were performed under constant T or constant ρ using the method described below. A dummy node, M, which is not part of the structure, was created to impose boundary conditions, see Figure 4.4 (b). Let u_1^M and u_2^M denote the displacements of M; (u_{left_1}, u_{left_2}), $(u_{right\_1}, u_{right\_2})$, (u_{top_1}, u_{top_2}), and $(u_{bottom\_1}, u_{bottom\_2})$ the displacement nodes on the left, right, top and bottom edges of the RVE, respectively. The displacements of the nodes on the top, bottom, left, and right edges were coupled to the corresponding displacements of node M by means of periodic

boundary conditions (PBCs) [144] defined by the following equations

$$u_{right\_1} - u_{left\_1} = u_1^M \quad \text{and} \quad u_{top\_2} - u_{bottom\_2} = u_2^M \tag{4.6}$$

In this way, the point force applied to node M is fully transmitted to the lattice structure. The macroscopic stresses acting on the lattice structure can be expressed as:

$$\Sigma_{11} = \frac{R_1^{RVE}}{A_1}, A_1 = \left(\overline{W}_2 + u_2^M\right) d \quad \text{and} \quad \Sigma_{22} = \frac{R_2^{RVE}}{A_2}, A_2 = \left(\overline{W}_1 + u_1^M\right) d \tag{4.7}$$

where R_j^{RVE} $(j = 1, 2)$ denotes the concentrated force corresponding to the x_j direction of node M; A_1 and A_2 are the areas of the left/right and top/bottom edges of the RVE, respectively; d the strut diameter; $\overline{W}_1$ and $\overline{W}_2$ widths of the RVE in the initial configuration in x_j direction. Two additional dummy nodes N_j are created and connected to dummy node M using a spring element of spring stiffness coefficient $\overline{k}_j$ (SpringA element of the ABAQUS element library [143]) as shown in Figure 4.4 (b). Hence, the force R_j^S transmitted from nodes N_j to node M can be calculated as:

$$R_j^S = \overline{k}_j \left(u_j^M - u_j^{N_j}\right) \tag{4.8}$$

where $u_j^{N_j}$ is the displacement of node N_j. Hence, the point forces acting on the RVE, R_j^{RVE}, can be calculated by applying force equilibrium (Figure 4.4 (c)).

$$R_j^{RVE} = \overline{k}_j \left(u_j^{N_j} - u_j^M \right) - ma_j \tag{4.9}$$

where m and a_j are the mass and acceleration in x_j direction at node M, respectively. Hence, to keep the stress triaxiality constant, the following parameters need to be satisfied at each incremental strain,

$$\rho = \frac{\Sigma_{11}}{\Sigma_{22}} = \text{ const } \Rightarrow \frac{\left\{ \overline{k}_1 \left(u_1^{N_1} - u_1^M \right) - ma_1 \right\} \left(\overline{W}_1 + u_1^M \right) d}{\left\{ \overline{k}_2 \left(u_2^{N_2} - u_2^M \right) - ma_2 \right\} \left(\overline{W}_2 + u_2^M \right) d} = \rho \tag{4.10}$$

If the mass m and accelerations a_j at node M are nullified by using very small mass (10^{-8}), Equation (4.10) becomes

$$\begin{aligned} &\rho = \frac{\Sigma_{11}}{\Sigma_{22}} = \text{ const } \Rightarrow \rho = \overline{\overline{k}}\overline{u} \\ &\text{with} \\ &\overline{\overline{k}} = \left\{ \frac{\overline{k}_1}{\overline{k}_2} \right\}, \quad \overline{u} = \left\{ \frac{\left(u_1^{N_1} - u_1^M \right) \left(\overline{W}_1 + u_1^M \right)}{\left(u_2^{N_2} - u_2^M \right) \left(\overline{W}_2 + u_2^M \right)} \right\} \end{aligned} \tag{4.11}$$

In the above equation, the displacement components $u_1^{N_1}$ and $u_2^{N_2}$ are prescribed values for node N_j. The displacement components of node M at each increment can be calculated through Equation (4.6). Note that, in Equation (4.11), I can tune the values of $\overline{\overline{k}}$ and $\overline{u}$ to maintain ρ constant using the method described below.

Numerical calculations suggested u_1^M and u_2^M were very small quantities, i.e. $u_j^M \ll \overline{W}_j$. Hence, I controlled $\overline{u} \approx -1$ or 1 (depending upon the state of stresses) via prescribing very large values to $u_1^{N_1}$ and $u_1^{N_2}$ ($u_1^{N_1}$=$u_2^{N_2}$). Therefore, a constant triaxiality could be maintained by maintaining a constant $\overline{\overline{k}}$. In the numerical simulations, the kinetic energy of the system

was maintained at less than 5% of its internal energy to ensure that the process was quasi-static. The ABAQUS Standard solver is not subject to convergence issue for all cases. Hence, the current methodology using ABAQUS Explicit solver was compared with ABAQUS Standard solver results for possible cases without any convergence issues. The results are presented in APPENDIX A.1, which shows that the two methodologies are comparable.

Under the principle stretches, the macroscopic logarithmic strain tensor $\mathbf{E}^0$ and rate of deformation $\dot{\mathbf{E}}^0$ read

$$\mathbf{E}^0 = E_{11}\hat{\mathbf{e}}_1 \otimes \hat{\mathbf{e}}_l + E_{22}\hat{\mathbf{e}}_2 \otimes \hat{\mathbf{e}}_2 + E_{33}\hat{\mathbf{e}}_3 \otimes \hat{\mathbf{e}}_3 \tag{4.12}$$

$$\dot{\mathbf{E}}^0 = \dot{E}_{11}\hat{\mathbf{e}}_1 \otimes \hat{\mathbf{e}}_1 + \dot{E}_{22}\hat{\mathbf{e}}_2 \otimes \hat{\mathbf{e}}_2 + \dot{E}_{33}\hat{\mathbf{e}}_3 \otimes \hat{\mathbf{e}}_3 \tag{4.13}$$

where the components of the two tensors can be calculated as:

$$E_{ii} = \frac{1}{\Omega}\int_\Omega \varepsilon_{ii} d\Omega = \ln \lambda_i, \quad \dot{E}_{ii} = \frac{1}{\Omega}\int_\Omega \dot{\varepsilon}_{ii} d\Omega = \frac{1}{\lambda_i}\dot{\lambda}_i \tag{4.14}$$

where ε_{ii} $(i = 1, 2, 3)$ denotes the microscopic logarithmic strain within the RVE. Next, I consider strain inside the shear band. At the current configuration, the averaged logarithmic strain inside the band of thickness H at an angle θ , with respect to coordinate x_1 (Figure 4.4 (a)), is equal to the sum of uniform strain in remote area plus the additional strain associated with additional band displacements Δ_1 and Δ_2 under the local coordinates ξ_i $(\hat{\Delta} = \Delta_1\hat{t} + \Delta_2\hat{n})$. The averaged logarithmic strain rate tensor within the band $\dot{\mathbf{E}}^b$ can be written as:

$$\dot{\mathbf{E}}^b = \dot{\mathbf{E}}^0 + \left(1 - \frac{\Omega_b}{\Omega}\right)\left(\frac{\dot{\Delta}_1}{H}\hat{\mathbf{t}} + \frac{\dot{\Delta}_2}{H}\hat{\mathbf{n}}\right) \otimes \hat{\mathbf{n}} = f\left(\dot{\lambda}_1, \dot{\lambda}_2, \dot{\Delta}_1, \dot{\Delta}_2, \theta\right) \quad (4.15)$$

The following method was employed to calculate $\dot{\mathbf{E}}^b$ in the simulations. Let Ω^b denote the volume of a shear band at the deformed configuration, see Figure 4.4 (a). The averaged logarithmic strain rate tensor in the band can be described as:

$$\dot{\mathbf{E}}^b = \dot{E}^b_{ij}\hat{\mathbf{e}}_i \otimes \hat{\mathbf{e}}_j \quad (4.16)$$

with the components of the tensor calculated as:

$$\dot{E}^b_{ij} = \frac{1}{\Omega^b}\int_{\Omega^b} \dot{\varepsilon}^b_{ij} d\Omega \quad (4.17)$$

where $\dot{\varepsilon}^b_{ij}$ denotes the microscopic logarithmic strain rate within the band. The formation of localisation in lattice structures is difficult to visualize due to the presence of randomly distributed defects in a large domain. To calculate ε^b_{ij} and visualize band strain, the nodal displacements at joints of FCC truss lattices were extracted from the detailed FE solutions and used as the input to create a continuum plot of the displacement field using 2D triangular solid elements. The microscopic strain tensor inside the band can be calculated using the finite element formulation described in APPENDIX A.2.

The ratio between the equivalent strain within the band E^b_{eq} and macroscopic equivalent strain E_{eq} plays an important role in the identification of failure mechanisms, i.e.

$$E^b_{eq}/E_{eq} = \phi\left(\dot{\lambda}_1, \dot{\lambda}_2, \dot{\Delta}_1, \dot{\Delta}_2, \theta\right) \tag{4.18}$$

The additional band displacements Δ_1, Δ_2 and shear band angle θ would vanish if no localisation takes place in lattice structure. The accumulated equivalent logarithmic strain within the band and far field can be defined by Hill's equivalent strain [145], derived below.

4.3.1 Plastic collapse surface and effective stress-strain

The theoretical framework to construct continuum constitutive model for octet-truss lattice materials were provided by [146]. The same methodology is being used to obtain elastic properties of FCC truss lattice. The FCC unit cell along with its unit vectors is sketched in Figure 4.5. Let $\mathbf{N}$ define the linear transformation that relates macroscopic strains to microscopic strains under small strain deformation. The components of $\mathbf{N}$ can be determined by the components of tensor for the strut member, i.e.

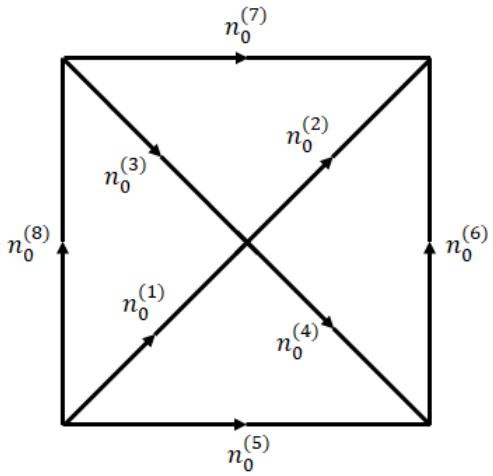

Figure 4.5: FCC unit cell and its unit vectors

$$\{\mathbf{N}\}_{ij} = \begin{cases} \left\{ n_0^{(i)} \otimes n_0^{(i)} \right\}_{jj}, & \text{for } j = 1, 2 \\ \left\{ n_0^{(i)} \otimes n_0^{(i)} \right\}_{12}, & \text{for } j = 3 \end{cases} \tag{4.19}$$

where unit vector $n_0^{(i)}$ is aligned with the initial direction of the longitudinal axis of the strut. The macroscopic strain vector, $\mathrm{E} = [E_{11}, E_{22}, 2E_{12}]$, and microscopic strain vector, $\varepsilon = [\varepsilon^{(1)}, \varepsilon^{(2)}, \varepsilon^{(3)}, \varepsilon^{(4)}, \varepsilon^{(5)}, \varepsilon^{(6)}, \varepsilon^{(7)}, \varepsilon^{(8)}]$ can be summarized as:

$$\varepsilon = \mathbf{N}\mathrm{E} \tag{4.20}$$

The macroscopic stress vector, $\Sigma = [\Sigma_{11}, \Sigma_{22}, \Sigma_{12}]$, can be written using transpose of localised strain matrix in the form of microscopic stress vector, $\sigma = \left[\sigma^{(1)}, \sigma^{(2)}, \sigma^{(3)}, \sigma^{(4)}, \sigma^{(5)}, \sigma^{(6)}, \sigma^{(7)}, \sigma^{(8)}\right]$:

$$\Sigma = \mathbf{c}_0 \mathbf{N}^T \sigma \tag{4.21}$$

At macroscale, the elastic stress-strain relationship can be given as:

$$\Sigma = \mathbf{K}\mathrm{E}, \quad \text{or} \quad \mathrm{E} = \mathbf{K}^{-1}\Sigma \tag{4.22}$$

where $\mathbf{K}$ is the symmetric macroscopic stiffness tensor of the lattice material and is given as:

$$\mathbf{K} = E\mathbf{c}_0 \mathbf{N}^T \mathbf{N} \tag{4.23}$$

where $\mathbf{c_0}$ is the diagonal matrix consisting volume fractions of each struts

and E is elastic modulus of the parent material.

Table 4.1: Components $n^{(i)_1}$ and $n^{(i)_2}$ of i^{th} unit vectors $n^{(i)}$ of individual beam members within unit cell

	$n_0^{(1)}$	$n_0^{(2)}$	$n_0^{(3)}$	$n_0^{(4)}$	$n_0^{(5)}$	$n_0^{(6)}$	$n_0^{(7)}$	$n_0^{(8)}$
$n_1^{(i)}$	$1/\sqrt{2}$	$1/\sqrt{2}$	$1/\sqrt{2}$	$1/\sqrt{2}$	1	0	1	0
$n_2^{(i)}$	$1/\sqrt{2}$	$1/\sqrt{2}$	$-1/\sqrt{2}$	$-1/\sqrt{2}$	0	1	0	1

Components of unit vector of unit cell are given in Table 4.1 and from this stiffness tensor of FCC truss lattice can be given as

$$\mathbf{K} = \begin{bmatrix} K_{11} & K_{12} & K_{13} \\ K_{21} & K_{22} & K_{23} \\ K_{31} & K_{32} & K_{33} \end{bmatrix} = E \begin{bmatrix} 0.0354 & 0.0146 & 0 \\ 0.0146 & 0.0354 & 0 \\ 0 & 0 & 0.0146 \end{bmatrix} \tag{4.24}$$

From Equations (4.20) to (4.23) at microscale under elastic limit stress tensor can be rewritten as:

$$\sigma = \mathrm{N}\mathbf{K}^{-1}\Sigma \tag{4.25}$$

This microscopic stress equation has been used to establish plastic yielding of struts. I calculated plastic collapse surface of the FCC truss lattice under combination of multiaxial loadings and proceed to establish a Hill's model-based calculation of the equivalent plastic strain as given below.

4.3.2 Plastic collapse surface

In the analytical solution I have assumed that the struts are pin-jointed and made from rigid, ideally plastic material. The accuracy of analytical solution has been validated using FE calculations. In the FE analysis each uniform cylindrical strut has been modelled by 50 Timoshenko beam elements (B21 element in ABAQUS) and has equal length in horizontal and vertical direction. The strength of stretch dominated lattice structure with

10% relative density shows three times stronger than the foam compared to bending dominated foams [147, 148]. Hence the value of relative density has been taken as 0.10 for our investigation [149]. The material was assumed to be elastic-plastic following Ramberg-Osgood Equation with hardening exponent $n = 100$ during FE calculations. The FE simulations has been terminated when local strut stress reaches yield stress $\sigma_y = 168$MPa of parent material. The macroscopic collapse stress is calculated from Equation (4.25) equating microscopic stress to yield stress.

To calculate the yield surface under the combination of Σ_{11} and Σ_{22}, Equation (4.25) was employed with $\Sigma_{12} = 0$, i.e.

$$\begin{aligned} \sigma^{(1)} = \sigma^{(2)} = \sigma^{(3)} = \sigma^{(4)} = 10\Sigma_{11} + 10\Sigma_{22} = |\sigma_y| \\ \sigma^{(5)} = \sigma^{(7)} = 34\Sigma_{11} - 14\Sigma_{22} = |\sigma_y| \\ \sigma^{(6)} = \sigma^{(8)} = -14\Sigma_{11} + 34\Sigma_{22} = |\sigma_y| \end{aligned} \tag{4.26}$$

Similarly, to calculate yield surface under pure shear ($\Sigma_{11} = \Sigma_{22} = 0, \Sigma_{12} \neq 0$), i.e.

$$\begin{aligned} \sigma^{(1)} = \sigma^{(2)} = 34\Sigma_{12} = |\sigma_y| \\ \sigma^{(3)} = \sigma^{(4)} = -34\Sigma_{12} = |\sigma_y| \\ \sigma^{(5)} = \sigma^{(6)} = \sigma^{(7)} = \sigma^{(8)} = 0 \end{aligned} \tag{4.27}$$

where $\sigma^{(i)}$ is local axial stress of i^{th} strut shown in Figure 4.5. The macroscopic yield stresses were calculated for a variety of proportional stress paths and plotted in the relevant stress space to give the plastic collapse surface. The plastic collapse surface under combinations of applied stress $(\Sigma_{11}, \Sigma_{22})$ obtained from Equations (4.26) and (4.27) has been plotted in Figure 4.6.

The FE calculations has been included in Figure 4.6 shows good agreement with analytical solution. Note that plastic collapse of FCC truss lattices is driven by horizontal and vertical struts in this space, which has also been

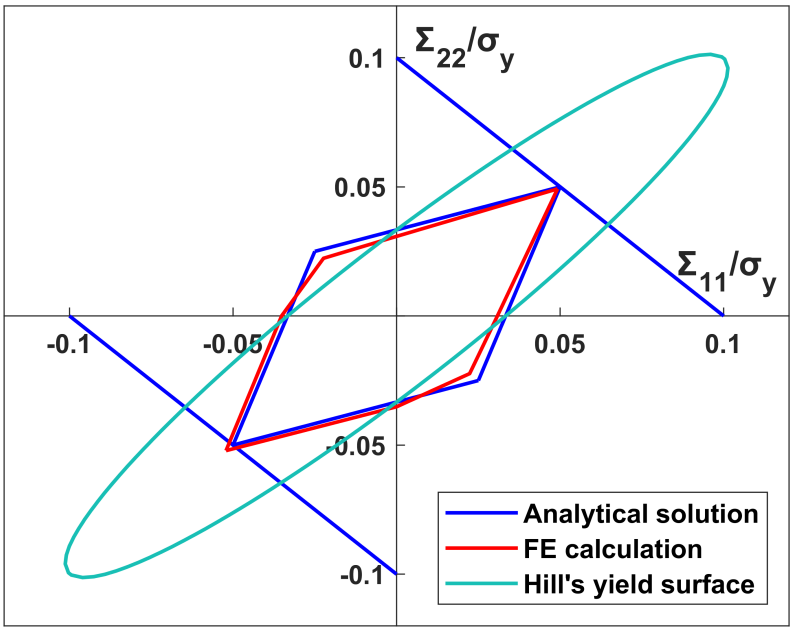

Figure 4.6: Comparison between the analytical, FE and Hill's yield criterion predictions of plastic collapse surface

observed in FE calculations.

4.3.3 Anisotropic plastic strain

In this section I will use Hill's generalisation of von Mises yield criterion for materials with anisotropic property. With respect to the principal axes of anisotropy, Hill's yield criteria have the form:

$$\Phi \equiv \Sigma_{eq}^2 - 1 = 0 \tag{4.28}$$

where the applied macroscopic stress is characterized by the equivalent stress measure given by for 2-dimensional space [150]:

$$\Sigma_{eq} = \sqrt{(G+H)\Sigma_{11}^2 + (F+H)\Sigma_{22}^2 - 2H\Sigma_{11}\Sigma_{22} + 2I\Sigma_{12}^2} \tag{4.29}$$

In above equation F, G, H, and I are material constants which characterize the degree of anisotropy and can be expressed as [145]:

$$\begin{aligned} F &= \frac{(\sigma_y)^2}{2}\left[\frac{1}{\left(\Sigma^y_{22}\right)^2}+\frac{1}{\left(\Sigma^y_{33}\right)^2}-\frac{1}{\left(\Sigma^y_{11}\right)^2}\right] \\ G &= \frac{(\sigma_y)^2}{2}\left[\frac{1}{\left(\Sigma^y_{33}\right)^2}+\frac{1}{\left(\Sigma^y_{11}\right)^2}-\frac{1}{\left(\Sigma^y_{22}\right)^2}\right] \\ H &= \frac{(\sigma_y)^2}{2}\left[\frac{1}{\left(\Sigma^y_{11}\right)^2}+\frac{1}{\left(\Sigma^y_{22}\right)^2}-\frac{1}{\left(\Sigma^y_{33}\right)^2}\right] \\ I &= \frac{3(\sigma_y)^2}{2\left(\Sigma^y_{12}\right)^2} \end{aligned} \tag{4.30}$$

From Equations (4.26) and (4.27) one can calculate uniaxial and shear yield strengths $(\Sigma^y_{11}, \Sigma^y_{22}, \Sigma^y_{12})$ with respect to material principal axes. The out of plane yield strength has been taken as $\Sigma^y_{33} = 0.1\sigma_y$ (0.1 is the relative density of FCC truss lattice) to calculate material constants. Equation (4.29) has been plotted in Figure 4.6 and shows a reasonably good agreement with analytical and FE solutions under combination of tension and compression. However, it dramatically overestimates the yield surface under biaxial tension and compression. The Hill's criterion has been explored to show FCC truss lattice anisotropic behaviour and to establish equivalent plastic strain equation for anisotropic material. From these parameters the equivalent plastic strain of an anisotropic material can be calculated, using work conjugation given as [145]:

$$\begin{aligned} E_{eq} = \Bigg\{ \frac{1}{FH+FG+GH}[&(F+H)\left(E_{11}\right)^2 + 2H\left(E_{11}E_{22}\right) + \\ &(G+H)\left(E_{22}\right)^2 + \frac{2\left(E_{12}\right)^2}{I}] \Bigg\}^{1/2} \end{aligned} \tag{4.31}$$

The above equation has been extensively used to quantify localisation and coalescence.

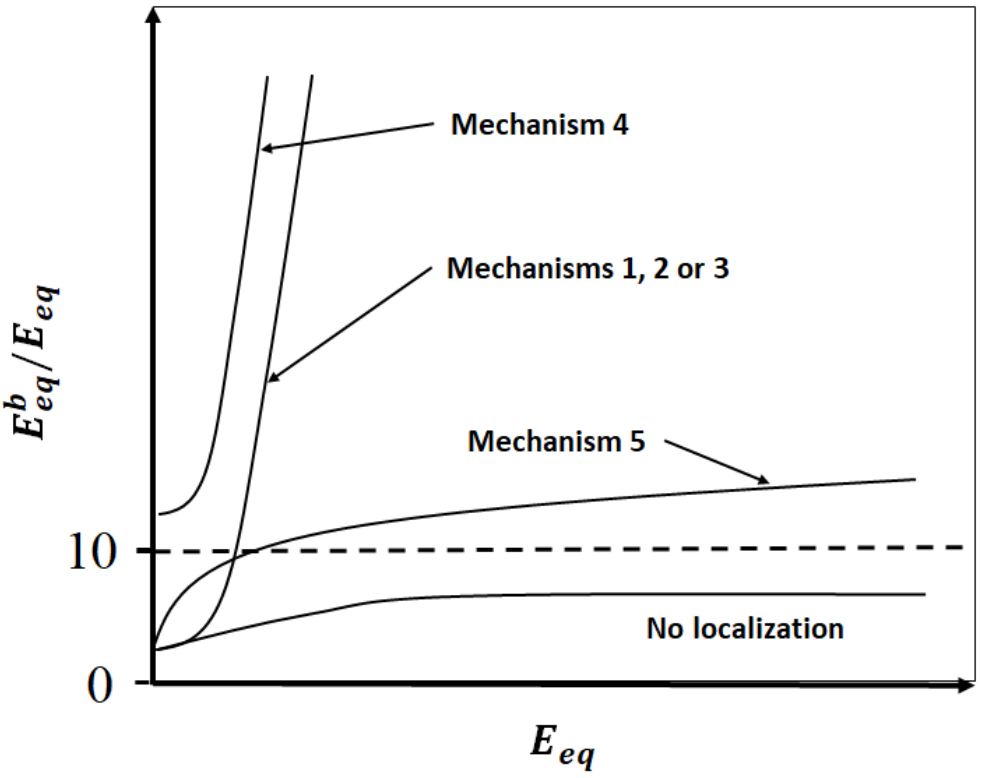

Figure 4.7: Schematic diagram of evolution of normalised equivalent band strain against equivalent remote strain

4.3.4 Failure mechanisms criterion

Macroscopic localisation occurs when parts of a lattice in a band plastically deform while remote regions remain elastic. This criterion is used to identify localisation of the structure, i.e. (1) when E^b_{eq}/E_{eq} increases exponentially, the onset of localisation occurs; and (2) when E^b_{eq}/E_{eq} exceeds the threshold value of 10 the onset of coalescence occurs [128]. Figure 4.7 is a schematic plot of the evolution of strain inside a localisation band with respect to the remote strain. Mechanisms 1, 2, and 3 are crushing/shear band formation and failure is by crushing/shear band formation, where E^b_{eq}/E_{eq} increases exponentially. In case of failure dictated by onset of coalescence the value of E^b_{eq}/E_{eq} starts at a higher than the threshold value and failure occurs owing to Mechanism 4. In Mechanism 5 the value of E^b_{eq}/E_{eq} increase monotonically above the threshold as E_{eq} increases.

4.3.5 Finite element model

The struts of the FCC truss lattice metamaterials (Figure 4.2) have been modelled as 2 -node Timoshenko-beam element (B21 in ABAQUS notation) with rigid connections between struts. In the numerical simulations, each strut is modelled as a uniform circular cross sectioned solid bar of diameter d, with equal length and height ($l = h$) for perfect lattice. The relative density $\overline{\rho}$ of the FCC unit cell truss lattice material (ratio of the density of the lattice material to the density of the solid material from which it is made) is given by

$$\overline{\rho} = (1 + \sqrt{2}) \left(\frac{\pi}{2}\right) \left(\frac{d}{l}\right) \tag{4.32}$$

The strength of a stretch dominated lattice structure with 10% relative density is three times stronger than to an equivalent bending dominated foams [147, 148]. Thus, the value of the relative density was taken as 0.10 ($d = 0.528$ mm, $l = 20$ mm) for our investigation, taking manufacturability of the minimum strut diameter into consideration [149]. Numerical tests have suggested that with each strut meshed with 5 beam elements of equal length, the deviation in the macroscopic stiffness was within 3% compared to 10 beam elements. Failure events, such as first localisation and void coalescence, have been observed to occur at small strains (< 0.01), and the struts have not been found to be in contact during deformation. Hence, contact among struts owing to large deformation has not been modelled. Further numerical studies have suggested that distorted struts have negligible effect on the relative density and for lattices with missing struts, a constant relative density has been achieved by a slight increase in the diameter of the struts.

4.3.6 Material model

The Ramberg-Osgood model, Equation (4.33), was used to represent the true stress-strain relationship of the material in the numerical study, as illustrated in Figure 4.8 [151].

$$\bar{\varepsilon} = \frac{\bar{\sigma}}{\bar{E}} + \kappa\left(\frac{\bar{\sigma}}{\bar{\sigma}_y}\right)^n \tag{4.33}$$

where $\bar{E}$ = 71300MPa MPa and $\bar{\sigma}_y$ = 168 MPa are parent material's Young's modulus and yield stress, respectively; $\kappa = 0.002$ is the yield offset and $n = 9.9$ is the hardening exponent. This material model is suitable to capture the mechanical behaviour of aerospace-grade lightweight aluminum alloys such as AlSi10Mg alloy.

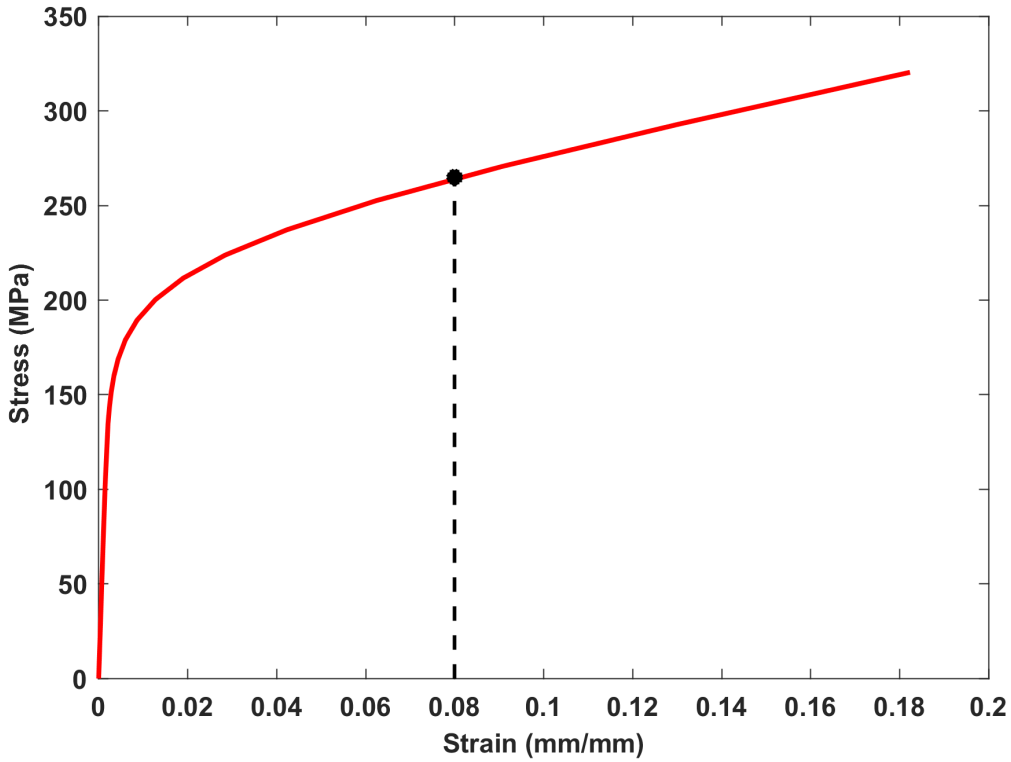

Figure 4.8: Stress strain curve of the parent material with failure strain ($\varepsilon_f = 0.08$) used for the FE analysis

To study failure mechanisms, the local tensile strain (LTS) criterion was employed in the numerical study. Materials such as high strength aluminum

alloys fail due to shear localisation when the maximum tensile strain is reached, hence the LTS criterion is appropriate for this study. Rosenthal et al. [151] showed elongation at failure varied between 8-9% for AlSi10Mg specimens manufactured using LPBF. Hence, it is assumed that when the maximum tensile strain in a lattice reaches a failure strain of $\varepsilon_f = 0.08$, failure occurs, and the simulation is terminated. It is noted that material damage has not been considered in the above-mentioned constitutive model.

4.3.7 Representative volume element (RVE)

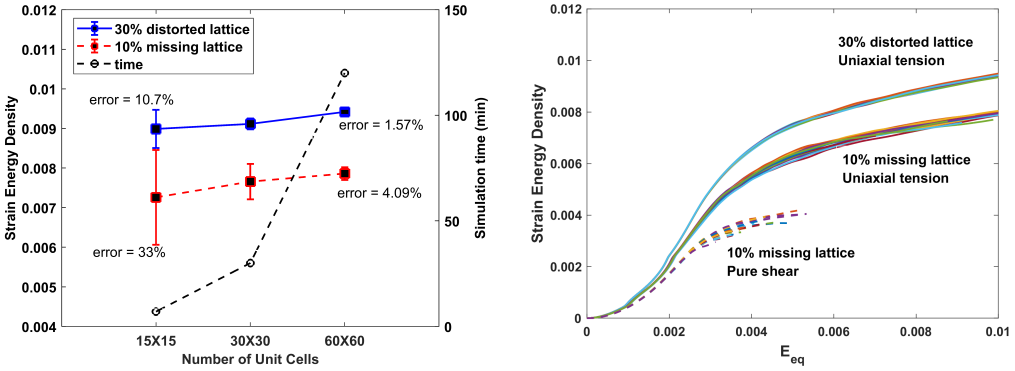

(a) (b)

Figure 4.9: (a) Strain energy density convergence plot verses number of unit cells in RVE with 30% distorted and 10% missing lattices at $E_{eq} = 0.01$ and simulation time verses unit cells under uniaxial tension, and (b) strain energy density as a function of equivalent strain for RVE containing 60×60 unit cells, with 30% distorted struts and 10% missing struts, under uniaxial tension and pure shear.

An RVE should contain sufficient unit cells to be representative of the bulk mechanical behaviour and lattice failure mechanisms but be minimized to prevent excessive computational cost. Cohen et al. [152] stated that equilibrium solutions in the non-linear regime are not unique, and therefore the response of a truss lattice can depend significantly on the RVE size. To predict the non-linear behaviour of a truss lattice structure, several RVEs comprising increasing number of unit cells must be numerically tested until

convergence is obtained. Therefore, numerical simulations were conducted to evaluate the effect of the size of RVE. The increase in computational time with respect to increase in number of unit cells is shown in 4.9 (a). The strain energy densities under uniaxial tension with equivalent strain $E_{eq} = 0.01$ were calculated for the RVEs containing 15×15, 30×30 and 60×60 unit cells with two types of defect; 30% distorted and 10% missing struts, as shown in Figure 4.9 (a). During the simulations, all the lattices and their respective imperfections were generated using the algorithm described in Section 4.2 with 20 repetitions. The results suggest that (i) the strain energy density for the RVE containing 60×60 unit cells can converge to within 5% deviation; (ii) the variation of strain energy density for distorted imperfection is much less than that of missing struts imperfection for RVEs containing 15×15 and 30×30 unit cells. Figure 4.9 (b) shows the strain energy density as a function of equivalent strain for the RVE containing 60×60 unit cells with 30% distorted struts and 10% missing struts, under uniaxial tension and pure shear. Again, the results confirm the convergence of strain energy density for the RVE containing 60×60 unit cells. Henceforth, all the numerical simulations have been carried out using the RVE containing 60×60 unit cells.

4.4 Results and discussion

4.4.1 Effect of imperfections on elastic and shear modulus

Figure 4.10 shows the effects of imperfection on macroscopic stiffness for 20 different RVE resolutions using the method described in Section 4.2. K_{ij} and K^*_{ij} denote the components of the microscopic stiffness tensor defined in Equation (4.25), for the perfect and imperfect lattices, respectively. The

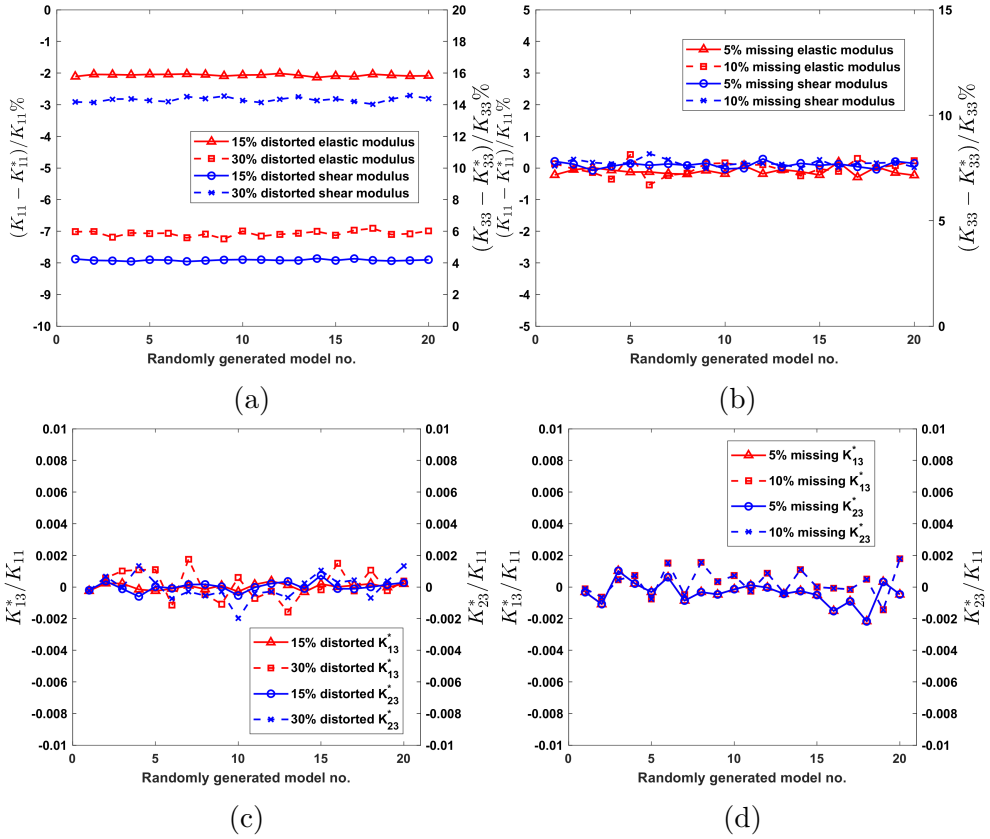

Figure 4.10: Macroscopic elastic and shear modulus variation due to defects in FCC truss lattices (a) for distorted struts, (b) for missing struts, and orthotropic material properties variation due to defects in FCC truss lattices, (c) for distorted struts, and (d) for missing struts with respect to perfect lattice.

percentage differences have been calculated against the perfect lattice. As the irregularity increases in lattice structures, there are up to 7% decrease in elastic modulus, and up to 14% increase in shear modulus for distorted defects, whereas no significant changes have been observed in elastic modulus for missing strut defects. A perfect FCC truss lattice exhibits in-plane orthotropic material behaviour, i.e. $K_{13} = K_{31} = 0, K_{23} = K_{32} = 0$. Figures 4.10 (c) and (d) show the variations of K^*_{13} and K^*_{23} normalised by K_{11}, which suggests that defects can only incur small variations of K^*_{13} and K^*_{23}. As $K^*_{13} = K^*_{31}$ and $K^*_{23} = K^*_{32}$, the results confirm that the material remains in-plane orthotropic after incorporating the defects.

4.4.2 Effect of imperfections on failure locus

Figure 4.11 (a) shows the failure loci of FCC truss lattice metamaterials under multiaxial loadings obtained by FE simulations. Four quadrants of the failure loci have been plotted for the perfect, 15% distorted and 5% missing struts lattices, respectively. The lattices were subjected to (1) biaxial tension in the first quadrant, (2) biaxial compression in the third quadrant and (3) combination of tension and compression loadings in the second and fourth quadrants. The failure loci are approximately symmetrical about the line where triaxiality $T = -0.67$ and $T = 0.67$. It is evident that lattice imperfection significantly reduces the failure stress within the first quadrant; whereas the effect of imperfection is less pronounced in the other quadrants. In the first quadrant $\Sigma_{11} \geq 0, \Sigma_{22} \geq 0$, the failure stress of the perfect lattice is significantly higher than the imperfect lattices as there is not any arbitrary change in load path and, hence, no localisation occurs. In the second quadrant, $\Sigma_{11} \leq 0, \Sigma_{22} \geq 0$, the failure mechanisms of crushing band and shear band (Mechanisms 1, 2, 3, and 4) dictate failure for all types of lattices, resulting in an insignificant impact on the failure strength between the different lattices. In the third quadrant, $\Sigma_{11} \leq 0, \Sigma_{22} \leq 0$ and triaxiality $T < -0.2$, the perfect and imperfect lattices all fail owing to the formation of a crushing band (Mechanism 1) under compression; this shows that, both the stress triaxiality and initial imperfections have significant effects on the failure mechanisms in other quadrants. Figure 4.11 (b) shows two distinct functional relations between triaxiality T and stress ratio ρ, i.e., $\Sigma_{22} > 0$ and $\Sigma_{22} < 0$. In the following sections, our discussion will focus on the failure mechanisms in the first and second quadrants owing to the symmetric nature of the failure loci: this corresponds to the scenarios with $T \in [-0.2, 0.67]$ and $\Sigma_{22} > 0$.

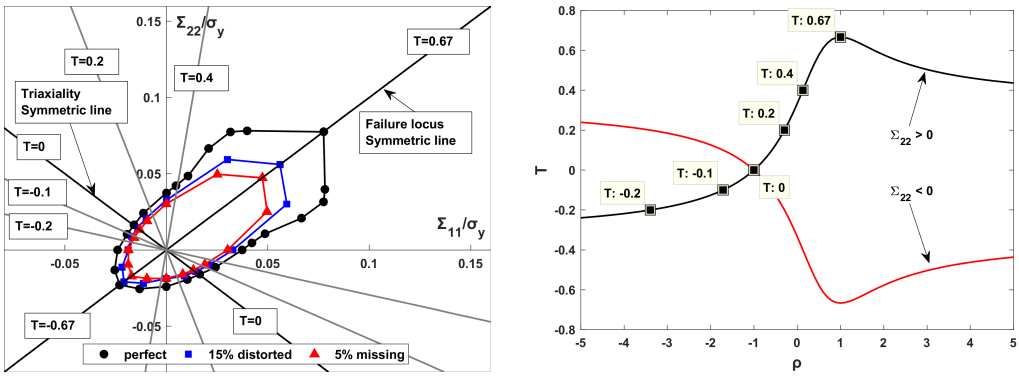

(a) (b)

Figure 4.11: (a) Failure locus of perfect and imperfect lattice structures and (b) stress triaxiality verses stress ratio taken for numerical simulations.

4.4.3 An illustrative example - pure shear loading ($T = 0$)

In this section the mechanical response and failure mechanisms are discussed for various different lattice cases; a perfect lattice and imperfect lattices with distorted strut defects (15% and 30%) and missing struts (5% and 10%), subjected to a constant triaxiality ($\Sigma_{11} = -\Sigma_{22}, T = 0$, pure shear loading). Results will be presented for the effect of stress triaxiality in later sections.

Figure 4.12 (a) shows the normalised effective stress as a function of remote equivalent strain, E_{eq}, for perfect and imperfect lattices. The perfect lattice has the highest load carrying capacity and ductility. The missing strut defects cause the lattice to fail at much lower effective strains and lower stresses than the corresponding lattices with distorted strut defects. Figure 4.12 (b) shows the normalised equivalent band strain, E^b_{eq}/E_{eq}, as a function of the remote equivalent strain, E_{eq}, for the perfect lattice and imperfect lattices with selected imperfections. The failure points of the lattices are marked as 'filled circle' on the curves. The failure mechanisms of the perfect lattice, imperfect lattices with the 30% distorted strut defects and the 10% missing strut defects are shown in Figures 4.12 (c) to

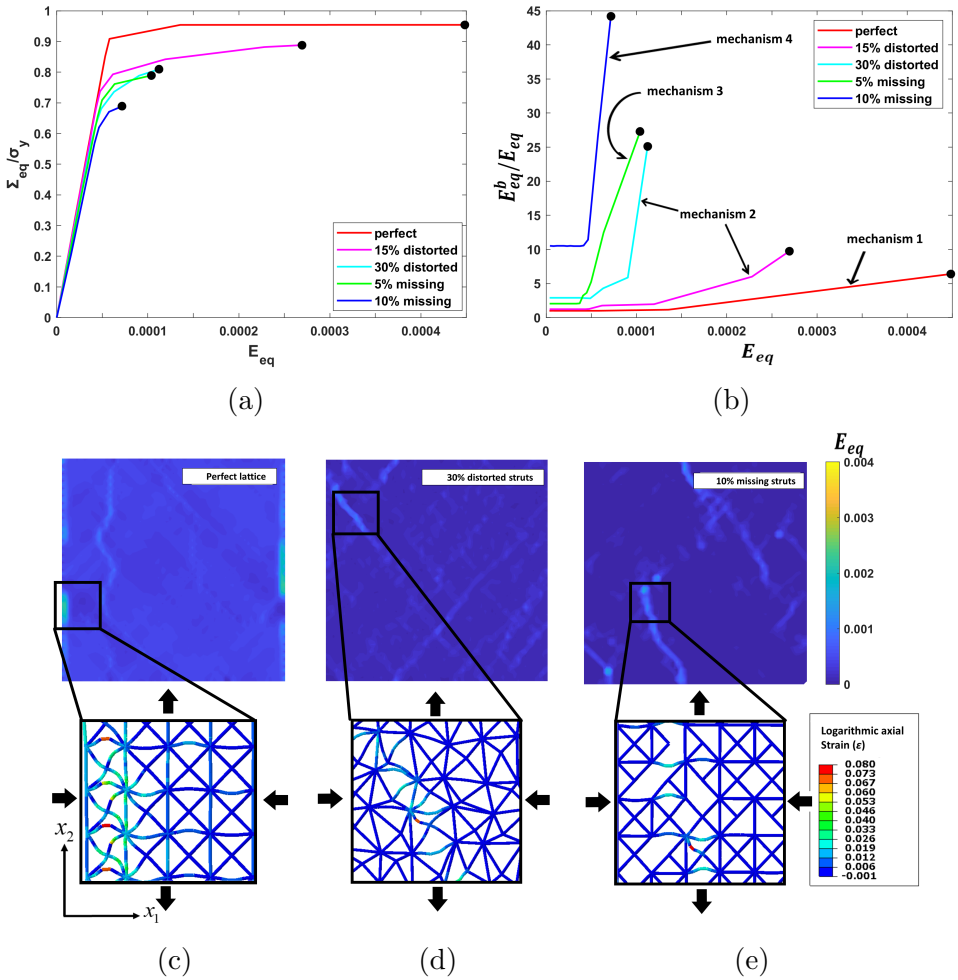

(a) (b)

(c) (d) (e)

Figure 4.12: Failure mechanisms comparison of lattices under pure shear (a) variation of normalised macroscopic stress against equivalent remote strain of perfect and imperfect lattices; (b) evolution of normalised equivalent band strain against equivalent remote strain of perfect and imperfect lattices; (c), (d) and (e) equivalent strain continuum plots of RVE, when the maximum strain reached ($\varepsilon_f = 0.08$) for prefect, 30% distorted and 10% missing strut lattices, respectively.

(e), respectively. Equivalent strain continuum plots are shown, as well as detailed views of the failed areas. To calculate equivalent strain, the nodal displacements at the joints of the FCC truss lattices were extracted from the FE solutions and used as inputs to calculate strain at each integration point, using 2D triangular solid elements (APPENDIX A.2). There is no shear localisation in the perfect lattice and failure occurs due to crushing band formation (Mechanism 1) under compressive stress ($\Sigma_{11} = -\Sigma_{22}$) with the maximum normalised equivalent band strain less than 5. Strain localisation occurred in the lattices with the 15% and 30% distorted strut and missing strut imperfections, respectively. For the 10% missing struts lattices, the normalised equivalent band strain is around 10 at the onset of shear band formation (Figure 4.12 (b)), which suggests that void coalescence dictates the start of macroscopic localisation (Mechanism 4). For the imperfect lattices with 15%, 30% distorted struts and 5% missing struts, the normalised equivalent band strains are less than 5 before the onset of shear band formation (Figure 4.12 (b)), which suggests that the strain localisation is not dictated by the onset of coalescence.

4.4.4 The effect of stress triaxiality on failure localisation

The effect of triaxiality on failure mechanisms is investigated in this section through comparison of the behaviour of (1) a perfect lattice and imperfect lattices with 15% distortion (Figure 4.13 (a)) and 5% missing struts (Figure 4.13 (b)); (2) imperfect lattices with 15% and 30% distortion (Figure 4.13 (c)); and (3) imperfect lattices with 5% and 10% missing struts (Figure 4.13 (d)). In these figures, the normalised equivalent band strain, E^b_{eq}/E_{eq}, is plotted as a function of the remote effective strain, E_{eq}. To facilitate interpretation of the results, Figures 4.14 and 4.15 show the continuum plots

and details of the failed areas for the imperfect lattices with 15% distortion and 5% missing strut imperfections, respectively, at selected triaxialities.

Perfect lattice - For triaxialities $T \leq 0$, the perfect lattice has a high normalised equivalent band strain which shows failure due to crushing band formation under compression. For triaxialities $T > 0$, the perfect lattice tends to fail at very high macroscopic strain and does not show any strain localisation dominated failures.

15% distorted lattice - For the 15% distorted strut lattice, the maximum normalised equivalent band strain is higher or close to 10 at triaxialities $T < 0$, which signifies the occurrence of strain localisation. As shown in Figure 4.14 (a) at triaxiality $T = -0.2$, the lattice fails owing to crushing band formation (Mechanism 1). A band of localised high strain can be seen in both the continuum plot and detailed beam element figure. It can also be observed that from Figures 4.14 (b) and (c) (triaxialities $T = -0.1$ and 0), the structure fails due to shear band localisation (Mechanism 2). From triaxialities $T > 0$, strain localisation does not occur, and multiple high equivalent strain areas can be observed (Figures 4.14 (d), (e) and (f)).

5% missing struts - For all triaxialities, the 5% missing strut lattices (Figure 4.13 (b)) show failure occur due to strain localisation. The normalised equivalent band strain is less than 5 before onset of the shear band formation, which suggests that the strain localisation is not dictated by the onset of coalescence (i.e. Mechanism 3). At triaxiality $T = -0.2$ (Figure 4.15 (a)), compressive loading pre-dominates, and lattice struts fail owing to crushing band formation (Mechanism 1). At triaxialities $T = -0.1$, 0 and 0.1 (Figures 4.15 (b) to (d)), shear strain localisation (Mechanism 3) becomes noticeable. At triaxiality $T = 0.4$, the normalised equivalent band strain does not increase exponentially and strain localisation is dictated by the cluster localisation (Figure 4.15 (e), Mechanism 5) and at triaxiality $T = 0.67$, the normalised equivalent band strain is below the threshold

value hence no localisation occurs (Figure 4.15 (f)).

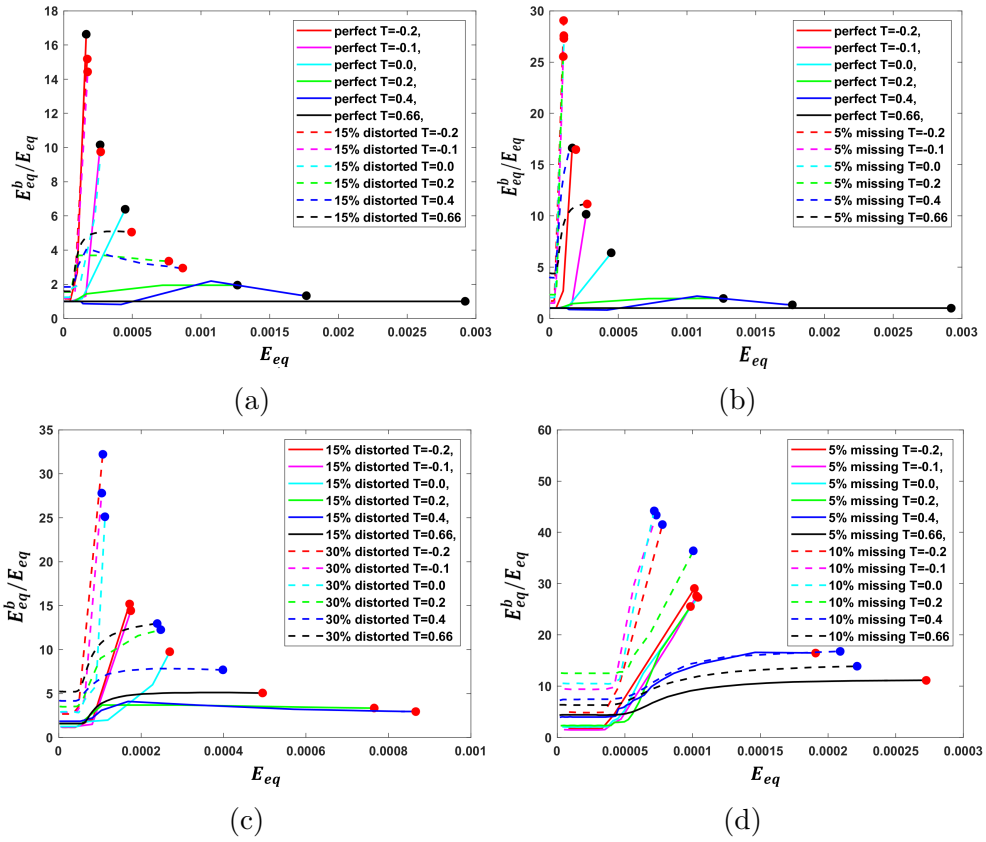

Figure 4.13: Evolution of equivalent band strain with varying triaxiality from -0.2 to 0.67. Comparison for (a) perfect vs 15% distorted struts, (b) perfect vs 5% missing struts, (c) distorted struts 15% vs 30% and (d) missing struts 5% vs 10%

30% distorted lattice - For triaxiality $T < 0$, the failure mechanisms for the 30% distorted lattice are similar to those of the 15% distorted lattices (Figure 4.13 (c)) i.e. Mechanisms 1 and 2. For triaxiality $0 \leq T \leq 0.4$, the maximum normalised equivalent band strain for the 30% distorted lattice is much higher than that for the 15% distorted lattice, which indicates strain localisation dominated failure. At triaxiality $T = 0.67$, strain localisation does not occur, and multiple high equivalent strain areas form, as with the 15% distorted lattice.

10% missing struts - The 10% missing struts lattice fails on the formation of a crushing band at triaxiality $T = -0.2$. For triaxialities $T = -0.1$, 0 and 0.2, the normalised equivalent band strains are higher than 10 before

onset of the strain localisation (Figure 4.13 (d)), which suggest that void coalescence dictates the onset of strain localisation (Mechanism 4). For triaxialities $T = 0.4$ and 0.67, the normalised equivalent band strains do not increase exponentially, and the maximum normalised equivalent band strains are more than 10, which suggests that the strain localisation is dictated by the cluster localisation (Mechanism 5).

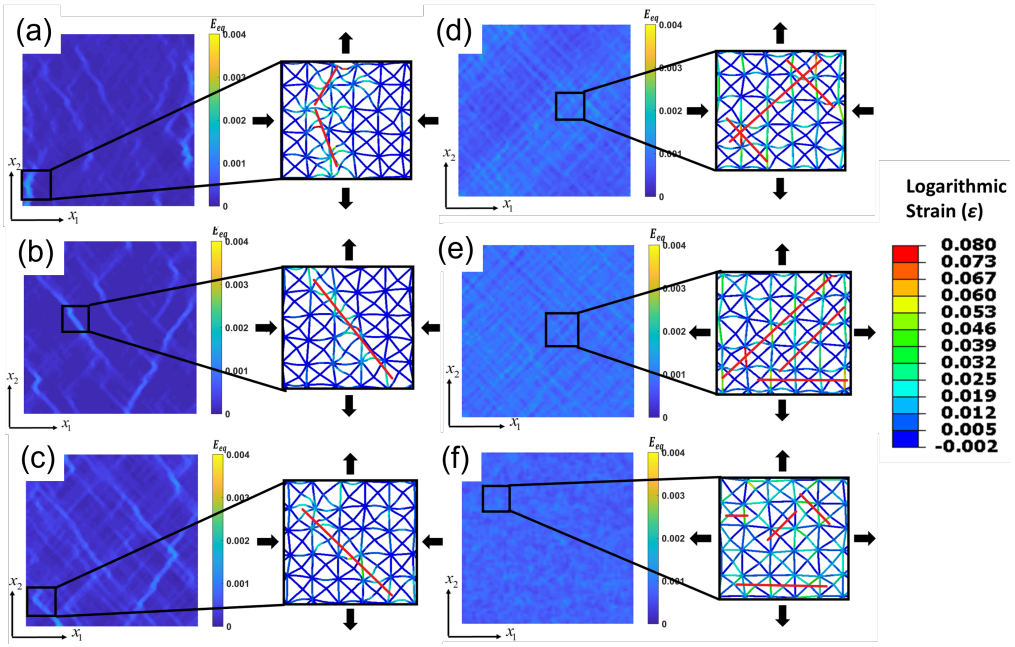

Figure 4.14: 15% distorted lattices at the point of failure illustrating failure mechanisms on continuum and lattice level at triaxiality (a) $T = -0.2$, (b) $T = -0.1$, (c) $T = 0.0$, (d) $T = 0.2$, (e) $T = 0.4$ and (f) $T = 0.67$

It can be seen from the above that lattice imperfections affect the onset of localisation effects, leading to lattice failure. Failure, therefore, involves a number with transition points between mechanisms.

4.4.5 Effect of imperfection on onset of localisation and lattice failure

Figures 4.16 (a) and (b) show the normalised equivalent band strain E^b_{eq}/E_{eq} as a function of triaxiality T, at the instants of onset of localisation and final failure, respectively, under the triaxiality range $-0.2 \leq T \leq$

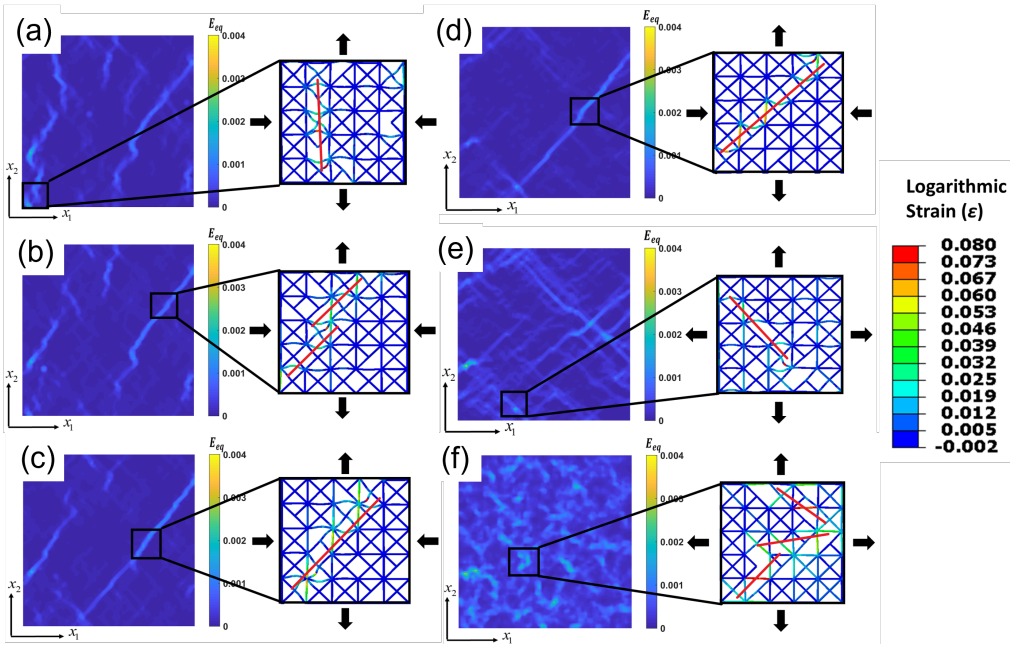

Figure 4.15: 5% missing lattices at the point of failure illustrating failure mechanisms on continuum and lattice level at triaxiality (a) $T = -0.2$, (b) $T = -0.1$, (c) $T = 0.0$, (d) $T = 0.2$, (e) $T = 0.4$ and (f) $T = 0.67$

0.67 $(\Sigma_{22} > 0)$, for perfect and imperfect lattices. There are three zones that can distinguish the failure mechanisms: Zone I ($T \leq -0.2$) represents compressive loading dominated behaviour, Zone II ($-0.2 < T < 0.2$) the shear loading dominated behaviour, and Zone III the tensile loading dominated behaviour.

In Zone I ($T \leq -0.2$), crushing band dominated failure mode occurs for all lattices. The normalised equivalent band strains are lowest compared to other failure mechanisms at onset of localisation (Figure 4.16 (a)); however, all types of lattice structures fail at much higher normalised equivalent band strain because of crushing band compared to other types of failure mechanisms (Figure 4.16 (b)).

The perfect lattice – The normalised equivalent band strain for perfect lattices is around ~ 1 at onset of localisation (Figure 4.16 (a)); and at all triaxialities, the perfect lattice shows independency for onset of localisation. In Figure 4.16 (b), the perfect lattice shows continuous decrease in band

strain. The crushing band formulation shows higher band strain at time of failure and after triaxiality $T \geq 0$, localisation does not occur resulting in a flattened curve.

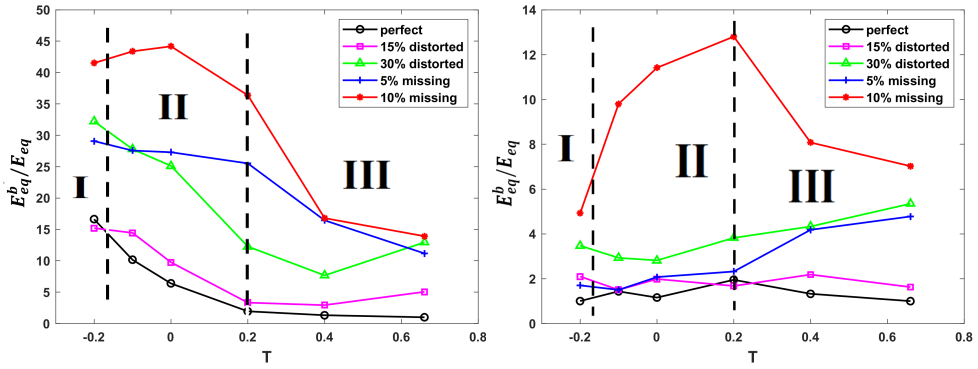

Figure 4.16: Value of normalised equivalent band strain at onset of localisation and (b) at the point of failure as a function of triaxiality

Distorted lattices– For the 15% distorted lattice, the normalised equivalent band strains are not changing substantially through all triaxialities (Figure 4.16 (a)). This indicates that the onset of localisation is nearly independent of triaxiality for the 15% distorted lattices. The 30% distorted lattice shows Mechanism 2 dominated failure for triaxiality $0 \leq T \leq 0.4$, and they are more inclined to shear band formulation compared to 15% distorted lattices. At triaxiality $T = 0.67$, multiple high equivalent strain areas form, as the same as the 15% distorted lattice but at a higher equivalent band strain due to higher degree of irregularity. Hence, from Zone II to Zone III the normalised band strain is increasing continuously (Figure 4.16 (a)). Figure 4.16 (b) shows the decreasing trend in normalised equivalent band strain at the time of failure, which indicates that crushing band shows maximum band strain followed by shear band localisation at the time of failure. Like perfect lattices, for triaxiality $T > 0$, localisation does not occur, resulting in a flattened curve for the 15% distorted lattice. The trend of 30% distorted lattice is the same as the 15% distorted lattice albeit at higher maximum normalised equivalent band strain, which implies

dependency of degree of irregularity on the final failure.

Missing lattices – From Figure 4.16 (a), the 5% missing lattice shows that, in Zone I and Zone II, the normalised equivalent band strains are not changing substantially at onset of localisation, indicating that the onset of localisation is independent of triaxiality. In Zone III the normalised equivalent band strain increases due to void coalescence dominated failure (Mechanisms 5). For the 10% missing lattice, from Zone I to Zone II, the band strains at onset of localisation increase owing to the change from failure Mechanism 1 to Mechanism 4. The slight decrease in normalised equivalent band strain at triaxiality $T = 0.67$ (biaxial tension) represent the absence of shear band and failure dictated by cluster coalescence only (Mechanism 5). For all triaxialities, for the 10% missing lattices, the strain localisation occurs at higher normalised equivalent band strain compared to the 5% missing lattices. Thus, the number of missing struts is crucial for the strain localisation. In Figure 4.16 (b), the 10% missing lattice shows that the maximum normalised equivalent band strain is higher than 5% missing lattice at the time of final failure. It shows that the 10% missing lattices are more prone to crushing band (Mechanism 1) and shear band (Mechanism 4) formulation compared to 5% missing lattices before final failure occurs. In Zone III, the changes in number of missing struts show no significant difference, which signifies that failure Mechanism 4 and Mechanism 5 are nearly independent of number of missing struts in this range.

4.4.6 Effects of size parameter on mechanical response and onset of localisation

To explore the significance of dimensional inaccuracy of FCC truss imperfect lattices on mechanical response and localisation, I have studied two variants of diameter of struts $0.5d$ and $1.5d$. For brevity, the responses of

the imperfect lattices with the 15% distorted struts and 5% missing struts subjected to different triaxiality at constant relative density are shown in Figure 4.17. In Figures 4.17 (a) and (c), the normalised effective stress response, Σ_{eq}/σ_y, is plotted against effective remote strain, E_{eq}, for the 15% distorted and 5% missing lattices, respectively. The response graph shows that, irrespective of the size of struts, the maximum load bearing capacity of the imperfect lattices does not show significant difference at equal relative densities. Figure 4.17 (b) shows the strain localisation with varying triaxiality for the 15% distorted lattice. The normalised equivalent band strain curves for both strut diameters follow the same path and fail at nearly the same points. At triaxiality $T = -0.2$, $0.5d$ lattice fails owing to Mechanism 1 and $1.5d$ fails owing to Mechanism 2. For rest of the triaxialities ($T > -0.2$), the failure mechanisms are again not sensitive to the size of the struts. Again, the failure mechanisms of 5% missing lattice are not much affected by the strut diameter (Figure 4.17 (d)).

4.4.7 Effect of triaxiality on band orientation

Figure 4.18 shows the variations of band orientation with triaxiality for the imperfect lattices. Figure 4.18 (a) is a typical example for the 5% missing struts lattice, showing band orientation under pure shear loading ($T = 0$), and Figure 4.18 (b) is a band orientation verses triaxiality plot for all types of defect. Band orientation can be divided into three subgroups where the imperfect lattices show a correlation between band orientation and a particular failure mechanism. The band orientation angles are greater than 60° for failure associated with crushing band or void coalescence induced failure. An orientation range 30° to 60° is associated with failure Mechanisms 2, 3 and 4. A band orientation of 0° is associated with those cases where there is no localised shear banding or cluster coalescence. The lat-

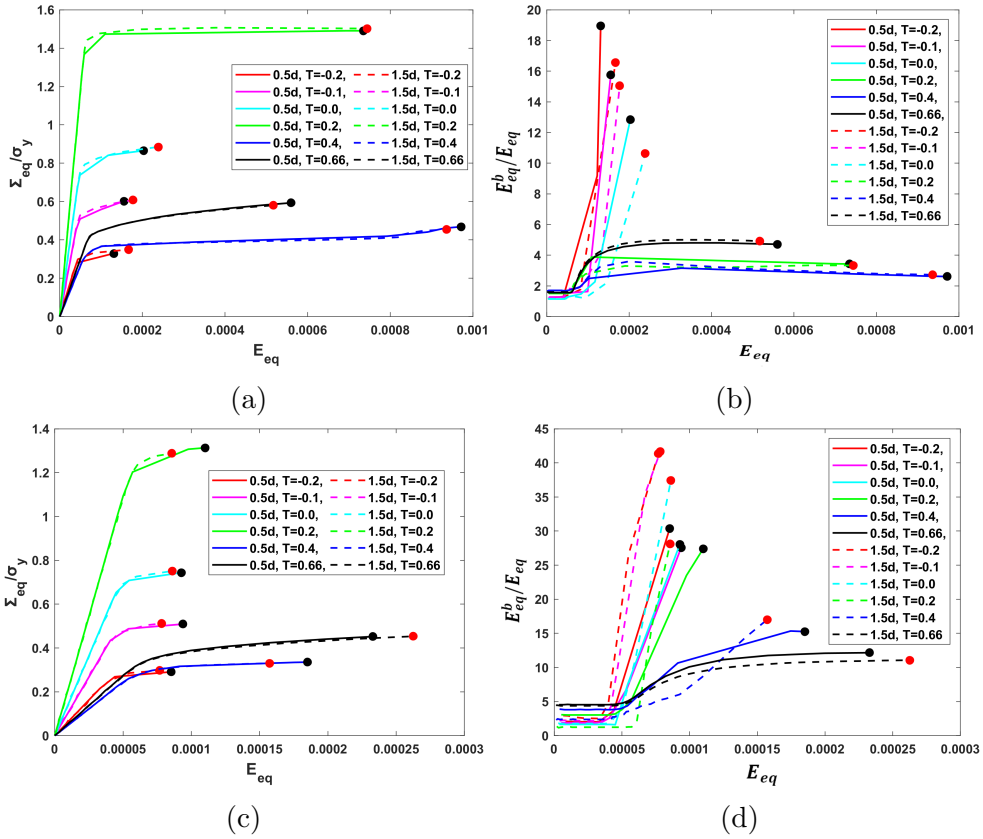

Figure 4.17: Macroscopic mechanical responses of the lattice with 15% distortion (a) and the lattice with 5% missing struts (c); and evolution of equivalent band strain for the lattice with 15% distortion (b) and the lattice with 5% missing struts (d) at $0.5d$ and $1.5d$.

tices with 15% distorted struts showed high variability and dependency on triaxiality of band orientation. The band orientation trend for the 30% distorted lattice is close to that of the 5% missing struts lattice and shows a linearly decreasing trend.

4.5 Summary

A novel numerical framework has been developed to investigate the various different failure mechanisms seen in perfect and imperfect planar FCC truss lattice metamaterials under different conditions of stress triaxiality, for the first time. It is seen that the mechanical response and mechanisms leading to failure are highly dependent on the state of stress triaxiality, the type

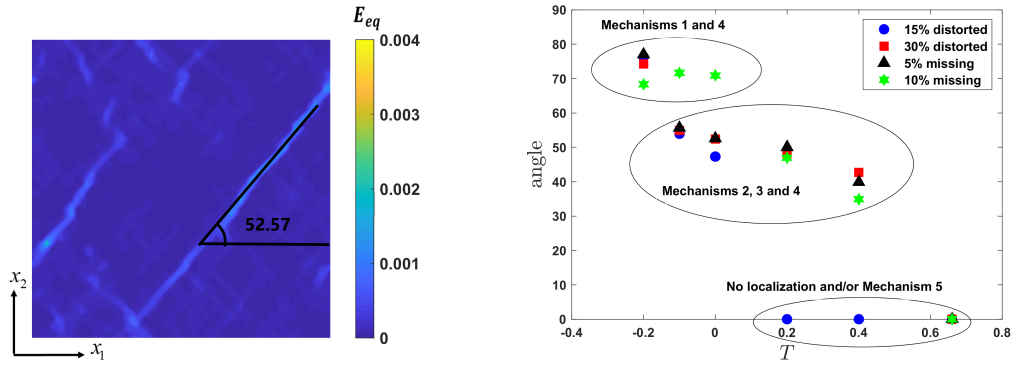

(a) (b)

Figure 4.18: (a) Shear band orientation of 5% missing struts defects at T=0 and (b) triaxiality affecting shear band orientation as per type of defects.

and quantity of defects. In order to help understand these dependencies a classification of failure mechanisms were introduced, as shown in Figure 4.3. The relationships between defect type, triaxiality and failure mechanisms are summarized below.

- For triaxiality $T \leq -0.2$, crushing band dominated failure (Mechanism 1) occurs for all lattices, while for triaxiality $-0.2 < T \leq 0$, only the perfect lattice fails due to Mechanism 1. At triaxiality $-0.2 < T \leq 0$, the 15% distorted lattices show shear band localisation (Mechanism 2), while at triaxiality $T > 0$ they do not show any localisation. However, the 30% distorted lattice is more inclined towards shear band localisation dominated failure mechanisms (Mechanism 2).

- The 5% and 10% missing strut lattices exhibit a variety of different failure mechanisms dependent on loading scenario. The 10% missing struts lattice tends to fail early owing to void coalescence (Mechanism 4) and the 5% missing struts lattice fails owing to shear band localisation (Mechanism 3). For triaxiality $T > 0.2$, Mechanism 5 and/or no localisation are observed, independent of the number of missing struts in this range.

- The severity of onset of localisation and coalescence shows dependence on lattice defect type: missing type defects are more prone to localisation compared to distorted defects. It is shown that a higher percentage distribution of irregularity gives higher normalised band strain.

- The response of the lattices is not sensitive to strut diameter variations within the range of the strut diameters.

- Failure associated with void coalescence has a wider range of band orientation than seen with the other failure mechanisms, with a band orientation in the range of 30° to 60°.

4.6 Conclusion

This chapter investigates the effect of stress triaxiality on the failure mechanisms of an-isotropic perfect and imperfect planar FCC truss lattice metamaterials. The study considers three types of imperfection in the numerical modelling, namely, distorted struts, missing struts, and strut diameter variation. This chapter proposes a novel numerical framework to overcome computational difficulties within the existing numerical approaches beyond the elastic region. The study observes three modes of microscopic localisation in perfect and imperfect lattices before failure: crushing band, shear band, and void coalescence. This concludes that the distorted lattices are prone to shear band localisation with an increase in distortion, whereas missing lattices majorly fail due to void coalescence at high missing struts defect. The strut diameter variation, within selected range shows no significant influence on the macroscopic mechanical response and strain localisation. This work may open the door for predicting failure mechanisms of imperfect lattices under a variety of loading conditions.

Note that in this study I have assumed that the failure of RVE occurs when the maximum failure strain is reached for any strut within the RVE. Further research is needed to consider the effect of the parent material damage and any defect interaction effects when multiple types and sizes of effect are present.

Chapter 5

Data-driven discovery of quasi-disordered mechanical metamaterials failed progressively

5.1 Introduction

Natural cellular materials, such as marine mussels, honeycombs, woods, trabecular bones, plant parenchyma, sponges and protoreaster nodosus, have inspired the development of mechanical metamaterials with desired or extreme mechanical properties (Figures 5.1a-d) [8, 9, 11, 153–157]. These include various truss-like micro-lattices, i.e., truss mechanical metamaterials, at a scale ranging from nanometres to millimetres, manufactured using various additive manufacturing techniques [158–160]. Truss metamaterials have provided unique opportunities to create lightweight structural components of high performance, such as lightweight sandwich structures [97, 25]. In addition, truss metamaterials are highly tailorable and can be designed to meet various multifunctional requirements, such as simultaneous load

bearing, active cooling, and noise reduction [161, 162].

Up till now, the majority of the relevant research has focused on the truss mechanical metamaterials of highly ordered structures, i.e., the bulk metamaterial is formed by repeating a RVE in the 2D or the 3D space [163, 164]. However, while nature-provided cellular materials resemble truss lattice structures of ordered, periodic arrangement, they are not perfectly periodic. Spatial disorderliness has been observed in a wide range of natural cellular materials. Egmond, et al. [12] have recently measured the disorderliness of the biological materials from trabecular bone to plant stems and fungi, using a disorder parameter $\dot{g}$ with $\dot{g} = 1$ representing the ordered system and $\dot{g} = 0.1$ the highly disordered system. They have identified the ranges of disorderliness within different types of biological materials, e.g. woods and fungi from $\dot{g} = 0.6$ to 0.8; trabecular bone and dentin from $\dot{g} = 0.55$ to 0.65; and corals and bee honeycomb from $\dot{g} = 0.9$ to 0.97 (see Figure 5.1 (e)).

The role of disorderliness in mechanical performance for natural cellular materials has not been fully understood yet. Existing research has suggested that introducing disorderliness to periodic cellular materials can cause a reduction in stiffness, strength, ductility, and fracture toughness [137, 165, 149]. However, Egmond, et al. [12] have recently found that the disorderliness at the range of $\dot{g} = 0.6$ to 0.8 within 2D Voronoi tessellation can cause an increase in toughness, through crack deflection, without loss of tensile strength in comparison with 2D regular hexagonal honeycombs. Based on this, they have hypothesized that structural disorder in natural cellular materials is a toughening mechanism and there may be a certain optimal degree of disorderliness in biogenic cellular materials in order to achieve damage tolerant behaviors. I performed 500 FE analyses on a 2D distorted lattices to observe the effects of the disordeliness on normalised strength and ductility, as shown in Figures 5.2 (a) and (b). This indi-

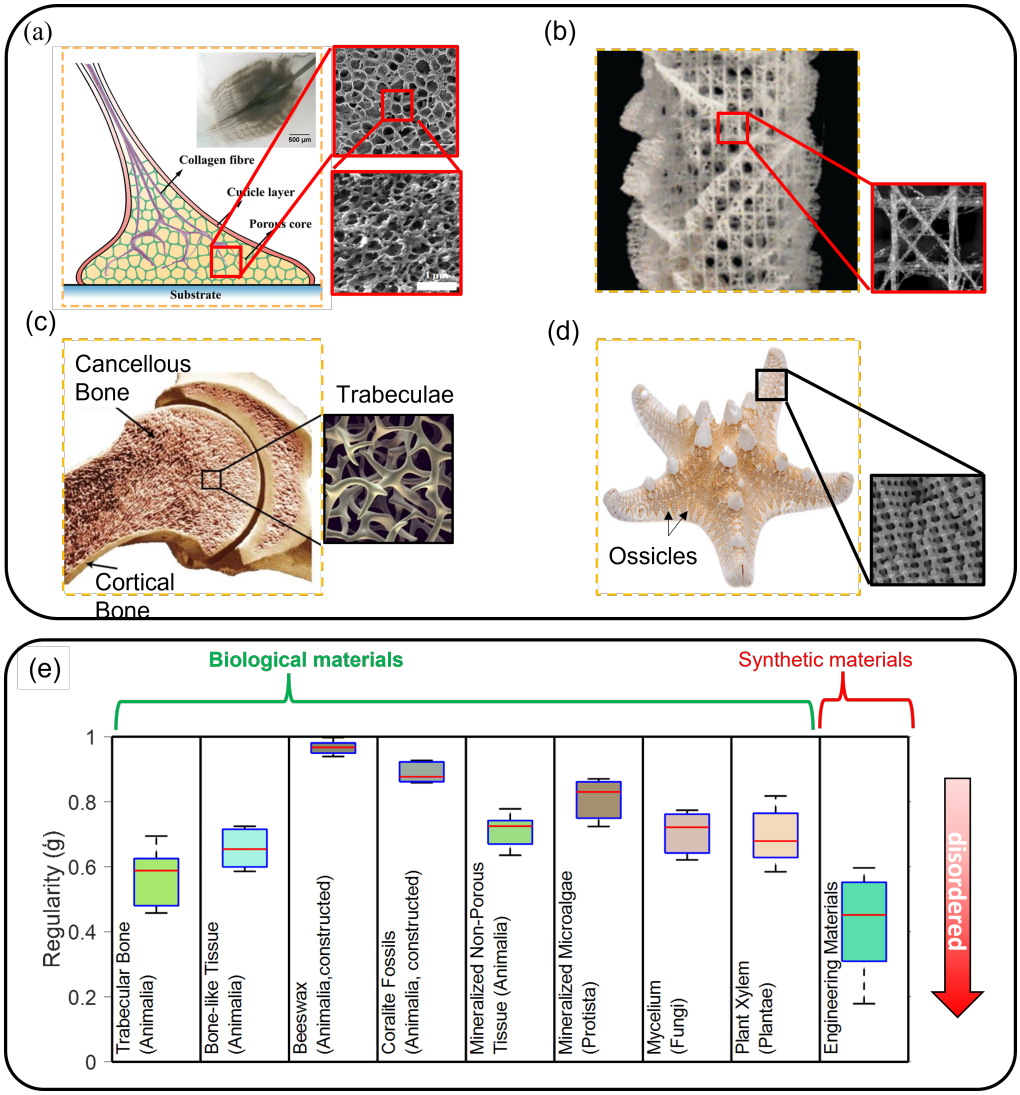

Figure 5.1: Natural cellular disordered metamaterials: (a) marine mussels on three different micro scales showing disorderliness of the struts [7], (b) deep-sea sponge, Euplectella aspergillum [8], consisting of square-grid-like architecture overlaid with a double set of diagonal bracing, (c) cortical and cancellous bone with trabeculae bone microstructure with porosity of 75% to 95% with naturally formed disorderliness [9, 10], (d) skeleton of protoreaster nodosus with its superficial soft tissue removed and SEM image of an ossicle's fracture surface affected by dislocation [11]; (e) disorderliness levels measured for all surveyed natural cellular materials (adapted from [12]).

cates that, the truss metamaterials with identical disorderliness can fail with either sudden, catastrophic brittle mode or progressive ductile mode during uniaxial tension tests, owing to the different distribution of disorderliness. Based on these preliminary analyses, *I hypothesize that not only*

the level of disorderliness but also the distribution of disorderliness within natural cellular materials may play an important role in achieving damage tolerance.

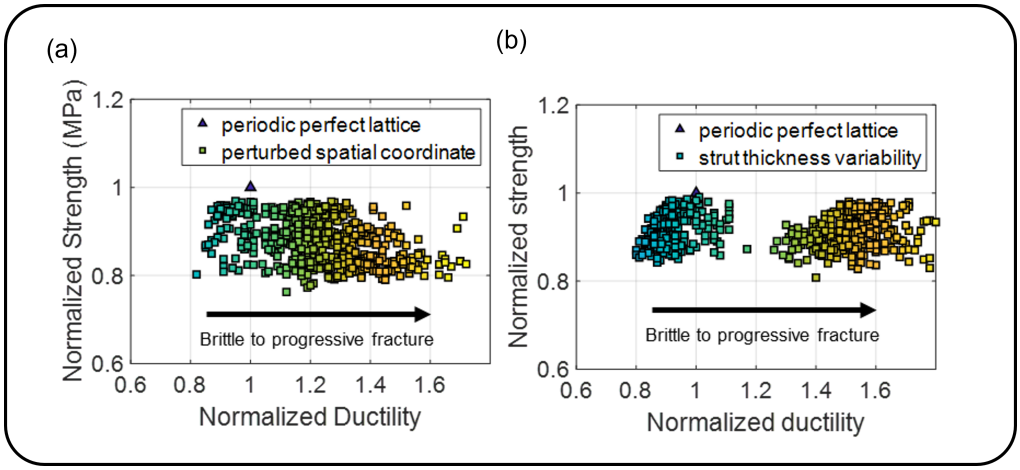

Figure 5.2: The effects of disorderliness on normalised strength and ductility: (a & b) showing a high range of ductility for spatial coordinate perturbation and strut thickness variation, respectively.

Structural materials of high performance are expected to have suitable ductility to (i) fail in a progressive manner that can give prior warning to failure events and (ii) have good load bearing capacity with the presence of flaws. It has been reported that highly ordered, periodic truss metamaterials often exhibit a sudden, catastrophic failure mode - when loaded beyond the yield point, localised bands of high strain emerge, causing catastrophic collapse [118, 13, 14]. To date, there are very limited studies on the design methodology to achieve damage tolerance for mechanical metamaterials. Owing to the highly nonlinear nature of the problems, the conventional FE based design optimisation methods are not efficient or even impractical for this purpose. Hence, mechanism-based design approaches have been attempted. Pham et al. [166, 167] have used the hardening mechanisms found in crystalline materials to develop damage-tolerant designs, primarily under compression. They have found that the disorderliness introduced to periodic truss metamaterials, by mimicking the microscale structure of

crystalline materials such as grain boundaries, precipitates, and phases, can lead to the designs of progressive failure mode.

Motivated by the hypotheses on the role of disorderliness in natural cellular materials, I here present a discovery framework for damage tolerant lattices via tuning the distribution of disorderliness to achieve damage tolerance. Our approach has focused on QTMs, which were formed by introducing small disorderliness to (parent) periodic truss metamaterials. As reported by Wang and Sigmund [39], QTMs can be tailored to achieve the extreme maximum isotropic elastic property.

Our approach to seek the optimal QTMs follows 3-steps in the data-driven framework: 1) FE simulations to create a database of structural responses (outputs) corresponding to the database of geometric inputs; 2) The deep-learning ANN approach to establish the functional relationship that links inputs to outputs, and 3) non-gradient optimisation to determine the optimal QTMs. Built upon the physical model and a custom-built loss function, numerical studies have suggested that our data-driven approach may only require relatively small datasets.

The chapter is organized as follow. The methodology of the data-driven framework the optimal QTMs are presented in Section 5.2. The results of the QTMs created from a periodic FCC lattice have demonstrated and discussed in detail in Section 5.3, along with the failure mechanisms of the brittle and optimal QTM designs. The experimentation validation of the optimal QTMs are presented in the Section 5.4. Section 5.5 contains concluding remarks and suggestions for further research.

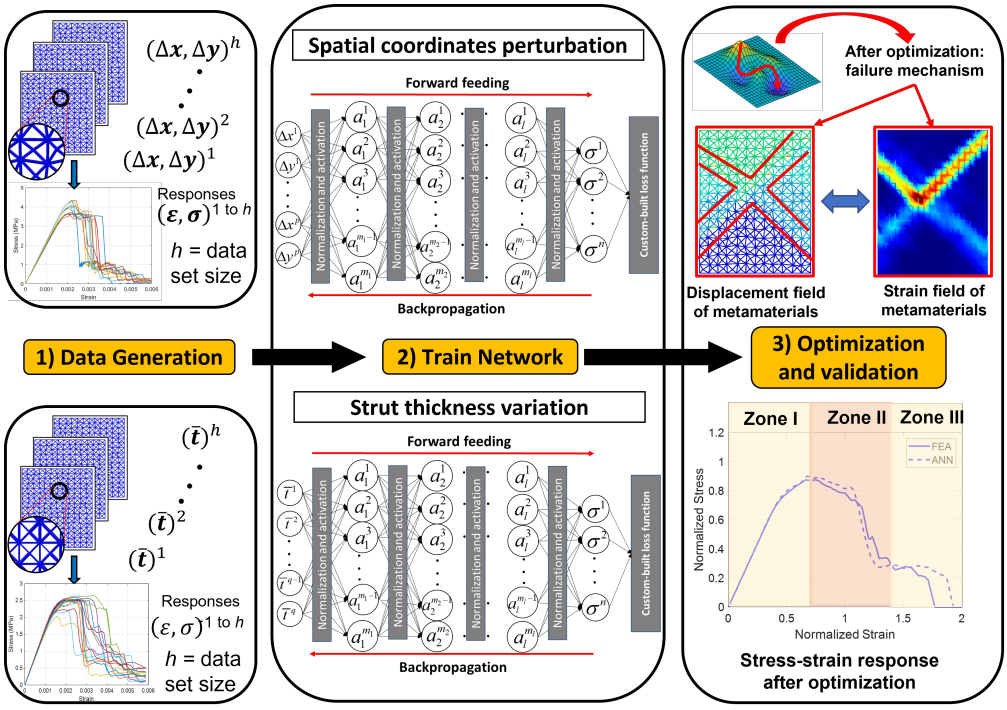

Figure 5.3: Overview of the methodology showing steps involved in designing QTMs, starting from step 1) data generation of spatial coordinate perturbation and strut thickness variation, step 2) ANN training with customised loss function to accurately map complex input and output variable, and step 3) optimisation and validation of the designs.

5.2 Methodology

5.2.1 Creating the design space for quasi-disordered lattices

Our approach to create QTMs of desired progressive failure modes was to introduce controlled (optimised) disorderliness to perfect periodic lattices of high performance. The periodic lattices with mechanical behaviour close to the H-S theoretical limit [163, 168, 169], such as FCC, triangular, and Kagome lattices [149], were chosen to act as the parent periodic lattices. Built upon data-driven approaches, the distribution and level of the disorderliness were tuned through optimisation procedures to ensure that the desired progressive failure modes could be achieved with maintaining or without much loss of the good mechanical properties inherited from the

parent periodic lattices. The geometries of the QTMs in the design space were numerically created through two distinct approaches, i.e., (1) random perturbation of the spatial coordinates of the nodes of a parent periodic lattice; and (2) random strut thickness variation of a parent periodic structure. Consider a two- dimensional (2D) parent periodic lattice with (x^i, y^i) representing the spatial coordinates of the ith node and t^j the thickness of jth strut. To create a QTM through random perturbation of the spatial coordinates of the nodes, the perturbation $(\Delta x^i, \Delta y^i)$ was defined as:

$$\begin{aligned} \Delta x^i &= \bar{x}^i - x^i = \beta\alpha r \\ \Delta y^i &= \bar{y}^i - y^i = \beta\alpha r \end{aligned} \tag{5.1}$$

Alternatively, to create a QTM through random strut thickness variation, the thickness of jth strut was defined as:

$$\bar{t}^j = (1 + \gamma\beta)t^j \tag{5.2}$$

In Eqs. 5.1 and 5.2, β $(-1 \leq \beta \leq +1)$ denotes a random variable following a uniform distribution probability distribution; r is the minimum distance between two nodes within the parent periodic lattice; α and γ are the degrees of irregularity for the spatial perturbation and strut thickness variation, respectively. In this chapter, small values are chosen for $\alpha = 0.2$ and $\gamma = 0.1$, which leads to QTMs. The method introduced in the chapter can be extended to triangular/kagome parent geometries, as shown in Figure 5.4).

5.2.2 Finite element modelling and damage model

Here, I present the details for FE modelling on the FCC lattices made of aluminium alloy Al-1050A. The lattice struts were represented as a 2-node Timoshenko-beam element (B21 in ABAQUS notation) with rigid

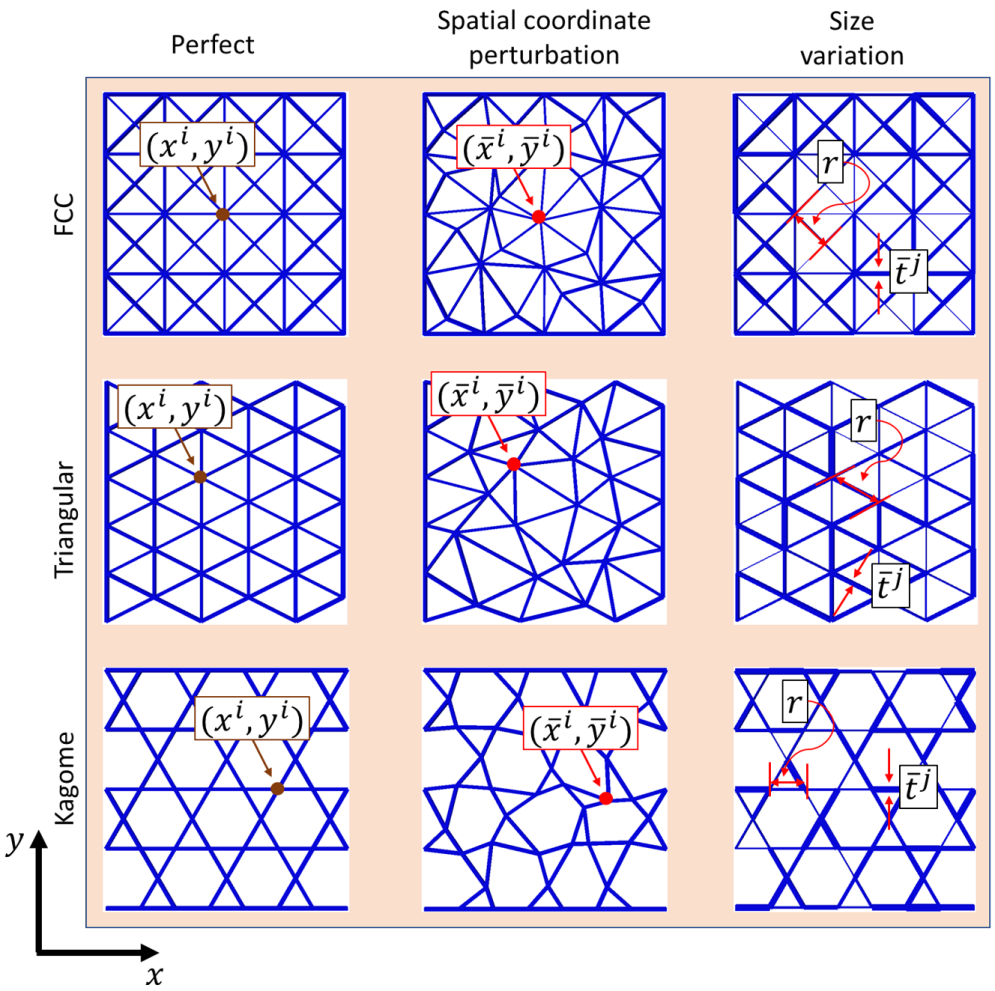

Figure 5.4: The QTM design space for two-dimensional topologies

connections. Each strut was modelled numerically as a uniform rectangular cross-sectioned solid bar of in-plane thickness, t, and unit out-of-plane width. For the parent periodic FCC lattice with identical lengths of the unit cell in the x and y directions, i.e., $u = v$, the relative density $\bar{\rho}$ of the perfect FCC lattice can be calculated as:

$$\bar{\rho} = 2\left(1 + \sqrt{2}\right)\left(\frac{t}{v}\right) \tag{5.3}$$

The relative density value was kept at $\bar{\rho} = 0.2$ for all QTM topologies in our investigation. Simulation results suggested that converged results could be achieved with each strut meshed with ten beam elements of equal length. To simulate the uniaxial tensile experiment, the specimen was subject to a

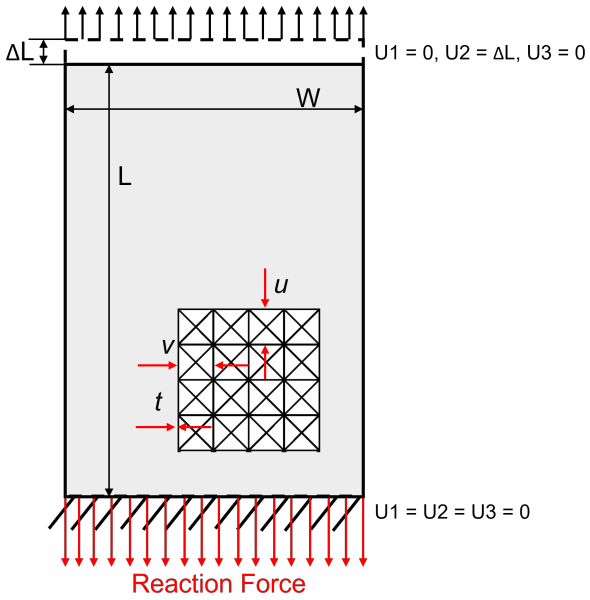

Figure 5.5: The FE model of a typical metamaterial specimen

constant vertical displacement boundary condition on the top and a fixed boundary condition on the bottom, see Figure 5.5. The macroscopic stress Σ, and macroscopic tensile strain E were calculated as:

$$\begin{aligned} \Sigma &= \frac{\text{Reaction Force}}{W}, \\ \text{E} &= \frac{\Delta L}{L} \end{aligned} \tag{5.4}$$

where W and L are the width and height of the QTMs, respectively; ΔL is the elongation in the y-direction.

The Ramberg-Osgood model was used to represent the true stress-strain relationship of the parent material, i.e., Aluminium alloy Al-1050A, given by:

$$\bar{\varepsilon} = \frac{\bar{\sigma}}{\bar{E}} + \kappa \left(\frac{\bar{\sigma}}{\bar{\sigma}_y} \right)^n \tag{5.5}$$

where $\bar{E} = 70\text{GPa}$ and $\bar{\sigma_y} = 134\text{MPa}$ are Young's modulus and yield stress of the Aluminium alloy, respectively; κ is the yield offset and n is the hardening exponent [13].

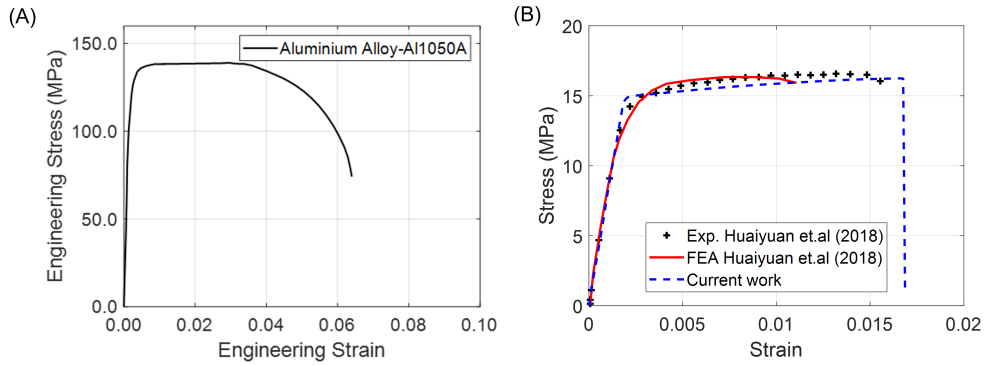

Figure 5.6: (a) Engineering stress-strain curve of the aluminum alloy (Al1050A [13]) used for FE simulations (b) Numerical validation against the experimental data based on a 2D triangular lattice reported by Huaiyuan et al. [13]

Failure initiation starts when the maximum axial strain reaches 0.03 in the element based on the tensile test result shown in Figure 5.6 [13]. The strut necking behaviour is replicated by the reduction of the yield stress after failure initiates, which is characterised by the damage variable D:

$$\bar{\sigma} = (1 - D)\,\bar{\sigma_y} \tag{5.6}$$

where D varies from 0 to 1, and is a function of the plastic strain, fitted to match the data of Figure 5.6 (a). The corresponding element is deleted from the mesh, when all the material points within the element failed ($D = 1$). Numerical validation was conducted against the experimental data based on a 2D triangular lattice reported by Huaiyuan et al. Figure 5.6 (b) [13], which suggested that FE simulation could achieve high fidelity.

5.2.3 A deep learning framework to map design space to output space

The input and output databases were generated to feed into deep learning neural network for training purposes. The input database included the geometric information of the QTM samples. Let h denote the number

of QTM samples included in the input database, and each QTM has p nodes and q struts. As shown in Figure 5.3, for the mth QTM sample, $m = 1, 2, \ldots, h$, the geometric information included in the input database consisted of (1) the perturbation of the spatial coordinates of the nodes, $(\Delta \boldsymbol{x}^m, \Delta \boldsymbol{y}^m)$, or (2) strut thickness variation, $\bar{\boldsymbol{t}}^m$, with

$$\Delta \boldsymbol{x}^m = \left[\Delta x^1, ..., \Delta x^p\right]^{m\ \mathrm{T}}, \ \Delta \boldsymbol{y}^m = \left[\Delta y^1, ..., \Delta y^p\right]^{m\ \mathrm{T}} \tag{5.7}$$

and

$$\bar{\boldsymbol{t}}^m = \left[\bar{t}^1, ..., \bar{t}^q\right]^{m\ \mathrm{T}} \tag{5.8}$$

The output database includes the information on the structural responses of the QTM samples obtained by FE simulations. As the current research focuses on the structural response under uniaxial tension, the normalised macroscopic stress data $\boldsymbol{\sigma}^m = [\sigma^1, \sigma^2, ..., \sigma^n]^{m\ \mathrm{T}}$ collected at a sequence of n predefined, equally spaced normalised macroscopic uniaxial strains, $\boldsymbol{\varepsilon}^m = [\varepsilon^1, \varepsilon^2, ..., \varepsilon^n]^{m\ \mathrm{T}}$, were stored in the output database for the mth QTM sample. Here, the macroscopic stresses are defined as the stresses averaged over the entire model, and the macroscopic tensile strain is defined as the elongation over the original length of the model.

A feed-forward deep-learning ANN was trained, using the input and output databases, to map the functional relationship between the input and output databases, as shown in Figure 5.3, i.e.,

$$\begin{aligned} \boldsymbol{\sigma} &= \left[\sigma^1, \sigma^2, ..., \sigma^n\right]^{\mathrm{T}} = f_1(\Delta \boldsymbol{x}, \Delta \boldsymbol{y}), \quad \text{or} \\ \boldsymbol{\sigma} &= \left[\sigma^1, \sigma^2, ..., \sigma^n\right]^{\mathrm{T}} = f_2(\bar{\boldsymbol{t}}) \end{aligned} \tag{5.9}$$

Neural network architecture refers to assembling neurons into layers: Each neuron uses a mathematical transformation of weights and biases to generate an output layer. For example, the mathematical form of a feed-forward propagation neural network of l layers can be written as:

$$
\begin{aligned}
&\boldsymbol{a}_1 = g\left(\boldsymbol{\theta}^{[1]}\boldsymbol{\psi} + \boldsymbol{b}_1\right)\\
&\boldsymbol{a}_2 = g\left(\boldsymbol{\theta}^{[2]}\boldsymbol{a}_1 + \boldsymbol{b}_2\right)\\
&\ldots\\
&\boldsymbol{a}_{ii} = g\left(\boldsymbol{\theta}^{[ii]}\boldsymbol{a}_{ii-1} + \boldsymbol{b}_{ii}\right)\\
&\ldots\\
&\boldsymbol{a}_{l-1} = g\left(\boldsymbol{\theta}^{[l-1]}\boldsymbol{a}_{l-2} + \boldsymbol{b}_{l-1}\right)\\
&\boldsymbol{\sigma} = \boldsymbol{\theta}^{[l]}\boldsymbol{a}_{l-1} + \boldsymbol{b}_l
\end{aligned}
\tag{5.10}
$$

where $\boldsymbol{\theta}^{[ii]}$ is a weight matrix in the iith layer, $ii = 1, 2, ..., l$; $\boldsymbol{b}_{[ii]}$ the bias vector in the iith layer; $\boldsymbol{a}_{[ii]}$ the output vector in the iith layer; g the activation function; $\boldsymbol{\psi}$ is the input vector of the ANN, i.e.,

$$
\begin{aligned}
&\boldsymbol{\psi} = \left[\left(\Delta x^1, \Delta y^1\right), ..., \left(\Delta x^p, \Delta y^p\right)\right]^{\mathrm{T}}, \quad \text{or}\\
&\boldsymbol{\psi} = \bar{\boldsymbol{t}} = \left[\bar{t}^1, ..., \bar{t}^q\right]
\end{aligned}
\tag{5.11}
$$

The learning (training) procedure tunes the ANN components to minimise the cost function $J(\boldsymbol{\theta}^{[ii]}, \boldsymbol{b}_{ii})$, which is related to the loss function $\mathcal{L}(\boldsymbol{\sigma}^m_{pred}, \boldsymbol{\sigma}^m_{true})$, by the following Equation [170]:

$$
J(\boldsymbol{\theta}^{[ii]}, \boldsymbol{b}_{ii}) = \frac{1}{h}\sum_{m=1}^{h}\mathcal{L}(\boldsymbol{\sigma}^m_{pred}, \boldsymbol{\sigma}^m_{true}) \tag{5.12}
$$

where the loss function measures the accuracy of the trained ANN by evaluating the difference between the predicted stresses, $\boldsymbol{\sigma}^m_{pred} = [\sigma^1, \sigma^2, ..., \sigma^n]^{m\ \mathrm{T}}_{pred}$ and the real stresses, $\boldsymbol{\sigma}^m_{true} = [\sigma^1, \sigma^2, ..., \sigma^n]^{m\ \mathrm{T}}_{true}$.

To improve the learning efficiency of the ANN model, the normalised macroscopic stress data $\boldsymbol{\sigma}^m = [\sigma^1, \sigma^2, ..., \sigma^n]^{m\ \mathrm{T}}$ for a QTM sample can be divided into three groups, which correspond to the three zones in the stress-strain relation for the QTM sample under uniaxial tension, respectively, as shown in Figure 5.3. It is noted that the structure experiences (1)

elastic deformation in Zone I, (2) plastic deformation caused by the failure of a limited number of struts in Zone II, and (3) final catastrophic failure in Zone III. Numerical experiments on quasi-disordered FCC lattices have suggested that the stress data in the three groups (Zones) have significantly different variances across the QTM samples (see APPENDIX B.1.2 Figure B.2). Based on this finding, a novel quantile regression loss function has been employed in this work, which is given as:

$$\mathcal{L}_{custom}(\boldsymbol{\sigma}^k_{pred}, \boldsymbol{\sigma}^k_{true}) = \frac{1}{3n}\sum_{i=1}^{3}\left[\sum_{\substack{k=1 \\ \sigma^k_{true}<\sigma^k_{pred}}}^{n}(\lambda_i - 1)\left(\sigma^k_{pred} - \sigma^k_{true}\right)^2 + \sum_{\substack{\mathrm{k=1} \\ \sigma^k_{true}\geq\sigma^k_{pred}}}^{n}\lambda_i\left(\sigma^k_{pred} - \sigma^k_{true}\right)^2\right] \tag{5.13}$$

where λ_i, $i = 1, ..., 3$, are the chosen quantiles for the three groups of the stress data and have values between 0 and 1. The quantile loss function is an extension of the Mean Square Error (MSE) that has the quantile $\lambda_i = 0.5$. The larger the value λ_i, the more under-predictions are penalized than over-predictions. Our numerical experiments have suggested that it can help to improve deep-learning efficiency (see APPENDIX B.1.5) and reduce the amount of data required for the deep-learning process by using distinct λ_i values at different Zones.

5.2.4 Non-gradient-based design optimisation

Design optimisation procedures can be employed to tune the distribution of disorderliness within the parent periodic lattices to achieve desired progressive failure modes. The mathematical model for design optimisation can be described as follows:

Objective function (maximize):

$$T(\Delta \boldsymbol{x}, \Delta \boldsymbol{y}) \text{ Or } T(\bar{\boldsymbol{t}}) \tag{5.14}$$

Constraints:

$$\begin{aligned}
&\Delta x_{\min} \leq \Delta x^i \leq \Delta x_{\max};\\
&\Delta y_{\min} \leq \Delta y^i \leq \Delta y_{\max}, \quad i \in [1, p]\\
&\text{or}\\
&t_{\min} \leq \bar{t}^j \leq t_{\max}, \quad j \in [1, q]\\
&\text{and}\\
&\langle \sigma_{ut} \rangle \geq \sigma_{\min}\\
&\langle E_0 \rangle \geq E_{0\,\min}
\end{aligned} \tag{5.15}$$

where $\langle \sigma_{ut} \rangle$ and $\langle E_0 \rangle$ denote the maximum normalised macroscopic tensile stress and the macroscopic Young's modulus of the lattice obtained by the uniaxial tensile tests, respectively; $\Delta x_{\min}$, $\Delta y_{\min}$, $t_{\min}$, $\sigma_{\min}$ and $E_{0\,\min}$ are the lower bounds of design variables; and $\Delta x_{\max}$, $\Delta y_{\max}$ and $t_{\max}$ the upper bounds. In Eq. 5.14, the objective function T is a measurement related to the deformation capacity of the QTMs, such as ductility and strain energy density obtained under uniaxial tensile load. Here and throughout the rest of the chapter, the ductility is defined as the macroscopic tensile strain at failure, which corresponds to the post-peak macroscopic stress equivalent to 25% of the peak macroscopic tensile stress; and the strain energy density was calculated as the area under the macroscopic stress-strain curve.

5.3 Results and Discussions

I demonstrate the success of the proposed method through the discovery of the high-performance 2D QTMs of the progressive failure modes. The

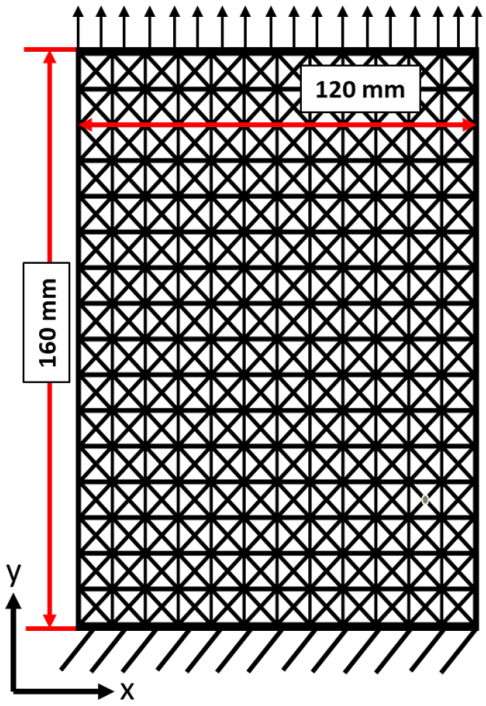

Figure 5.7: The dimensions and boundary conditions of the FE model

QTMs were created based on a parent periodic FCC lattice (see Section 5.2.1). It was assumed that the lattice was made of the aluminium alloy Al-1050A, and with relative density, $\bar{\rho} = 0.2$. This relative density value was chosen for our investigation while taking the manufacturability of the minimum strut thickness into consideration [13]. The parent periodic FCC lattice consisted of 12- and 16-unit cells periodically arranged along the x and y directions, respectively, with dimensions of 120 mm in x direction and 160 mm in y directions, see Figure 5.7. This geometry was chosen to ensure that the mechanical properties, i.e., macroscopic stiffness and peak strength were not sensitive to the size of the test samples. The size effects were evaluated by increasing the number of unit cells from 2 to 18 in x direction. I have conducted FE simulations for 100 QTMs at relative densities of $\bar{\rho} = 0.2$ with nodal perturbation irregularity $\alpha = 0.2$ for each sample size. Fig. 5.8 (a) shows the size effect via the functional relationship of the structural macroscopic stiffness against the number of unit cells in x

direction. The macroscopic stiffness is not sensitive to the number of unit cells when number of cells were more than 12. As shown in Fig. 5.8 (b), the peak strength converged at the lattice size of 12 unit cells in x-direction (i.e., 16 unit cells in y direction). Thus, I opted for the QTMs of 12×16 unit cells for this methodology development.

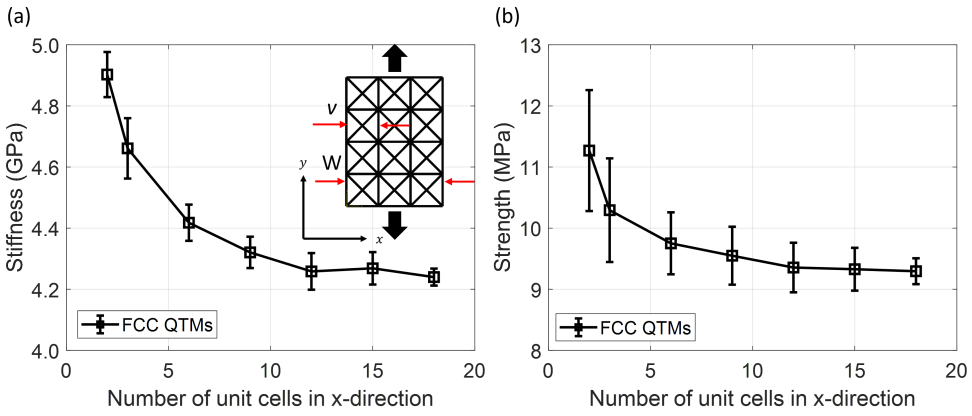

Figure 5.8: The size effects on (a) the structural macroscopic stiffness and (b) the structural peak strength of the FCC QTMs generated via spatial coordinate perturbations.

The FE simulations have suggested that the parent lattice exhibits a sudden, catastrophic structural failure mode under uniaxial tension along the direction, as shown in Figure 5.9 for the corresponding normalised macroscopic stress-strain relation. As shown in the insert of Figure 5.9 for the distribution of the displacement at failure, the failure event was mainly caused by the formulation of a single shear band across the sample. For the macroscopic stress-strain relation shown in Figure 5.9 and the rest of the chapter, the stress values have been normalised by the peak stress, and the strain values by the maximum strain of the parent FCC periodic lattice.

5.3.1 The ANN models

The first ANN model was created based on the scenario in which disorderliness was introduced into the FCC periodic lattice via the perturbation of the spatial coordinates of the nodes. The geometries of 5000

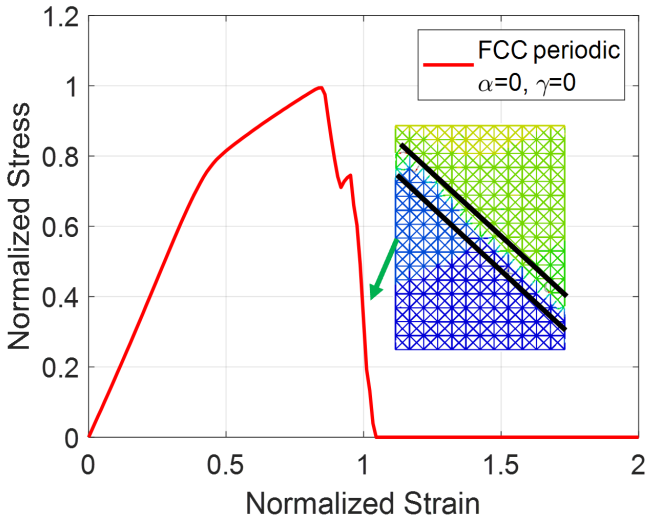

Figure 5.9: The normalised macroscopic stress-strain relation of a parent periodic FCC lattice.

QTM samples were generated with irregularity, $\alpha = 0.2$, at constant relative density, $\bar{\rho} = 0.2$. The input database containing perturbation of the spatial coordinates of the nodes, $\boldsymbol{\psi} = [(\Delta x^1, \Delta y^1), ..., (\Delta x^p, \Delta y^p)]^{\mathrm{T}}$, and the output database containing the normalised macroscopic stress data, $\boldsymbol{\sigma} = [\sigma^1, \sigma^2, ..., \sigma^n]^{\mathrm{T}}$, were created to train the ANN model. The ANN model consisted of 7 hidden layers with 4096, 2048, 1024, 1024, 1024, 512, and 512 neurons, respectively, in sequence from input to output layers. The numerical experiments have suggested that the structure of the ANN has achieved optimal size in deep learning, and no further improvement was observed by increasing the number of hidden layers. The tuning of ANN model hyperparameters was obtained by performing Bayesian optimisation (APPENDIX B.1.4), based on the loss function with ($\lambda_1 = 0.5, \lambda_2 = 0.45$ and $\lambda_3 = 0.1$), respectively. The second ANN model was created based on the scenario in which the disorderliness was introduced into the parent FCC periodic lattice via strut thickness variation. The ANN model was trained based on the input database containing struct thicknesses, $\boldsymbol{\psi} = \bar{\boldsymbol{t}} = [\bar{t}^1, ..., \bar{t}^q]$, and the output database resulted from the FE simulations for 5000 QTM samples, with irregularity

$\gamma = 0.1$ and at constant relative density, $\bar{\rho} = 0.2$. The ANN parameters are the same as in the previous case, except that the chosen quantiles were $\lambda_1 = 0.5, \lambda_2 = 0.5$ and $\lambda_3 = 0.3$, respectively. I trained the two ANN models for 1000 iterations with an early stopping function when no improvements were made for ten iterations consecutively.

The evaluations on the full dataset are presented in Figures 5.10 and 5.11. Figure 5.10 compares the FEA with the ANN predictions of the stress-strain curves of the FCC QTMs generated via nodal perturbations ($\alpha = 0.2$). In the Figure 5.10, the first, second, and third row plots compare training, validation, and test datasets, respectively. The stress-strain curves are randomly selected from the respective datasets. Similarly, Figure 5.11 compares the FEA with the ANN predictions for FCC QTMs generated via strut thickness variations ($\gamma = 0.1$). In both cases good agreement has been achieved.

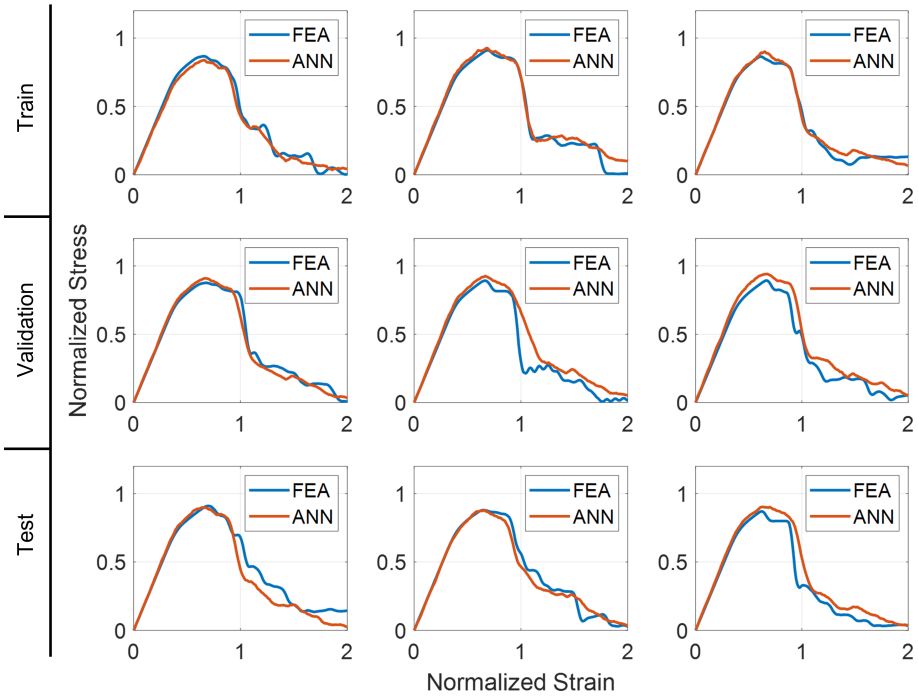

Figure 5.10: The comparison of the FEA results with the ANN predictions for FCC QTMs generated via spatial coordinate perturbations.

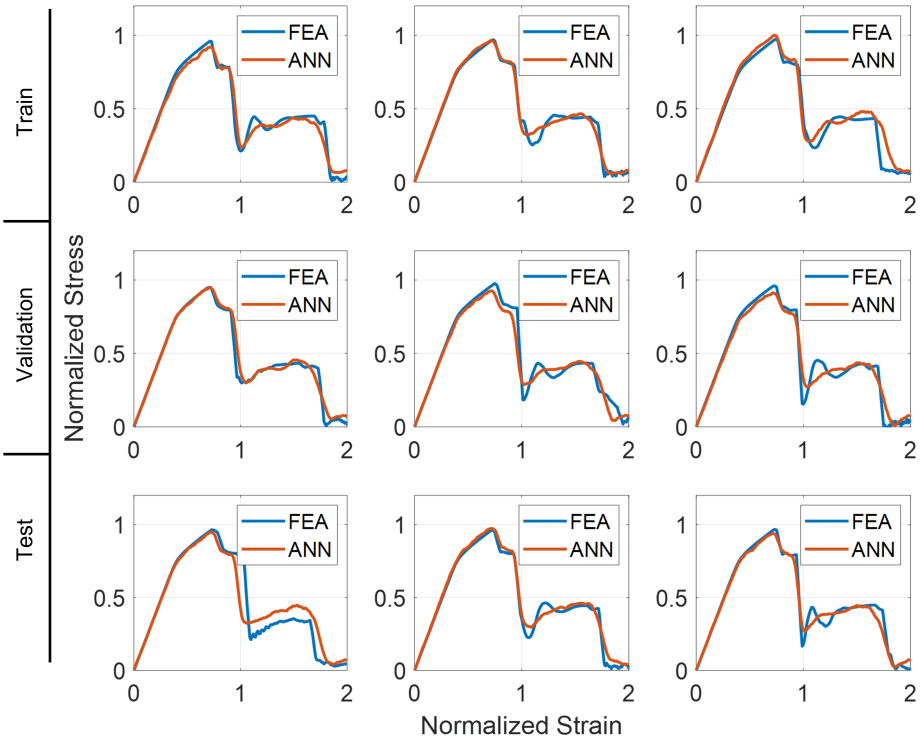

Figure 5.11: The comparison of the FEA results with the ANN predictions for FCC QTMs generated via strut thickness variations.

5.3.2 The design optimisation

The optimisation problem described in Eqs. 5.14 and 5.15 can be solved using non-gradient based optimisation algorithms, such as the Genetic Algorithms [171, 172], the Particle Swarm optimisation [173], and the Simulated Annealing (SA) optimisation [92], with the structural responses calculated by FE simulations.

The objective functions were optimised with the constraints of allowable nodal perturbation, $\alpha = 0.2$, allowable struct thickness variation $\gamma = 0.1$, minimum normalised strength, $\sigma_{\min} = 0.9$, and minimum normalised stiffness, $E_0 = 0.95$, using the SA optimisation algorithm (MATLAB [174]). However, owing to the highly nonlinear nature of the problem, I found that it was impractical to use the FE based optimisation procedures to solve the optimisation problem. A numerical experiment suggested that it took up

to 7 minutes to calculate the structural response of a single sample under a uniaxial tensile test. In this work, I used the SA optimisation algorithm to achieve the optimised designs with the upper limit of 10000 iterations. Figure 5.12 shows a typical behavior of the SA optimiser obtained by the strain energy density optimisation function. It can be seen that the optimal value has been converged at 600 iterations. As shown in Table 5.1, under the environment of the PC with Intel(R) Core(TM) i5-5200U CPU @ 2.20GHz, 4 core processors with 16GB RAM, it took approximately 0.015 minutes to complete a single calculation by a trained ANN model, compared to 7 minutes by a single FE calculation (up to 48 days for the optimisation process). Hence, ANN based optimisation process is far more efficient than the conventional FE based optimisation process.

Table 5.1: Quantitative comparison of the FEA versus the ANN based optimisation method time

number of samples	FEA based optimisation (min)	ANN based optimisation (min)
1	7	0.015
10000 (iterations)	70000 (∼48 days)	150

The strength constraint can ensure that the resulted QTMs preserve more

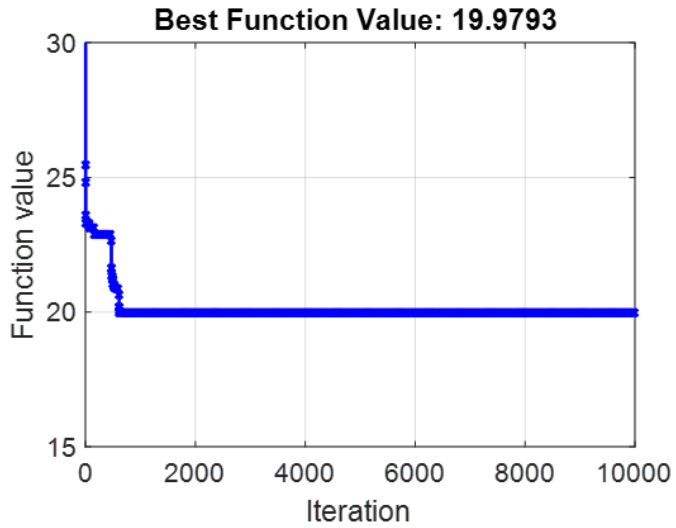

Figure 5.12: The convergence behavior of the SA optimiser

than 90% of the strength and 95% of the stiffness from the parent periodical FCC lattice. The relative density of optimised QTMs have been found to be maintained at a constant value $\bar{\rho} = 0.2$. The optimisation results are presented below for the QTMs having improved ductility owing to the progressive failure process.

5.3.3 The optimised results

Based on the first ANN model, I optimised the distribution of the perturbation of the spatial coordinates of the nodes for the maximized ductility design and the maximized strain energy density design, respectively, as shown in Figures 5.13 and 5.14 for the optimised designs. The optimised distributions of the nodal perturbation were used to create the corresponding FE models for validation and interpretation purposes. Compared to the periodic FCC lattice (Figure 5.9), which failed in a sudden, catastrophic manner, the optimised designs exhibited progressive failure modes. The optimised design based on the maximized ductility design model exhibits a 73% increase in ductility (Figure 5.13 (a)); and the optimised design based on the maximized strain energy density model exhibits a 56% increase in strain energy density (Figure 5.14 (a)), both with less than 5% reduction in stiffness and up to 15% reduction in strength. The ANN predictions have good agreement with the FE simulation results. FE simulations suggested that the progressive failure modes in the optimised designs were mainly achieved by shear band branching that causes load-path shift to undamaged struts, as shown in Figure 5.13 (d) (QTM-N1) and Figure 5.14 (d) (QTM-N4) for ductility and strain energy density objective functions, respectively. However, it has been found that the optimised designs were not unique: the solution is sensitive to the initial distribution of the perturbation. This indicates that the method can generate different designs

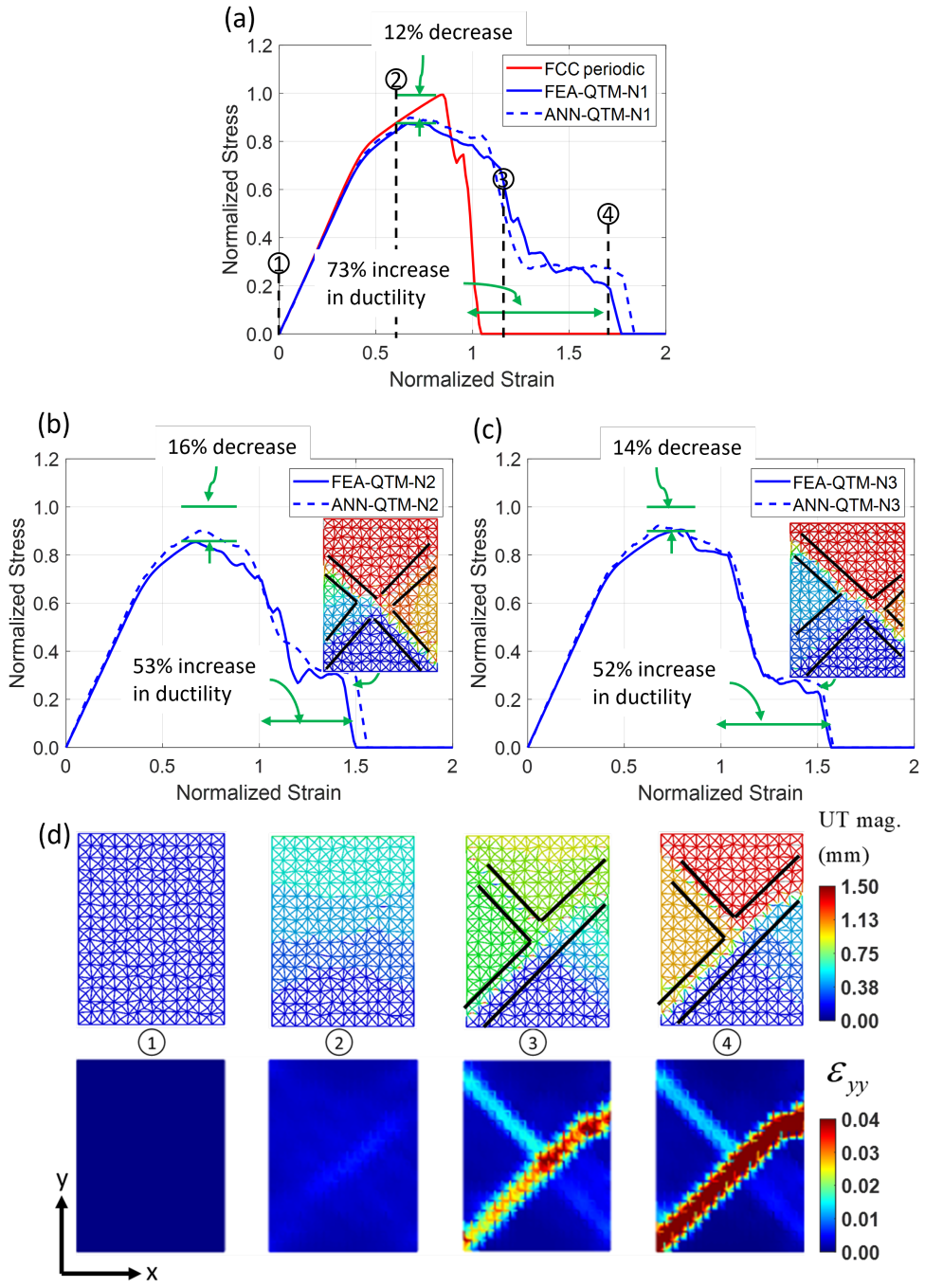

Figure 5.13: (a, b and c) the normalised stress-strain curves of three optimised QTMs (-N1, -N2 and -N3, using ductility objective function) obtained by the FE simulations and ANN predictions; (d) the detailed distributions of displacements in the lattices along with the continuum plots of microscopic strain [14] at selected macroscopic strains of a QTM (-N1), showing shear band branching.

with similar local optima. To illustrate this, based on three different initial distributions that were randomly picked from the input dataset, I obtained

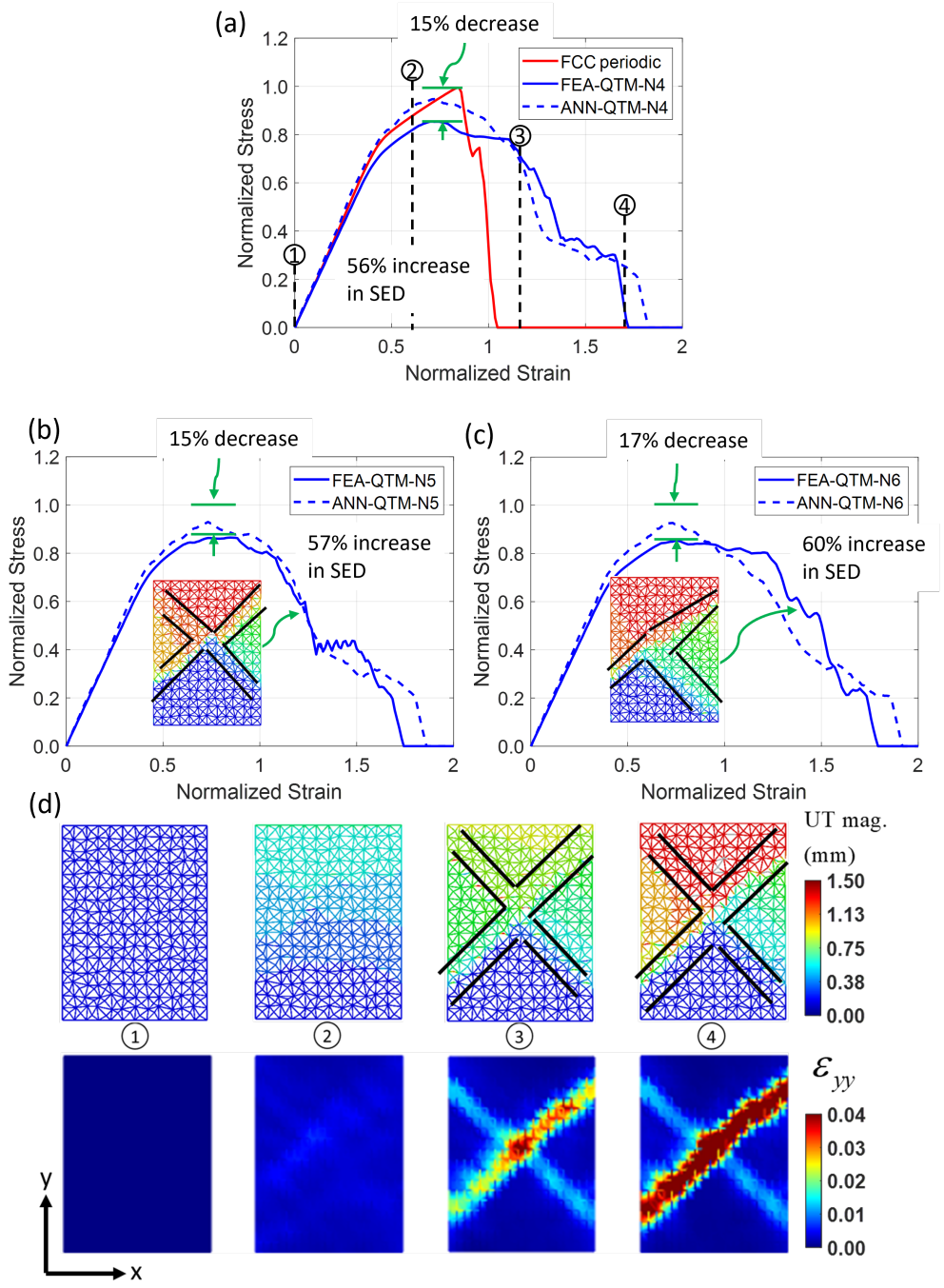

Figure 5.14: (a, b and c) the normalised stress-strain curves of three optimised QTMs (-N4, -N5 and -N6, using strain energy density objective function) obtained by the FE simulations and ANN predictions; (d) the detailed distributions of displacements in the lattices along with the continuum plots of microscopic strain [14] at selected macroscopic strains of a QTM (-N4), showing shear band branching.

the optimised distributions of the perturbation for the maximized ductility designs (Figures 5.13 (a), (b) and (c) for QTMs-N1, -N2 and -N3) and the

maximized strain energy density designs (Figures 5.14 (a), (b) and (c) for QTMs-N4, -N5 and -N6), respectively. Albeit slight differences in mechanical behaviors, these optimised designs all show progressive failure modes with a significant increase in ductility or strain energy density compared to the periodic FCC lattice. The inserted distribution of the displacement at failure, as shown in Figures 5.13 (b), (c), (d) and Figures 5.14 (b), (c), (d), have suggested that the progressive failure modes were mainly caused by shear band branching in different patterns.

In this section, I optimised the variation of strut thickness within the parent periodic FCC lattices using the ductility objective function, as shown in Figure 5.15 for the three optimised designs. As in the previous case, I obtained the optimum designs that exhibited progressive failure modes compared to the periodic FCC lattice (Figure 5.7). The optimised designs exhibit more than 80% increase in ductility with the expense of less than 5% stiffness and less than 11% strength (Figures 5.15 (a), (b) and (c)); and again the progressive failure modes in the optimised designs were mainly achieved by the shear band branching with different patterns, as shown in Figure 5.15 (b), (c) and (d) of QTMs -S1, -S2 and -S3. Similarly, I have obtained three optimised QTM designs using the strain energy density objective function, as shown in Figure 5.16. The optimised designs exhibit more than 60% increase in strain energy density with the expense of less than 5% stiffness and less than 9% strength (Figures 5.16 (a), (b) and (c)). Our results show that the QTMs resulting from the strut thickness variation are more prone to brittle failure compared to those resulting from the spatial nodal perturbation.

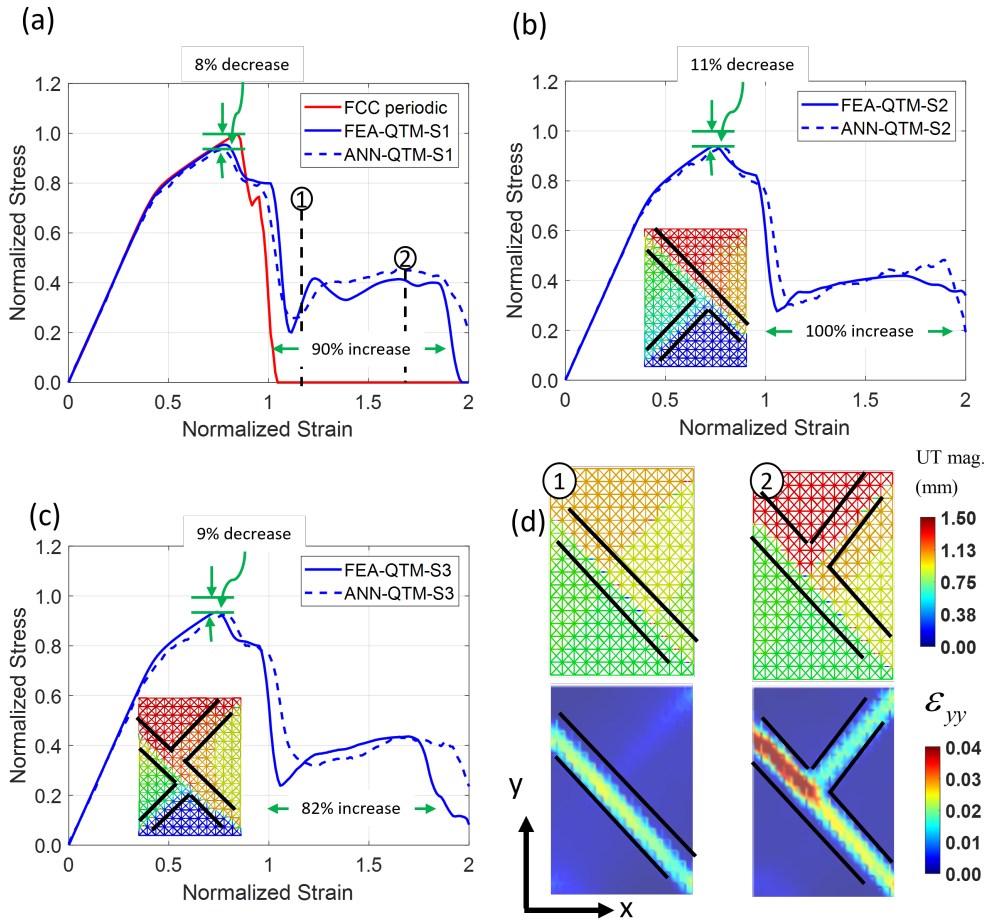

Figure 5.15: Designs of metamaterials based on strut thickness variation using ductility objective function, (a, b and c) the normalised stress-strain curves of three optimised QTMs (-S1, -S2 and -S3) obtained by the FE simulations and ANN predictions; (d) the distribution of microscopic strain at selected macroscopic strains of a QTM (-S1), showing that shear band branching causes progressive failure mode. The inserts of show the distribution of the displacement at failure, which is caused by the formulation of the shear band branching with different patterns.

5.3.4 Failure mechanism

To understand how initial disorderliness can affect shear band branching that leads to enhancement of ductility, I have studied the failure mechanisms of two QTM designs: i) an optimised QTM with improved ductility (Figure 5.17 (a)), and ii) a QTM with low ductility brittle failure mode (Figure 5.17 (b)). The failure paths have been traced for both designs, which were caused by the breaking of struts owing to damage, as shown

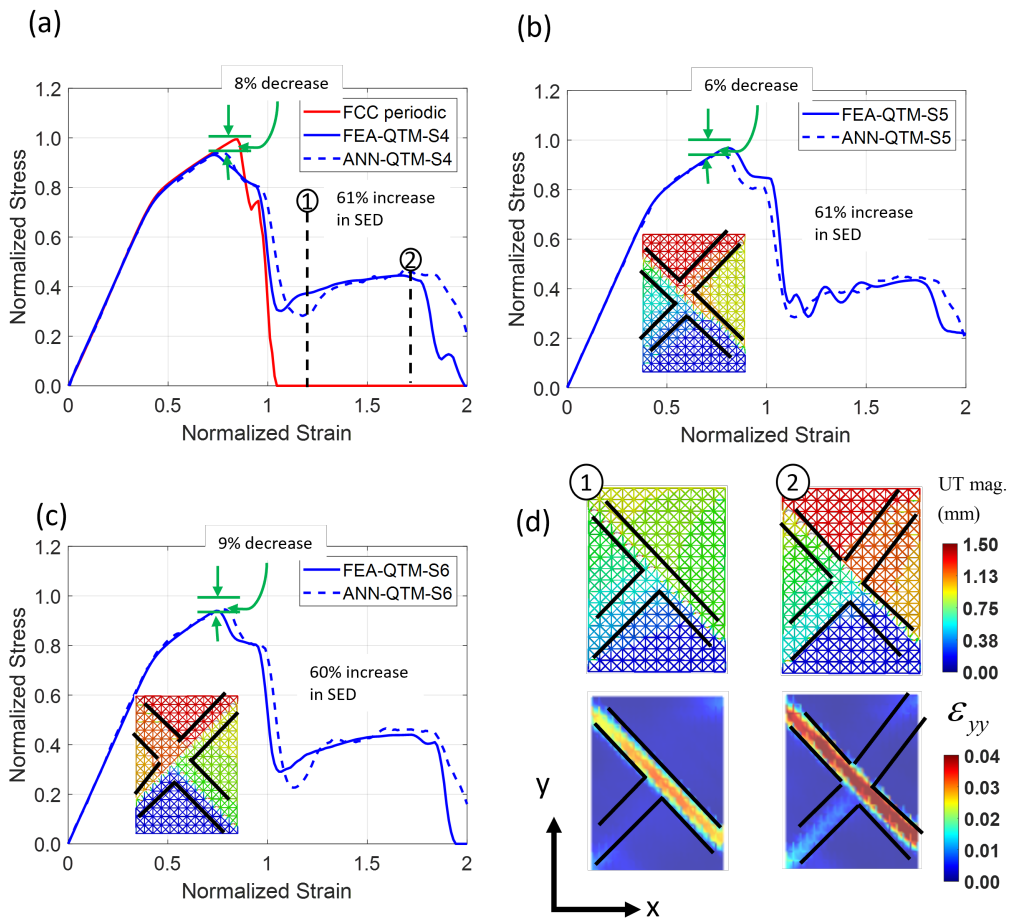

Figure 5.16: Designs of metamaterials based on strut thickness variation using strain energy density objective function, (a, b and c) the normalised stress-strain curves of three optimised QTMs (-S4, -S5 and -S6) obtained by the FE simulations and ANN predictions; (d) the distribution of microscopic strain at selected macroscopic strains of a QTM (-S4), showing that shear band branching causes progressive failure mode. The inserts show the distribution of the displacement at failure, which is caused by the formulation of the shear band branching with different patterns.

in the detailed geometries of the QTMs with contour showing the magnitude of the damage variable D. Here, the damage variable D varies from 0 to 1, with $D = 1$ representing complete failure at the integration point of the element. The resultant initial spatial coordinate perturbation, i.e., $\sqrt{(\Delta x^i)^2 + (\Delta y^i)^2}$, is employed to quantify the overall disorderliness at ith node. The continuum plots of the resultant coordinate perturbations suggest that the optimised QTM (Figure 5.17 (a)) has a higher level distribution of disorderliness than the brittle QTM (Figure 5.17 (b)). For both

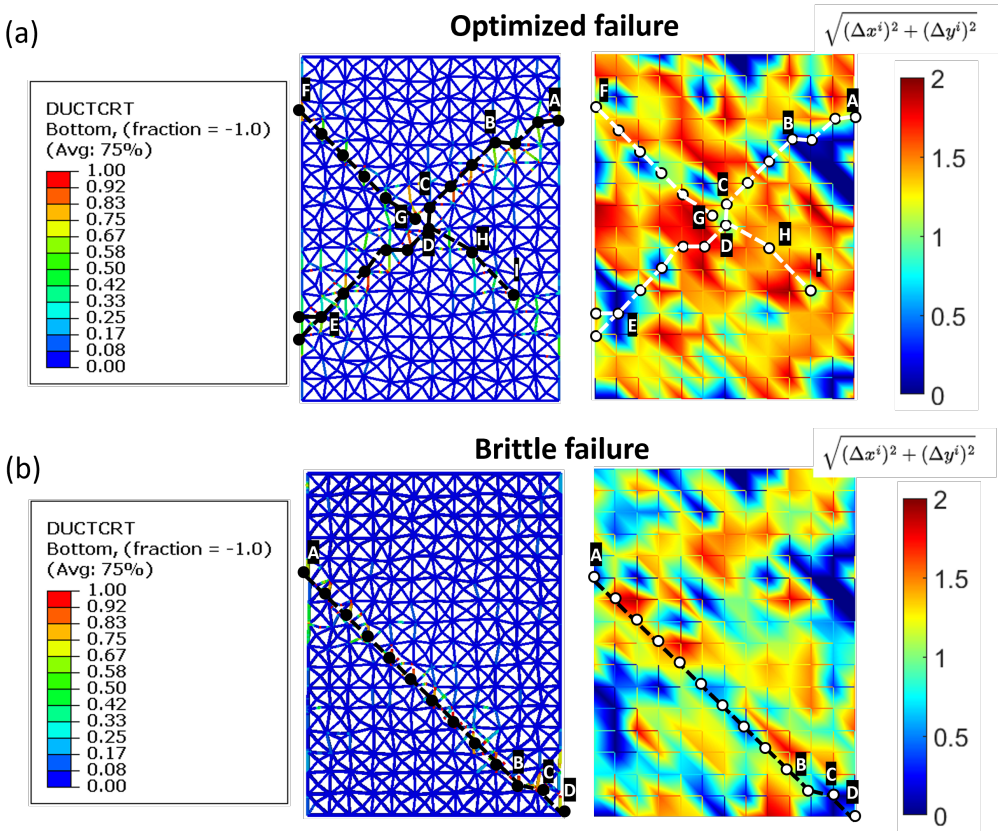

Figure 5.17: Failure mechanisms of two QTM designs: (a) an optimised QTM-N3 (b) a randomly selected low ductile QTM with brittle fracture

QTMs, the failure paths were initiated at the locations with a low level of disorderliness. For the optimised QTM (Figure 5.17 (a)), the breaking of struts was initiated at Point A and followed the path with minimum disorderliness, i.e., Points B and C for the formulation of a shear band; near Point C when the shear band encountered highly distorted area, shear band branching occurred and multiple shear bands started to formulate. In contrast, for the brittle QTM (Figure 5.17 (b)), the shear band branching did not occur owing to the absence of a highly distorted area on the failure path.

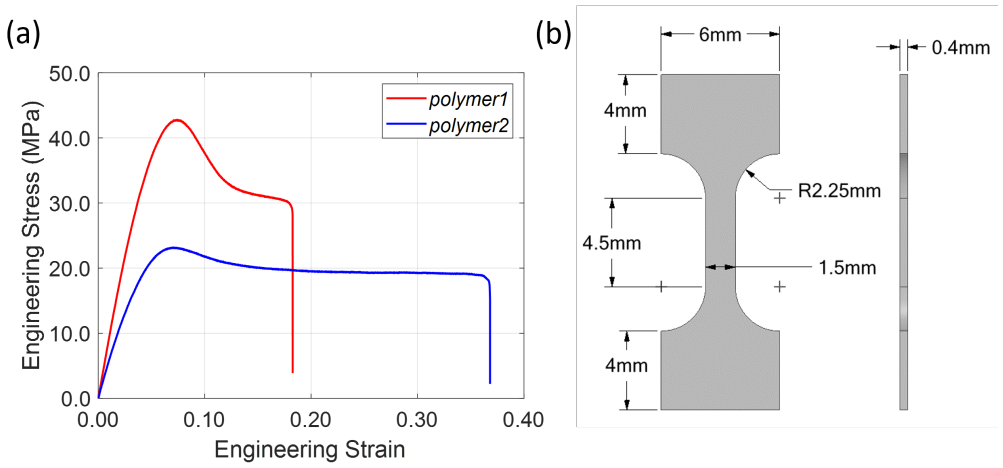

Figure 5.18: (a) engineering stress-strain curves of the *polymer1* and *polymer2*; (b) miniature specimen dimensions.

5.4 Experimental study

To validate the methodology described above, test specimens were manufactured, using the polyjet manufacturing technique, for the uniaxial tension test based on three selected FCC lattice designs, i.e., the parent periodic FCC lattice, the QTM with progressive failure mode (QTM-1), and the QTM with sudden failure mode (QTM-2). The optimised design shown in Figure 5.14 (d) was used as the geometry of the QTM-1; and the geometry of the QTM-2 was selected from the data used for deep learning, which exhibited sudden catastrophic failure mode according to the FE simulations. As discussed for the failure mechanism, the shear band branching was mainly caused by the distribution of initial disorderliness. To question if the failure modes of the lattices depend on the parent material, I chose polymers as the parent material instead of Aluminum alloy (Al1050A), which was used in the design optimisation as described previously. Two types of polymers (i.e., *polymer1* and *polymer2*) were used as the parent materials, which were created by combining commercialized acrylic (Objet Vero-Clear FullCure810) and rubber-like material (Objet Tango-Gray FullCure950). *Polymer1* has a mixture of 75% acrylic and 25% rubber-like

material, and *polymer2* has a mixture of 50% acrylic and 50% rubber-like material. Both polymers show elastic-plastic stress-strain response, with *polymer2* being much more ductile than *polymer1*. Figure 5.18 (a) shows the engineering stress-strain curves of *polymer1* and *polymer2*. A miniature specimen tensile tests were performed to get engineering stress-strain curves. The geometrical dimensions of the miniature sample are shown in Figure 5.18 (b).

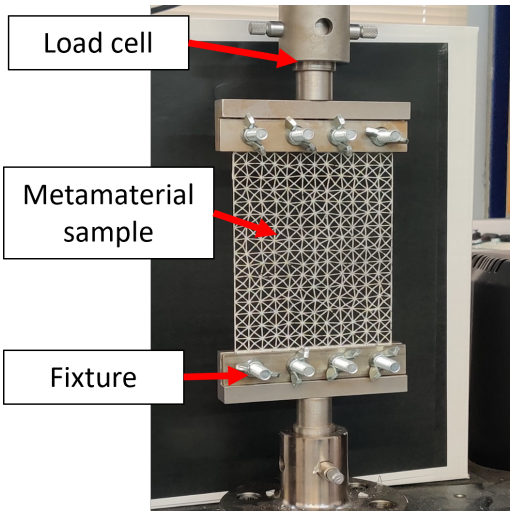

Figure 5.19: A typical 3D printed QTM-1 using *polymer1* sample and experimental setup

The tensile tests were conducted at room temperature using a 0.1% strain rate using an INSTRON testing system, as shown in Figure 5.19, for a photograph of the experimental setup. Each specimen contained 12 × 16 cells, and the geometry of the specimen had size 120 × 160 mm (with a height of 25 mm clamping at both top and bottom sides) with 1 mm out-of-plane thickness, and each strut had 0.4 mm thickness. The detailed geometry used for tensile tests of the three selected FCC lattice designs, i.e., the parent periodic FCC lattice, the QTM with progressive failure mode (QTM-1), and the QTM with sudden failure mode (QTM-2) are given in Figures 5.20 (a), (b) and (c), respectively. Digital image correlation (DIC) was employed to capture the full-field strain evolution of the samples during

the full fracture process. A CCD camera (Thorlabs DCC1545M) with an imaging lens (100 mm focal length) was configured at a spatial resolution of 5 pixels/mm and a frame rate of 20 fps. In the DIC algorism, the subset image was 128 × 128 pixels, and the step size was 64 pixels to maintain a high level of speckle correlation [175, 176].

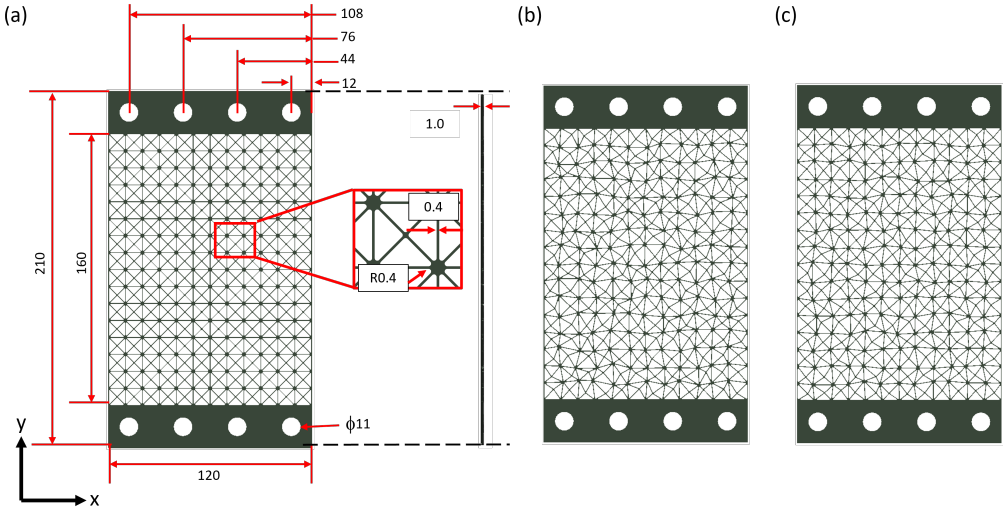

Figure 5.20: Geometry details of (a) the parent periodic FCC lattice (b) the QTM with progressive failure mode (QTM-1) and (b) the QTM with sudden failure mode (QTM-2) used for uniaxial tensile test (all dimensions are in mm)

The normalised macroscopic stress-strain curves for the specimens made of *polymer1* and *polymer2* are shown in Figures 5.21 (a) and 5.22 (a), respectively. For both parent materials, the periodic FCC lattice failed in a sudden, catastrophic manner. Compared to the periodic FCC lattice, the QTM-1 achieved a 60% increase in ductility for *polymer1* and a 33% increase for *polymer2*, respectively, without significantly decreasing the mechanical stiffness ($\leq$ 3%) and the strength ($\leq$ 13%). On the other hand, for both parent materials, the QTM-2 exhibited sudden, catastrophic failure mode with ductility either slightly higher (*polymer1*) or much lower (*polymer2*) than that of the periodic FCC lattice.

To further examine the failure mechanisms, a series of video snapshots at four selected tensile strains, numbered as "1", "2", "3" and "4" shown

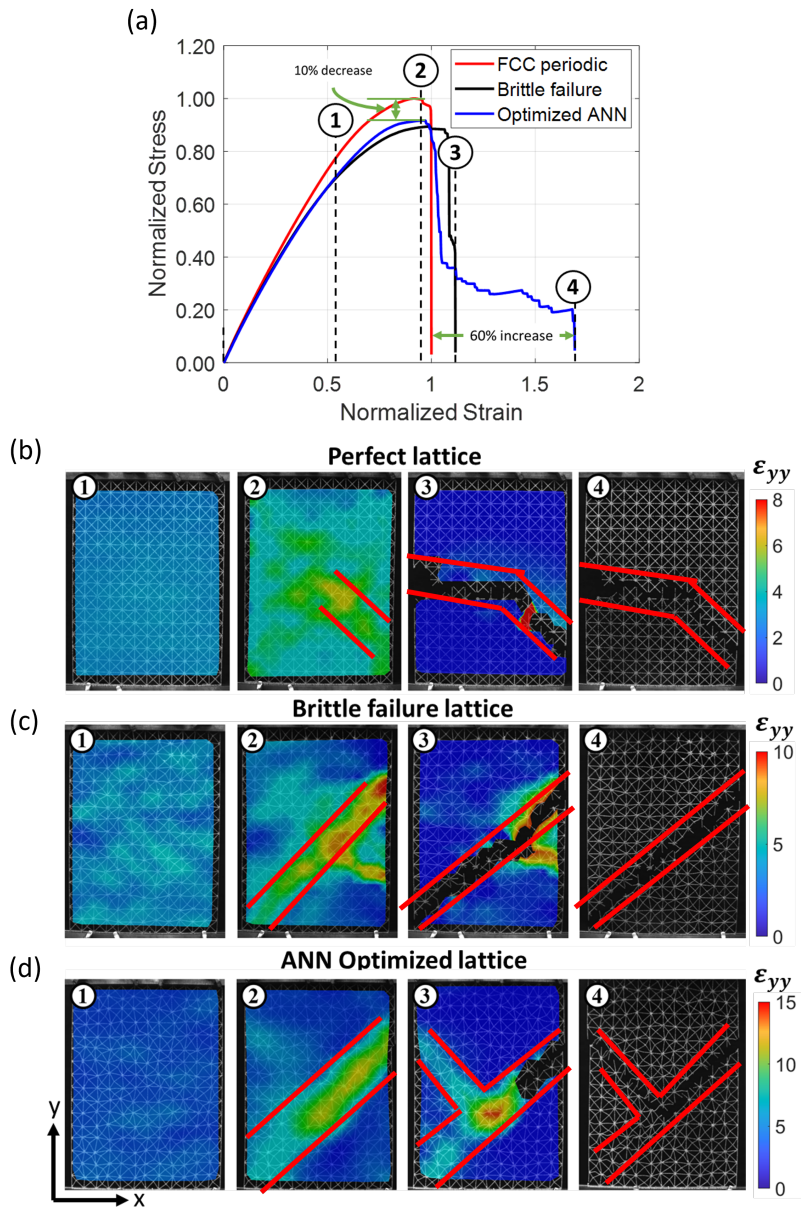

Figure 5.21: Tensile tests of the parent periodic FCC lattice, the QTM with progressive failure mode (QTM-1), and the QTM with sudden failure mode (QTM-2). (a) the normalised stress-strain curves of QTM-1 showing 60% increase in ductility using *polymer1*, (b), (c) and (d) snapshots of *polymer1* samples at different global strains during the test of parent periodic FCC, QTM-2, and QTM-1, respectively. The DIC images show the progression of microscopic strain ε_{yy} and shear band branching. (the fourth snapshots of parent periodic FCC lattice, QTM-1 and QTM-2 were taken after the final fracture occurred)

in Figures 5.21 (a) and 5.22 (a), were presented in Figure 5.21 (b)-(d) (*polymer1*) and Figures 5.22 (b)-(d) (*polymer2*), respectively. For both parent polymers, both the periodic FCC structure and QTM-2 fail instan-

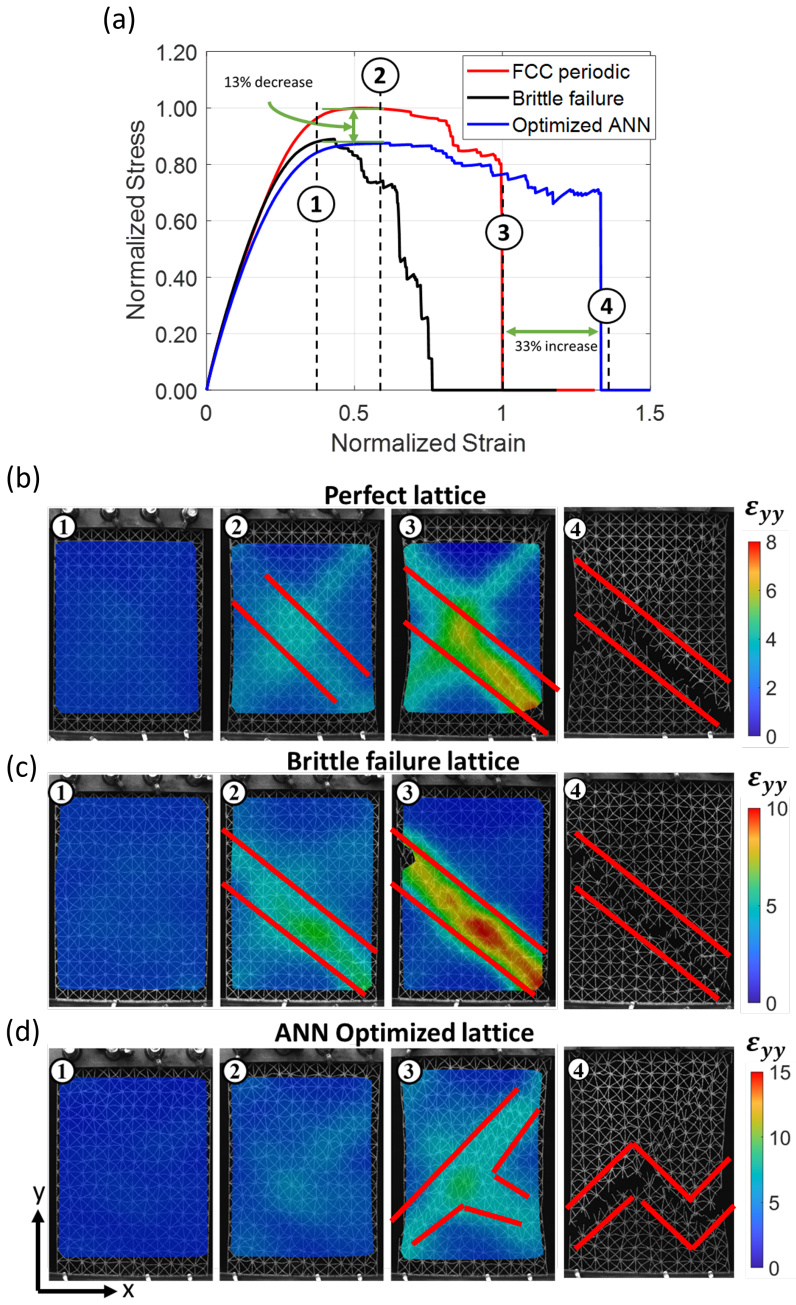

Figure 5.22: Tensile tests of the parent periodic FCC lattice, the QTM with progressive failure mode (QTM-1), and the QTM with sudden failure mode (QTM-2). (a) the normalised stress-strain curves of QTM-1 showing 33% increase in ductility using *polymer2*, (b), (c) and (d) snapshots of *polymer2* samples at different global strains during the test of parent periodic FCC, QTM-2, and QTM-1, respectively. The DIC images show the progression of microscopic strain ε_{yy} and shear band branching. (the fourth snapshots of parent periodic FCC lattice, QTM-1 and QTM-2 were taken after the final fracture occurred)

taneously owing to a single shear band formation across the sample at the tensile strain "3". Interestingly, the shear band deflection in Figure 5.21 (b) did not lead to progressive failure mode owing to the brittle parent material (*polymer1*). On the other hand, the QTM-1 design develops damage-tolerant behaviors via progressive failure modes owing to shear band branching (Figure 5.21 (d), *polymer1*) or excessive tortuosity in the development of the shear band (Figure 5.22 (d), *polymer2*).

5.5 Conclusion

The structures of the natural cellular materials exhibit a certain level of disorderliness. Prior to this work, it was well established that the disorderliness within cellular materials can cause a reduction in stiffness, strength, ductility, and fracture toughness. This has been demonstrated by a range of theoretical and experimental studies by Romijn et al. [137], Chen et al. [165], Tankasala et al. [149], and Xu et al. [177]. However, in this chapter, I have shown that the level and the distribution of disorderliness can either increase or decrease ductility of the truss lattice metamaterials by a great margin (see Figures 5.2 (a) and (b)), affecting both stiffness and strength. With this continuation, I have developed a physical-based data-driven framework, which tunes the disorderliness to achieve the QTMs with improved ductility. The higher ductility was achieved through changing the failure mechanisms from single shear band formulation to shear band branching or excessive shear tortuosity, which led to desired progressive failure modes. We have shown that, the solutions from the optimization calculation are not unique, which suggests that there is more than one optimum distribution of the disorderliness, however, they have all utilized progressive failure modes by arranging the nodes to improve the ductility. With this data-driven methodology, I can achieve the designs

with ductility increased up to 100% without losing much of their stiffness ($< 5\%$) and strength ($8 \sim 15\%$). Our numerical study has benefited from well-designed ANN deep-learning models, built upon a custom-built loss function (APPENDIX B.1.5, Figure B.3), which can be trained with a relatively small dataset. Additionally, the experiment study shows that the damage-tolerant designs obtained using this methodology are independent of parent material properties.

The design of damage-tolerant mechanical metamaterials [166] has significant importance in engineering applications. However, no deterministic approaches were developed prior to this work due to the indefinite solutions available. We believe this is just a beginning of an exciting field in the novel topological designs of mechanical metamaterials with tailored properties. Although the examples shown in the result section is based on FCC lattices, it is essential to note that the mechanical behaviours of other types of truss lattice such as Kagame, Diamond and Triangular, may differ from the FCC based lattices. It is likely that the difference in deformation mechanisms, i.e., bending dominated or stretching dominated, and redundancies of lattice structures [178] may lead to different damage tolerant behaviours with the presence of disorderliness. Future work will be conducted to reveal the underlying mechanisms via comparing different type of lattice structures. This study opens a new research area in seeking damage tolerance metamaterials, and the proposed method is general and applicable to other truss lattice topologies at any scale. The approach proposed in this paper can undoubtedly serve as a unique tool for designing novel mechanical metamaterials well beyond elastic limits.

Chapter 6

Creep characterisation of Inconel 718 lattice metamaterials manufactured by laser powder bed fusion

6.1 Introduction

In recent years, interest in manufacturing periodic or lattice metamaterials has continuously increased due to highly customized properties. Before advancing AM, other orthodox manufacturing technologies like investment casting, deformation forming, brazing etc., are studied to produce periodic lattice geometries. Limitations of such techniques include the fitness of the structures and the actual cell geometry [19]. Over the years, AM technologies have been developed to produce three-dimensional objects directly from a digital model by adding materials without specialized tooling. For example, LPBF or SLM can produce fine surface geometries like roughness value at 50 microns lattice structures using AM process for metal alloys. LPBF creates components layer by layer by melting specific parts

of a powder bed based on a 3D CAD model with a laser beam [148]. Sing et al. [179] used LPBF to manufacture complex cellular lattice structures and determined the factors most affecting their dimensional and mechanical properties. They found that the horizontal dimensions are primarily impacted by layer thickness, and vertical and diagonal dimensions are influenced mainly by laser power. The process offers benefits for producing complex components, especially in aerospace using superalloys, as it does not require tooling and directly uses CAD data [180]. However, there is limited research on how the high-temperature performance of LPBF components, such as their microstructures and mechanical properties, compares to those made through traditional methods [181]. For example, Inconel 718 is widely used in modern aircraft engines due to its high strength and elevated temperature resistance [182]. The material properties, such as precipitation and solid solution hardening, allow it to maintain strength and fatigue resistance at high temperatures up to 650 ℃[183]. However, its desired mechanical properties make it difficult to machine, requiring special tools and specific machining parameters [184].

In contrast, the LPBF process eliminates the issue of machinability, resulting in microstructures typically composed of columnar dendrites growing along the building direction [185]. Amato et al. [186] investigated the LPBF of Inconel 718 and examined the microstructure of the material and basic mechanical properties, such as hardness and tensile strength. Furthermore, because of the unique quality of the LPBF manufacturing process that allows for tailored mechanical, thermal and biological properties in the diffusion of lattices, trusses, and periodic materials could be found [20]. In conjunction with lightweight properties, lattice structures provide impact resistance, non-conducting heat properties and electromagnetic wave absorption [21–27, 187]. The study of lattice structure studies has continuously increased over the past decades. As a result, many researchers

are designing complex structures using lattices with different unit cells and relative densities. For example, Tancogne-Dejean & Mohr [164] studied a specific design which was an isotropic elastic structure with the combination of Simple Cubic (SC), BCC and FCC lattices. Through periodic homogenization, it was observed that isotropic truss lattices demonstrate lower initial yield anisotropy than the octet truss lattices. They developed a few cubic trusses lattice structures similar to the grid type, which were elastically isotropic. The study illustrated that the mechanical characteristics of grid-type of truss lattice structures change as per the direction of loading. Bonatti & Mohr [188] Performed finite element analysis and compression tests on stainless steel material specimens manufactured by AM and also examined statically-determinate solid octet truss lattice under large strain compression of different metamaterial architectures. It observed that hollow rhombic dodecahedral mesostructures provide nearly twice the strength and energy absorption of the octet truss. The smooth changes were due to structures becoming bending-dominated to stretching-dominant.

The high-temperature creep performance of LPBF-made Inconel 718 metamaterials has yet to be explored thoroughly. Creep is the primary failure mode at elevated temperatures, and a comprehensive creep design method is highly desirable to develop [189]. Andrews et al. [102] established expressions for the creep-bending of cell walls allowing the creep rate of honeycombs and foams to be predicted from the cell-wall properties and relative density. Fan et al. [104] investigated the uniaxial and multi-axial creep behavior of low-density open-cell foams and proposed a modified analytical expression by considering the mass at the strut node. Su, et al. [138] established an analytical model to predict the creep strain rate of imperfect honeycombs. It was observed in the study that the creep strain rate depends on the defects density as well as the type of missing struts of imperfect honeycombs. Monkman & Grant [190] Proposed an empirical

relationship between the minimum creep rate and rupture life at elevated temperatures by analyzing the steady-state creep rate. However, the creep performance of the metamaterials due to microstructure defects owing to the LPBF manufacturing process is still an issue.

As part of a more in-depth study, this chapter aims to investigate the creep characteristics of LPBF-manufactured Inconel 718 metamaterials. Instead, the creep behavior and effects of LPBF-made Inconel 718 metamaterials microstructural defects have been assessed. In this work, I have accurately captured the microstructure defects using Kachanov's creep damage model. In addition, the paper examines the leading causes of specimen failure and the effects of loading and relative density on creep life.

6.2 Material and experimental testing

6.2.1 Material and manufacturing

The chemical composition of the Inconel 718, to manufacture metamaterial produced by LBPF investigated in this study given in Table 6.1. The powder particles constituted a spherical shape and an average size of 30 µm between 15 µm and 45 µm. The metamaterial specimen consisted of BCC as basic unit cells, consisting of four equilateral triangles with 12 rectangular struts. The size of this unit cell is 4 mm, and the nominal thickness is 0.5 mm in both directions. The overall size of the structures is $32 \times 32 \times 80$ mm (composed of $8 \times 8 \times 20$ cells). Figures 6.1 (a) and (b) show the schematic metamaterial design with unit cell dimensions. Using the heat-treatment strategy, I heat-treated the specimens to improve the material properties (see Table 6.2 [16]). Figure 6.1 (c) shows the three as-built samples of metamaterials with a building plate. The build plate was removed via wire cutting, maintaining the strut thickness of 0.5 mm.

The relative density $\bar{\rho}$ of the BCC unit cell truss lattice material (ratio of the density of the lattice material to the density of the solid material from which it is made) is given by:

$$\bar{\rho} = \left(1 + \sqrt{3}\right)\left(\frac{2t}{l}\right)^2 \tag{6.1}$$

The strength of a stretch dominated lattice structure with 10% relative density is three times stronger than an equivalent bending dominated foam [147, 148]. Thus, the relative density value was taken as 0.13 for our investigation, considering the manufacturability of the minimum strut diameter [149].

Table 6.1: Chemical composition of the main elements in Inconel 718 powder (wt %)

Elements	in	weight	percent	(wt%)	
Ni	Cr	Fe	Nb	Mo	Ti
$50-55$	$17-21$	remainder	$4.8-5.5$	$2.8-3.3$	$0.7-1.2$
Al	Co	Mg	Si		
$0.2-0.8$	≤ 1.0	≤ 0.35	≤ 0.35		

Table 6.2: Heat treatment procedures for cast Inconel 718 components

Homogenization	Heat to 1093 °C±14, hold for 1–2 h, air cool or faster
Solution	Heat to 954–982 °C, hold for $\geq$ 1 h, air cool or faster
Ageing	Heat to 718 °C±8, hold for 8 h,
	furnace cool to 620 °C±8 in 1 h, hold for 10 h, air cool or faster

6.2.2 Microstructure characterisation

The microstructure of the Inconel 718 under creep tests was characterised by SEM equipped with an X-ray analysis system and 80 mm^2 silicon drift detector (SDD). Fractographic inspections were implemented on the fracture surface of the lattice specimens. Ruptured surfaces were sectioned from these specimens using electrical discharge machining (EDM), cleaned

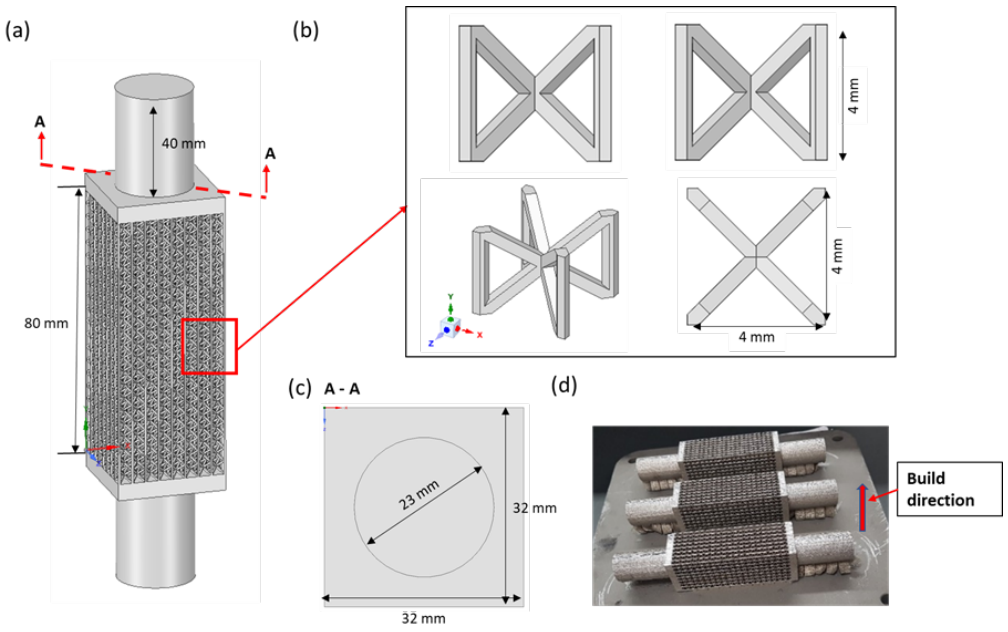

Figure 6.1: (a) CAD geometry of a BCC metamaterial with dimensions, (b) unit cell dimension of a BCC cell, (c) specimen clamp geometry dimensions, and (d) as-built specimens showing built direction with building plate

in an ultrasonic bath, and mounted on SEM stubs for imaging. A JEOL 7000F field-emission SEM was employed to characterise fracture surfaces at a working distance of 15 mm and an accelerating voltage of 15 kV. Energy-dispersive X-ray spectroscopy (EDS) analysis was conducted using the Oxford Aztec software to confirm the nature of fractures. The working distance for EDS analysis was 11.5 mm, and the accelerating voltage was 20 kV.

6.2.3 Experimental setups

Tensile test at elevated temperature

It is essential to identify the yield strength of the metamaterials since any stress applied higher than the yield stress can lead to plastic deformation, leading to failure before the creep fracture has fully developed. Hence, the yield strength, tensile strength and elongation of the bulk and lattice structure specimens during tension were evaluated by uniaxial tensile testing at

650 °C temperature and a constant strain rate of 0.02 mm/sec on the Mayes ESM250 testing rig. The rig was fitted with a Mayes 250 kN load cell on the crosshead (a horizontal bar across the top part of the rig), which was used to measure the force during the test. The load cell also had the capability of measuring displacement in the region of the crosshead. A Mayes 240V split section resistance furnace was used to maintain the required temperature. The furnace body is split into two halves and hinged to accommodate easy sample insertion. The temperature in the furnace, along the gauge length of the specimen, was measured using three K-type thermocouples spaced out along the specimen's gauge length surface. Two thermocouples were placed at the top and bottom edges of the gauge length, and a third one was in the middle. The furnace had three independent heating elements, and each of them was connected to a thermocouple. The data from the thermocouples were used to adjust the temperature within the furnace, and the samples were equilibrated at the test temperature for 30 min before testing. The testing equipment was located in a room with a controlled air temperature of around 20°C. The ends of the sample under testing were positioned in the designated holders with threads. The displacement was measured close to the boundaries of the gauge length. The displacement along the gauge length of the sample was measured using a pair of LVDT-0582 high-temperature side-contact linear voltage differential transformer (LVDT) extensometers. The several key components of the Mayes ESM250 testing rig are shown in Figure 6.2.

creep rupture tests

Creep tests were also carried out on the Mayes ESM250 testing rig. As mentioned in the above section, to reduce the influence of non-creep induced plastic deformation, uniaxial tension creep experiments were performed at the initially applied load levels of 35% and 70% of yield strength of

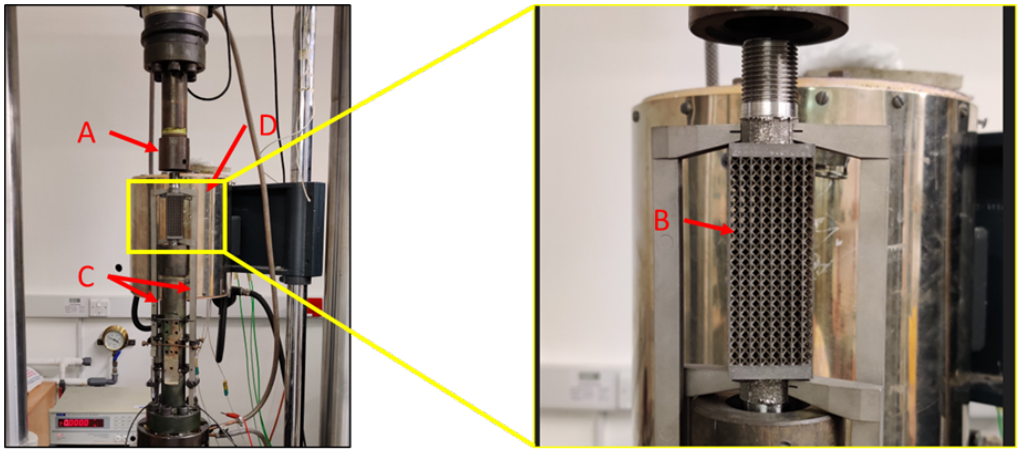

Figure 6.2: Testing rig based on the Mayes ESM250 electromechanical testing machine, used to conduct experimental tensile tests, consisting of; "A" crosshead with a load cell, "B" metamaterial specimen, "C" a pair of linear voltage differential transformer extensometers.

metamaterials obtained via a tensile test in the air at 650 ℃. The sample temperature was controlled by employing three thermocouples at the top, centre, and bottom of the specimen gauge length to ±0.5 ℃ of the set point. Creep strain measurements were obtained using an LVDT extensometer attached to the end sections of the specimen gauge length.

6.2.4 Numerical modelling

Numerical and material modelling for tensile test

To identify the yield strength of the metamaterial, a tensile test at elevated temperature has been performed, and a numerical model has been deployed for numerical validation. The numerical model was established using finite element software ABAQUS/EXPLICIT . Timoshenko beam elements with linear interpolation functions (element type B31 in ABAQUS [143]) were adopted to improve computational efficiency and ensure the accuracy of the simulations [191]. Numerical tests have suggested that converged results can be achieved with each strut meshed with 5 beam elements of equal length. All nodes on the bottom side of the lattice structure were con-

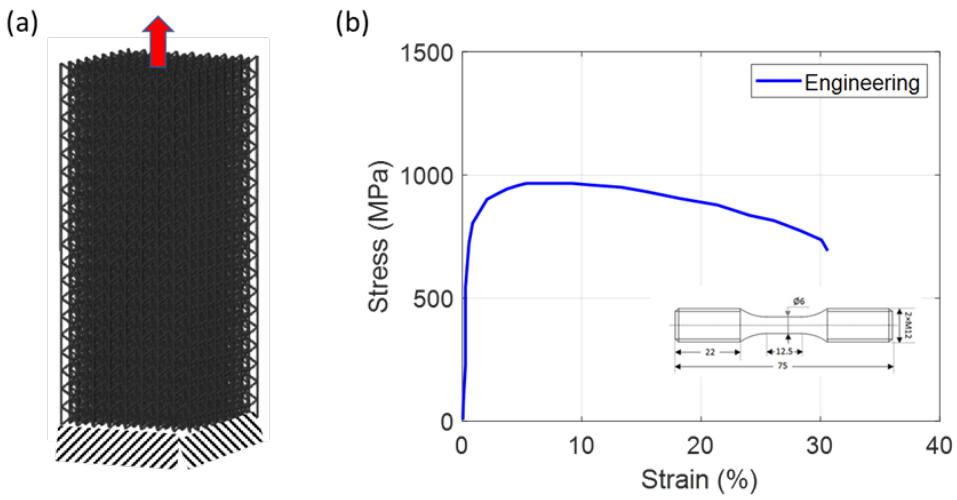

Figure 6.3: (a) Finite elements models of the lattice structure (b) Engineering stress-strain curves of LBPF manufactured as-built uniaxial tensile specimen (Inconel 718) under tensile test at 650 ℃

strained in translation and rotation degrees of freedom. All translational and rotation degrees of freedom were restricted for the upper surfaces of the structures except for the loading direction, as shown in Figure 6.3 (a). Displacement control and smooth analysis were imposed to ensure the simulation was a quasi-static process. The quasi-static process was verified by maintaining the kinetic energy of the system at less than 5% of its internal energy.

The Ramberg-Osgood model was used to represent the true stress-strain relationship of the parent material, i.e., additively manufactured Inconel 718, as illustrated in Figure 6.3 (b) [192]:

$$\bar{\varepsilon} = \frac{\bar{\sigma}}{\bar{E}} + \kappa \left(\frac{\bar{\sigma}}{\bar{\sigma}_y} \right)^n \tag{6.2}$$

where $\bar{E} = 202$ GPa and $\bar{\sigma} = 755$ MPa are Young's modulus and yield stress of the Inconel 718, respedtively; κ is the yield offset, and n is the hardening exponent. Thus, this material model is suitable for capturing the mechanical behavior of LBPF manufactured as-built uniaxial tensile specimen (Inconel 718) under a tensile test at 650 ℃.

Failure initiation starts when the maximum axial strain reaches 0.3 in the element based on the tensile test result shown in Figure 6.3 (b). The strut necking behaviour was replicated by the reduction of the yield stress after failure initiates, which is characterised by the damage variable D:

$$\bar{\sigma} = (1 - D)\bar{\sigma}_y \tag{6.3}$$

where D varies from 0 to 1, and is a function of the plastic strain, fitted to match the data of Figure 6.3 (b). The corresponding element was deleted from the mesh when all the material points within the element failed ($D = 1$).

Kachanov's creep damage equations

In order to understand the creep damage evolution in the material, including the tertiary stage of creep deformation, the creep damage model, originally proposed by Kachanov [100] and Rabotnov [193], has been shown to be reasonably accurate in predicting the tertiary creep behaviour of the materials. Incorporating the damage state parameter ω, the creep stain rate is defined as follows :

$$\frac{d\varepsilon^c}{dt} = A\left(\frac{\sigma}{1+\omega}\right)^{\eta} t^m \tag{6.4}$$

where ε^c, σ and t are the creep strain, the uniaxial stress and the time, respectively. The material constants A and η are the Norton law constants, which control secondary creep behaviour, and can be determined from a log-log plot of the creep strain rate versus the applied stress [194], while the material constant m controls the primary creep strain. The damage parameter ω ranges from 0 to 1 corresponding to no damage state and fully failure of materials, respectively. The creep damage rate as a function of stress and current damage is described as:

$$\frac{d\omega}{dt} = M\frac{(\sigma_r)^{\chi}}{(1+\phi)(1-\omega)^{\phi}}t^{m} \tag{6.5}$$

where, M, ϕ and χ are continuum damage material constants. ω is the damage parameter having a value in-between 0 (no damage) and 1 (100% damage/failure). The rupture stress σ_r is a dependent variable whose values change as per maximum principal stress σ_1 and equivalent stress σ_{eq} as defined by below equation:

$$\sigma_r = \delta\sigma_1 + (1-\delta)\sigma_{eq} \tag{6.6}$$

The above equation is suitable for mixed stress criteria of the material, where δ is a material constant related to the tri-axial stress state of the material range from 0 to 1 . The value of δ determines the maximum principal stress dominant at 1 and equivalent stress dominant at 0 , which is important for the multiaxial damage model. Although, the notched specimen uniaxial test needs to be performed to determine the value of δ [195]. In our case, the value of δ is zero since I have used the Timoshenko beam elements with linear interpolation functions (element type B31 in ABAQUS [143]).

6.3 Determination of high-temperature properties at 650 ℃

6.3.1 Tensile Properties

Figure 6.4 (a) compares the macroscopic stress-strain responses of the meta-materials subjected to uniaxial tension at 650 °C obtained via experiment and numerical calculation. The x-axis represents the applied macroscopic strain on the material, and the y-axis represents the corresponding macro-

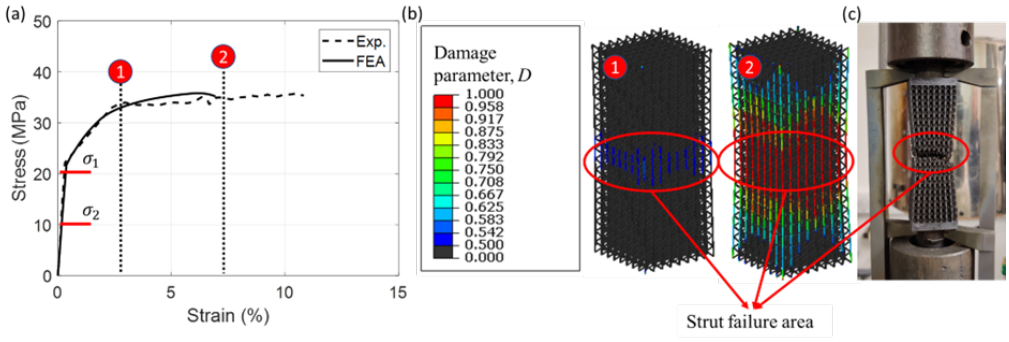

Figure 6.4: (a) A comparison between stress-strain curves obtained via experiment and FEA of a lattice specimen at 650 ℃. (b and c) the strut damage parameter of numerical calculations and experimental result after final fracture, respectively.

scopic stress. The dashed curve represents the experimental results, and the continuous curve represents the results from the numerical simulation. It can be observed that both curves show very similar behaviors, which suggests that our numerical simulation could achieve high fidelity. The macroscopic stress-strain response has been used to identify two loading conditions for the creep test, i.e. 35% and 70% of yield strength (10 kN and 20 kN), as shown in Figure 6.4 (a). In Figure 6.4 (b) and (c), I have shown the strut damage parameter of numerical calculations and experimental results at fracture, respectively.

6.3.2 Creep properties and damage parameters estimation

In this section, I have used Kachanov's creep damage equation to calculate damage parameters. For relatively simple one state variable, Kachanox equations, Eqs. (3) and (4), the material constants A, η, m, M, ϕ and χ can be determined directly by fitting the uniaxial strain-time equation to a few uniaxial strain-time curves, obtained from creep tests at a given temperature.

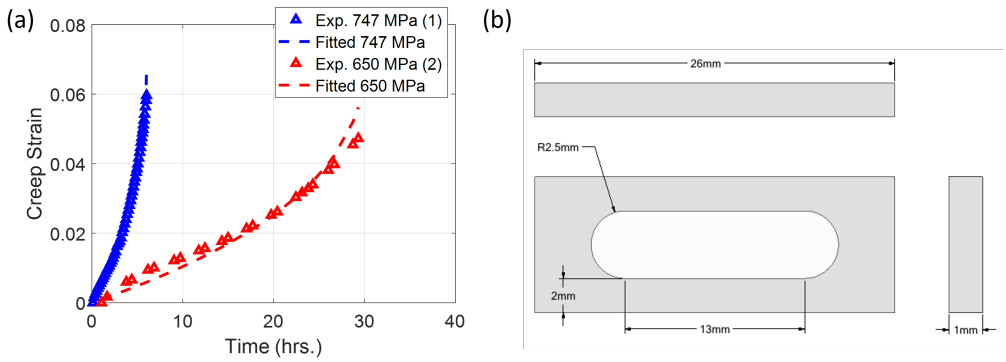

Figure 6.5: (a) Fitted and tested uniaxial creep strain curves of the parent material ((1)-[15], (2)-[16]) (b) dimensions of the Two bar specimens (TBS) [17, 18]

Figure 6.5 (a) shows the correlation between experimental and analytical data estimated through curve fitting at 650 MPa and 747 MPa stresses. The experimental creep curves have been reported by Xu et al. [16] subjected to 650 MPa and Xu et al. [15] subjected to 747 MPa stress conditions for Inconel 718 at an elevated temperature of 650 ℃. The estimated damage parameters obtained from the literature after curve fitting are given in Table 6.3. The damage parameters given in Table 6.3 are based on the Two bar specimens (TBS) [15–18], dimensions shown in Figure 6.5 (b). In their work, the TBS specimen surfaces were ground and polished before testing to remove the milling-affected zone containing machining defects. However, due to the complexity of the metamaterial used in this work, the lattice strut surfaces have experimented on as-built conditions. In addition, owing to manufacturing defects consisting of microstructure defects, the damage parameters were corrected for the creep material modelling. The inverse method mentioned by Wen et al. [196] was used for correction of the damage parameters. The updated damage parameters after the correction have also been provided in Table 6.3. The microstructures at the fracture surfaces of the metamaterial specimens have been discussed in the results section of this paper.

Table 6.3: Creep damage material constants (stress in MPa and time in hours) from literature and after correction

Material Property	from literature	after correction
A	3.54×10^{-35}	4.54×10^{-35}
η	11.167	11.9
m	0	0
M	5.13×10^{-35}	4.44×10^{-35}
ϕ	15.25	12.0
χ	11.662	5.416
δ	0	0

6.4 Results and discussion

6.4.1 Creep behaviour

Figures 6.6 (a) and (b) show the correlation between experimental and FEA results under 20 kN and 10 kN loads, respectively. For 10 kN loading condition, the numerical result has accurately captured the creep behaviour, whereas for 20 kN the numerical result is reasonably close to experimental result of metamaterials at 650 ℃. Furthermore, at the 20 kN load, the metamaterial fails very early owing to brittle fracture compared to the 10 kN loading. The differences in the creep life of metamaterials show that the failure mechanisms have been significantly affected by loading conditions. Figures 6.7 (a) and 6.8 (a) show the progression of the displacement, and Figures 6.7 (b) and 6.8 (b) show the creep damage evolution at the struts of the metamaterials at three different snaps at different loading conditions. It shows that the creep damage at the 20 kN load increases continuously, and the onset of crack at the edge of the specimen occurs. However, at the 10 kN load, the creep damages are broadly distributed, leading to higher

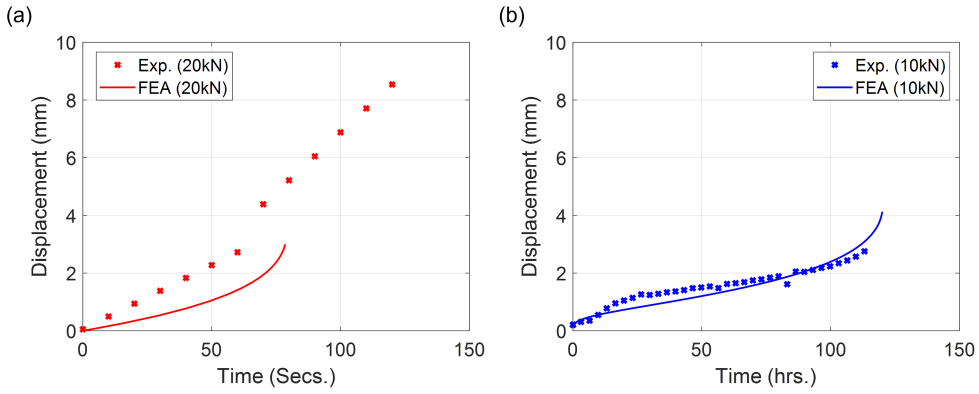

Figure 6.6: Creep life versus displacement curves showing the correlation between experimental versus FEA results of metamaterials samples under (a) 20 kN and (b) 10 kN loads at 650 ℃

creep life.

6.4.2 Microstructures and fracture characteristics

Figure 6.9 (a) shows the overview of the fracture surface for metamaterial samples under a 10 kN load. The onset of crack was observed at the edge of the specimens, which propagated transversely. To investigate the nature of failure, the fracture surface where the crack initials were examined using SEM. The fracture surface of metamaterials samples under 10 kN load exhibit a co-existence of brittle and ductile features, as shown in Figures 6.9 (c) and (f). Figure 6.9 (c) shows the region of transgranular cleavage with typical feather markings and river patterns, which indicates a feature of brittle fracture in this area. A microcrack of approximately 400 µm (Figures 6.9 (b) and (e)) was observed, which might be the main reason for structural failure. In addition, a region of the quasi-cleavage surface was found in the vicinity of the microcrack. The appearances of quasi-cleavage were similar to those reported by Martin et al. [197] and Lynch [198], which may attribute to the coalescence or growth of micro-voids that initiate within intense slip band intersections or form due to insufficient melting of the additive manufacturing. Figure 6.9 (f) shows typical deep dimples

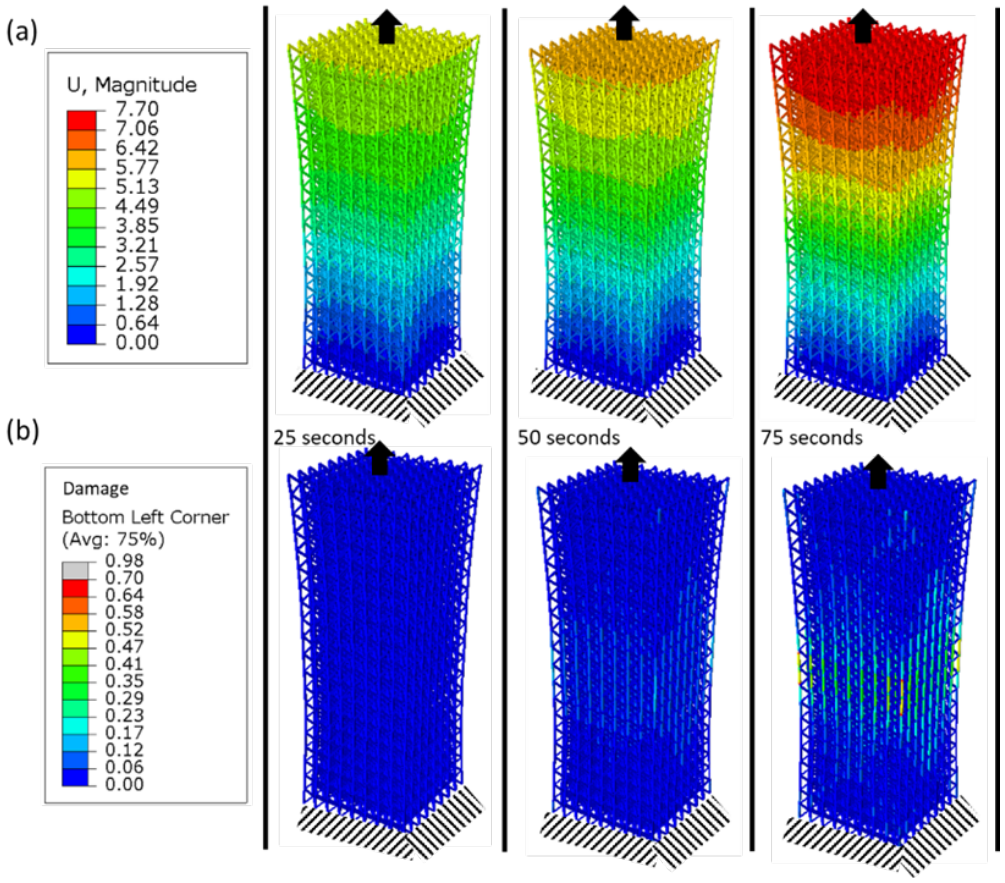

Figure 6.7: Creep behaviour of the metamaterials showing the progression of (a) displacement and (b) creep damage at different times at 20 kN load

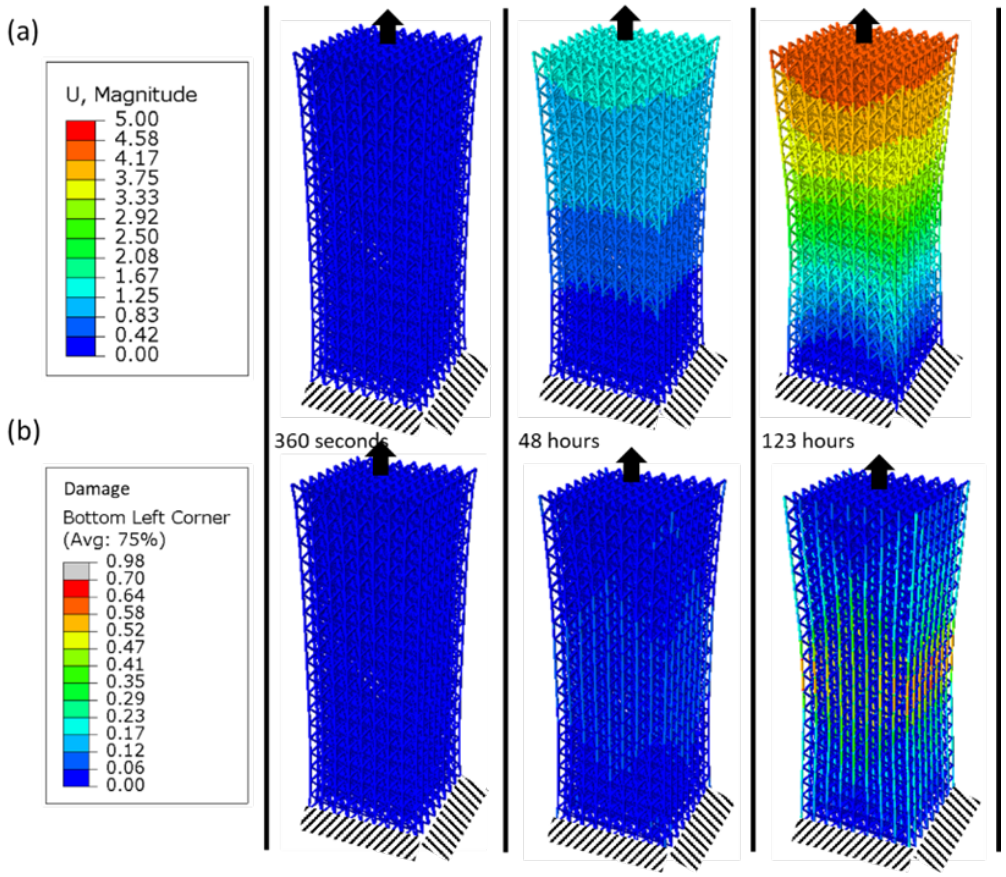

Figure 6.8: Creep behaviour of the metamaterials showing the progression of (a) displacement and (b) creep damage at different times at 10 kN load.

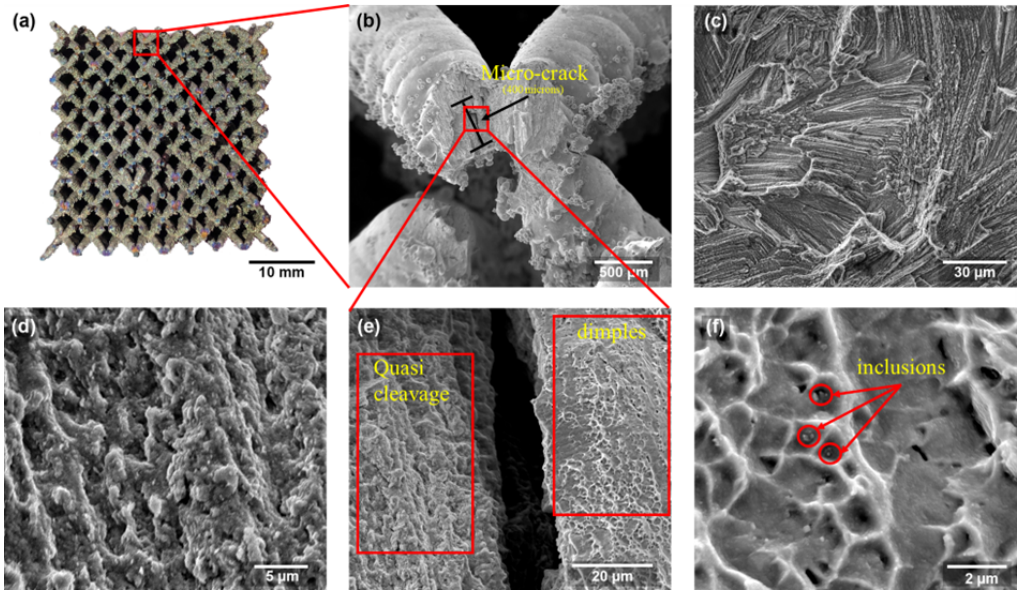

Figure 6.9: (a) An overview of the fracture surface for the specimen failure under 10 kN load. (b) The fracture surface of the crack initiates. (c) Fracture features at the region of transgranular cleavage. (d) Fracture features at quasi-cleavage surface. (e) Co-existence of brittle and ductile features in the vicinity of the microcrack. (f) Deep dimples with inclusions near the microcrack.

with a certain amount of inclusions near the microcrack, which suggests a ductile failure in this region. The presence of inclusions, microcracks and deep dimples may cause local softening under the tensile load and further result in the combination of brittle and ductile fracture under 10 kN, as shown in Figures 6.6 (a) and (b).

Figure 6.10 (a) shows the overview of the fracture surface for the metamaterial sample under a 20 kN load. The SEM images of the fracture surface where the crack initiates exhibit a typical brittle failure, as shown in Figures 6.10 (b) and (c). Unlike the sample that failed under a 10 kN load, a clear transgranular cleavage without any inclusions was observed across the whole fracture surface. A region with dull spots shows an alternating light, and a dark feature was found at the edge of the cross-section of the lattice truss, as shown in Figure 6.10 (c). EDS analysis was implemented to further confirm the composition of the element at dull spots. The x-ray

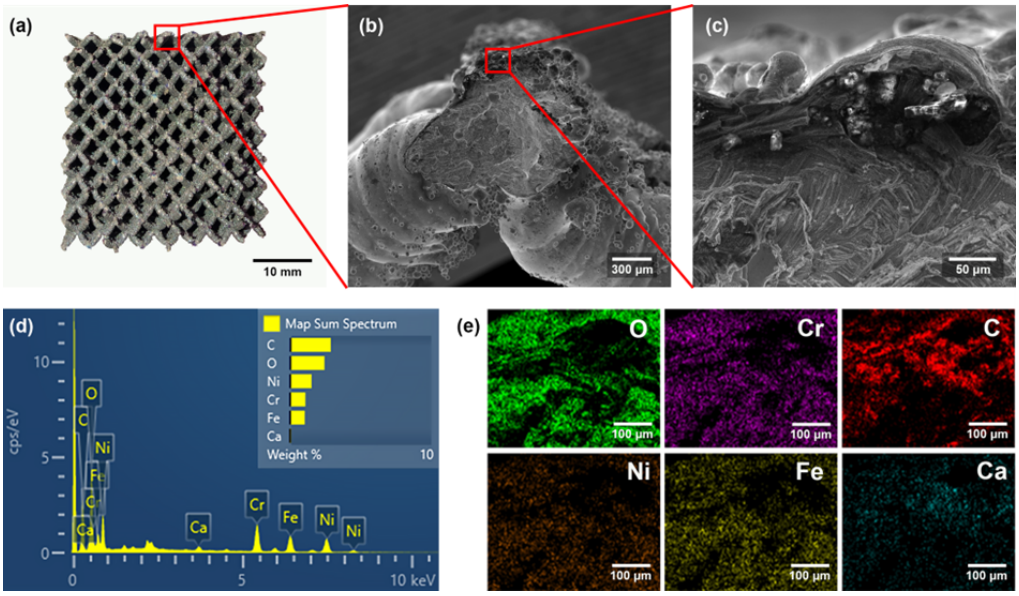

Figure 6.10: (a) An overview of the fracture surface for specimen failure under 20 kN load. (b) The fracture surface of the crack initiates. (c) EDS mapping area of the dull spots region. (d) and (e) X-ray emission spectrum and EDS elemental mapping at the dull spots region, respectively.

emission spectrum (Figure 6.10 (d)) and EDS elemental mapping (Figure 6.10 (e)) indicate that the alloying elements were a mixture of oxygen, chromium, carbon, nickel, iron, and calcium. Although there is a limited basis in literature to claim that carbides may directly lead to an earlier failure, the presence of carbides cannot be considered as benign in additive manufacturing as it can increase the local hardness and behave as a source of crack nucleation that reduces the local strength and toughness.

6.4.3 Creep performance of metamaterials

Here, I have shown the creep performance of the metamaterials at different loadings and relative densities obtained via numerical calculations. Figures 6.11 (a) and (b) show the impact of loading conditions and relative density on the creep life of metamaterials, respectively. Figure 6.11 (a) shows that the experimental data and FE results correlate reasonably. The X-axis shows the loading conditions and relative densities in Figures 6.11 (a)

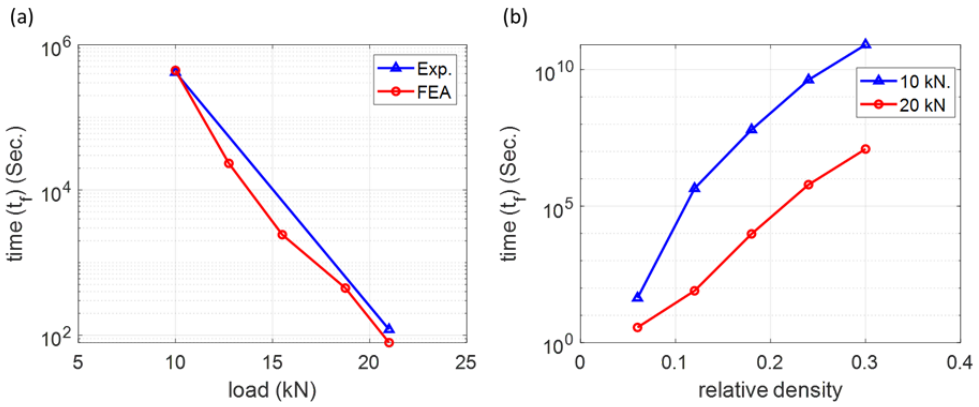

Figure 6.11: (a) The impact of loading conditions on the creep life of metamaterials comparison between test data and FE data; (b) The increase in creep life with respect to relative density obtained via FE calculations.

and (b), respectively, and the creep life has been plotted on the Y-axis on a logarithmic scale. It can be observed that the creep life decreases significantly with the loading, and the creep life has been plotted on the y-axis on a logarithmic scale. The relative density of the metamaterial designs was obtained by adjusting the strut thickness, t and maintaining other parameters constant in the numerical model. It can be observed that the creep life decreases significantly with the loading, and the creep life increases with the relative density. Additionally, the impact of relative density of the metamaterials are significant on creep failure life, subjected to different loading conditions.

6.5 Conclusion

This study investigated the creep behaviour of lattice metamaterials manufactured by LPBF using Inconel 718 at an elevated temperature of 650 ℃. The microstructural defects, such as suboptimal grain size and morphology, and macroscale anomalies, such as lack of fusion, present in LPBF materials led to performance degradation for creep mechanical properties. Through the use of microstructural characterisation and Kachanov's damage mod-

elling, it has been found that the creep performance of the metamaterials was affected by the microstructure defects. I have shown that, due to the LPBF, which can result in the presence of inclusions, microcracks, and deep dimples, local softening may occur under tensile load leading to an earlier failure compared to conventional manufacturing processes. Furthermore, the numerical calculations and experiment results showed a logarithmic decay in creep life with increased applied load. This is caused by high stress induced on the struts of the metamaterials, which leads to early failure owing to plastic deformation. Note that Kachanov's model does not consider plasticity damage, and viscoplastic model is recommended for higher loading.

These findings provide a deeper understanding of the creep behaviour of LPBF metamaterials and can inform the optimisation of LPBF manufacturing processes to improve the mechanical properties of metamaterials. The microstructure study shows that the improvements in the LPBF manufacturing parameters can influence the creep life of metamaterials significantly. However, the paper does not address important topics, such as the impact of strut size effects, LPBF building direction and residual stress on creep testing. Therefore, it is recommended for future study that to represent the size effect; ideally, miniaturised tensile and creep tests (approx. 0.5 mm specimen, i.e., size of the strut) at 650 ℃, should be carried out to derive the material properties, for lattice modelling. Additionally, future work needs to be conducted by undertaking more creep testing and modelling with different parameters such as loads, temperatures, and lattice types to allow a better understanding of the creep behaviour of metamaterials.

Chapter 7

Conclusion and Future Work

This thesis aims to investigate the the field of mechanical metamaterials by exploring their failure mechanisms, mechanical characteristics, and creep behaviour. The objective include: (1) to numerically investigate macroscopic elastic-plastic behaviour and failure mechanisms of truss metamaterials with defects under multi-axial loading; (2) to develop a data-driven framework to optimise the distribution of disorderliness to achieve damage tolerance metamaterial designs with the increase in ductility at the minor expense of stiffness and tensile strength; (3) to understand the creep behaviour and effects of microstructures of the metamaterials manufactured by 3D printing technology. To achieve these objectives, the related work has been presented from Chapter 4 to Chapter 6, and the conclusions have been provided below. Afterwords, the future works have been discussed based on the conclusions of the current study.

7.1 Conclusion

7.1.1 Localisation and coalescence of imperfect planar FCC truss lattice metamaterials

In summary, this chapter has undertaken an exploration of the influence of stress triaxiality on the failure mechanisms intrinsic to anisotropic perfect and imperfect planar FCC truss lattice metamaterials. Within the scope of this study, various forms of imperfections, including distorted struts, missing struts, and strut diameter variations, have been meticulously incorporated into the numerical modelling. A novel numerical framework has been introduced, aimed at surmounting computational challenges that extend beyond the elastic regime.

Throughout the course of this investigation, three distinct modes of microscopic localisation within both perfect and imperfect lattices have been identified prior to eventual failure: the formation of crushing bands, shear bands, and void coalescence. The findings affirm that distorted lattices exhibit a propensity for shear band localisation, particularly as distortion levels increase. Conversely, missing lattices predominantly experience failure through void coalescence, especially in instances of high missing strut defects. Notably, the variation in strut diameter, within the selected range, does not exert a significant influence on the macroscopic mechanical response and strain localisation.

This work endeavours to pave the way for the predictive understanding of failure mechanisms in imperfect lattices under diverse loading conditions. However, it is imperative to acknowledge that the present study assumes failure of the RVE when the maximum failure strain is reached for any strut contained within the RVE. Future investigations should expand their scope to consider the effects of parent material damage and the potential

interplay of defects when multiple types and sizes of defects coexist.
In conclusion, this chapter contributes valuable insights into the intricate behaviour of lattice metamaterials, shedding light on the nuanced relationship between stress triaxiality and failure mechanisms while also offering a promising foundation for future research endeavours in this field.

7.1.2 Data-driven discovery of quasi-disordered mechanical metamaterials failed progressively

In this work, I have demonstrated that the degree and distribution of disorder in truss lattice metamaterials can significantly impact their ductility, leading to either an increase or decrease in ductility, affecting both stiffness and strength. To take advantage of the geometrical disorderliness, I have created a framework based on physical principles and data-driven methods that allows us to adjust the degree of disorder in order to produce truss lattice metamaterials with higher ductility and better mechanical properties. I have demonstrated that the results obtained from the optimization process are not necessarily unique, implying that there are multiple optimal distributions of disorderliness. Nonetheless, all of these distributions have utilized progressive failure modes to enhance the ductility. The obtained designs showed that, it is possible to achieve designs that exhibit up to a 100% increase in ductility while only losing ($< 5\%$) of their stiffness and ($8 \sim 15\%$) of their strength. Additionally, The method has been validated by using two different types of polymers as the parent material in the experimental study, which also have demonstrated that the enhanced damage tolerant behaviors of the optimized metamaterials are material independent.

7.1.3 Creep characterisation of Inconel 718 lattice metamaterials

In this chapter, through the use of microstructural characterisation and Kachanov's damage modelling, I have investigated the creep behavior of Inconel 718 metamaterial, and the results indicate that the creep resistance depends on the microstructure and loading conditions. The creep behaviour of metamaterials is significantly different from that of bulk materials due to their complex structures. Furthermore, LPBF materials exhibit performance degradation in creep mechanical properties due to the presence of microstructural defects such as suboptimal grain size and morphology, as well as macroscale anomalies like lack of fusion. The results of this study, provide insights into the creep behavior of LPBF metamaterials and could aid in optimising LPBF manufacturing processes to enhance the mechanical properties of these materials.

7.2 Future work

The scope of the research question was to investigate mechanical metamaterials by exploring their failure mechanisms, mechanical characteristics, and creep behaviour. can be programmed and tuned to respond to mechanical actuation. This has been shown from Chapter 4 to Chapter 6. However, the research has highlighted several avenues of future work required to reaffirm arguments made within the study, to better understand the failure mechanisms, the requirement to further develop the data-driven process for future applications and to further study creep behavior of the metamaterials.

In Chapter 4, an numerical framework was developed to describe the failure mechanisms of the FCC metamaterials by introducing different manufac-

turing defects. Although the examples shown in the result section is based on FCC lattices, it is essential to note that the mechanical behaviors of other types of truss lattice such as Kagame, Diamond and Triangular, may differ from the FCC based lattices. It is likely that the difference in deformation mechanisms, i.e., bending dominated or stretching dominated, and redundancies of lattice structures [178] may lead to different behaviors with the presence of manufacturing defects. Additionally, it should be noted that the present study assumes that failure of the RVE occurs when the maximum failure strain is reached in any strut within the RVE. However, future research should investigate the potential impact of parent material damage and the effects of interactions between multiple types and sizes of defects. Another area for future work is investigating the dynamic response of the metamaterials under different loading conditions, including impact and vibration. Understanding the dynamic behaviour of the metamaterials will be critical in their application to various engineering fields, including aerospace and defence.

In Chapter 5, a data-driven methodology was developed to use manufacturing defects (studied in Chapter 4) to our advantage by tuning the disorderliness in the metamaterials. This methodology changes the failure mechanisms from single shear band to shear band branching of the structure and enhances the ductility. However, one area for further exploration is optimising the mechanical properties of the metamaterials using different types of imperfections and loading conditions. In addition, the data-driven methodology developed in this study can be further refined and extended to design new metamaterials such as Kagame, Diamond and Triangular with enhanced properties. Future work needs to be conducted to reveal the underlying mechanisms via comparing different type of lattice structures. In machine learning, one also had to explore the different loss functions used in this work to evaluate the test data sets. The idea behind evaluating the

test data set under different assumptions is still blurred and needs further exploration.

In Chapter 6, a damage model was implemented for investigation of the creep behavior of the Inconel 718 metamaterial at elevated temperatures. The investigation of creep behavior at even higher temperatures is also a promising area for future work. This would provide further insight into the effects of microstructure on the creep resistance of the metamaterial and help to optimise their performance in high-temperature applications. Additionally, the work does not address important topics, such as the impact of LPBF building direction and residual stress on creep testing. Future work needs to be conducted by undertaking more creep testing and modelling with different parameters (load, temperature, lattice type) to allow a better understanding of the creep behaviour of metamaterials. The study of the metamaterials behavior under different environmental conditions, such as exposure to corrosive or extreme temperatures, could also be explored. This could provide insight into the durability and longevity of the metamaterials in real-world applications.

Overall, the development of mechanical metamaterials using AM technologies has shown great promise in advancing materials engineering. However, there are still many avenues for future research and development in this area, and the results of this study provide a solid foundation for further exploration and innovation in the field.

Bibliography

[1] M. Ali, U. Sajjad, I. Hussain, N. Abbas, H. M. Ali, W.-M. Yan, and C.-C. Wang, "On the assessment of the mechanical properties of additively manufactured lattice structures," *Engineering Analysis with Boundary Elements*, vol. 142, pp. 93–116, 2022.

[2] X. Yu, J. Zhou, H. Liang, Z. Jiang, and L. Wu, "Mechanical metamaterials associated with stiffness, rigidity and compressibility: A brief review," *Progress in Materials Science*, vol. 94, pp. 114–173, 2018.

[3] J. Christensen, M. Kadic, O. Kraft, and M. Wegener, "Vibrant times for mechanical metamaterials," 2015.

[4] A. Challapalli and G. Li, "Machine learning assisted design of new lattice core for sandwich structures with superior load carrying capacity," *Scientific Reports*, 2021.

[5] Gibson LJ; Ashby MF, *Cellular solids: structure and properties. 2nd ed.* 1997.

[6] C. Tekolu, J. W. Hutchinson, and T. Pardoen, "On localization and void coalescence as a precursor to ductile fracture," *Philosophical Transactions of the Royal Society A: Mathematical, Physical and Engineering Sciences*, 2015.

[7] E. Filippidi, D. G. DeMartini, P. M. De Molina, E. W. Danner, J. Kim, M. E. Helgeson, J. H. Waite, and M. T. Valentine, "The

microscopic network structure of mussel (Mytilus) adhesive plaques," *Journal of the Royal Society Interface*, 2015.

[8] M. C. Fernandes, J. Aizenberg, J. C. Weaver, and K. Bertoldi, "Mechanically robust lattices inspired by deep-sea glass sponges," *Nature Materials*, 2021.

[9] A. M. Torres, A. A. Trikanad, C. A. Aubin, F. M. Lambers, M. Luna, C. M. Rimnac, P. Zavattieri, and C. J. Hernandez, "Bone-inspired microarchitectures achieve enhanced fatigue life," *Proceedings of the National Academy of Sciences of the United States of America*, 2019.

[10] P. J. Bishop, S. A. Hocknull, C. J. Clemente, J. R. Hutchinson, A. A. Farke, B. R. Beck, R. S. Barrett, and D. G. Lloyd, "Cancellous bone and theropod dinosaur locomotion. Part I-an examination of cancellous bone architecture in the hindlimb bones of theropods," *PeerJ*, 2019.

[11] T. Yang, H. Chen, Z. Jia, Z. Deng, L. Chen, E. M. Peterman, J. C. Weaver, and L. Li, "A damage-tolerant, dual-scale, single-crystalline microlattice in the knobby starfish, Protoreaster nodosus," *Science*, vol. 375, no. 6581, pp. 647–652, 2022.

[12] D. A. Egmond, B. Yu, S. Choukir, S. Fu, G. H. , C.V. Singh, and B. Hatton, "The benefits of structural disorder in natural cellular solids," *Applied Physics (physics.app-ph); Materials Science (cond-mat.mtrl-sci)*, 2021.

[13] H. Gu, M. Pavier, and A. Shterenlikht, "Experimental study of modulus, strength and toughness of 2D triangular lattices," *International Journal of Solids and Structures*, vol. 152-153, pp. 207–216, nov 2018.

[14] A. Bhuwal, T. Liu, I. Ashcroft, and W. Sun, "Localization and coalescence of imperfect planar FCC truss lattice metamaterials under multiaxial loadings," *Mechanics of Materials*, vol. 160, p. 103996, sep 2021.

[15] Z. Xu, C. J. Hyde, C. Tuck, and A. T. Clare, "Creep behaviour of inconel 718 processed by laser powder bed fusion," *Journal of Materials Processing Technology*, 2018.

[16] Z. Xu, J. W. Murray, C. J. Hyde, and A. T. Clare, "Effect of post processing on the creep performance of laser powder bed fused Inconel 718," *Additive Manufacturing*, 2018.

[17] T. H. Hyde, B. S. Ali, and W. Sun, "Analysis and design of a small, two-bar creep test specimen," *Journal of Engineering Materials and Technology*, 2013.

[18] B. S. Ali, T. H. Hyde, and W. Sun, "Small Two-Bar Specimen Creep Testing of Grade P91 Steel at 650°C," *High Temperature Materials and Processes*, 2016.

[19] M. Santorinaios, W. Brooks, C. J. Sutcliffe, and R. A. Mines, "Crush behaviour of open cellular lattice structures manufactured using selective laser melting," in *WIT Transactions on the Built Environment*, 2006.

[20] M. K. Thompson, G. Moroni, T. Vaneker, G. Fadel, R. I. Campbell, I. Gibson, A. Bernard, J. Schulz, P. Graf, B. Ahuja, and F. Martina, "Design for Additive Manufacturing: Trends, opportunities, considerations, and constraints," *CIRP Annals - Manufacturing Technology*, 2016.

[21] R. R. Boyer, "An overview on the use of titanium in the aerospace industry," *Materials Science and Engineering A*, 1996.

[22] R. Kuziak, R. Kawalla, and S. Waengler, "Advanced high strength steels for automotive industry: A review," 2008.

[23] T. Kim, H. P. Hodson, and T. J. Lu, "Fluid-flow and endwall heat-transfer characteristics of an ultralight lattice-frame material," *International Journal of Heat and Mass Transfer*, 2004.

[24] J. Wang, T. J. Lu, J. Woodhouse, R. S. Langley, and J. Evans, "Sound transmission through lightweight double-leaf partitions: Theoretical modelling," *Journal of Sound and Vibration*, 2005.

[25] T. Liu, Z. C. Deng, and T. J. Lu, "Minimum weights of pressurized hollow sandwich cylinders with ultralight cellular cores," *International Journal of Solids and Structures*, 2007.

[26] W. Yang, Z. Yue, and B. Xu, "A hybrid elastomeric foam-core/solid-shell spherical structure for enhanced energy absorption performance," *International Journal of Solids and Structures*, 2016.

[27] W. Yang, Q. Liu, Z. Gao, Z. Yue, and B. Xu, "Theoretical search for heterogeneously architected 2D structures," *Proceedings of the National Academy of Sciences of the United States of America*, 2018.

[28] J. Zhang, Y. Liu, B. B. Babamiri, Y. Zhou, M. Dargusch, K. Hazeli, and M.-X. Zhang, "Enhancing specific energy absorption of additively manufactured titanium lattice structures through simultaneous manipulation of architecture and constituent material," *Additive Manufacturing*, vol. 55, p. 102887, 2022.

[29] J. Yang, X. Chen, Y. Sun, J. Zhang, C. Feng, Y. Wang, K. Wang,

and L. Bai, "Compressive properties of bidirectionally graded lattice structures," *Materials & Design*, vol. 218, p. 110683, 2022.

[30] D. S. Nguyen and F. Vignat, "A method to generate lattice structure for Additive Manufacturing," in *IEEE International Conference on Industrial Engineering and Engineering Management*, 2016.

[31] A. Jam, A. du Plessis, C. Lora, S. Raghavendra, M. Pellizzari, and M. Benedetti, "Manufacturability of lattice structures fabricated by laser powder bed fusion: A novel biomedical application of the beta ti-21s alloy," *Additive Manufacturing*, vol. 50, p. 102556, 2022.

[32] M. Wong, I. Owen, C. J. Sutcliffe, and A. Puri, "Convective heat transfer and pressure losses across novel heat sinks fabricated by Selective Laser Melting," *International Journal of Heat and Mass Transfer*, 2009.

[33] Y. Shen, S. McKown, S. Tsopanos, C. J. Sutcliffe, R. A. Mines, and W. J. Cantwell, "The mechanical properties of sandwich structures based on metal lattice architectures," *Journal of Sandwich Structures and Materials*, 2010.

[34] D. Shidid, M. Leary, P. Choong, and M. Brandt, "Just-in-time design and additive manufacture of patient-specific medical implants," in *Physics Procedia*, 2016.

[35] E. Alabort, D. Barba, and R. C. Reed, "Design of metallic bone by additive manufacturing," *Scripta Materialia*, 2019.

[36] A. Zargarian, M. Esfahanian, J. Kadkhodapour, S. Ziaei-Rad, and D. Zamani, "On the fatigue behavior of additive manufactured lattice structures," *Theoretical and Applied Fracture Mechanics*, 2019.

[37] S. M. Ahmadi, G. Campoli, S. Amin Yavari, B. Sajadi, R. Wauthle, J. Schrooten, H. Weinans, and A. A. Zadpoor, "Mechanical behavior of regular open-cell porous biomaterials made of diamond lattice unit cells," *Journal of the Mechanical Behavior of Biomedical Materials*, 2014.

[38] R. T. Wu, T. W. Liu, M. R. Jahanshahi, and F. Semperlotti, "Design of one-dimensional acoustic metamaterials using machine learning and cell concatenation," *Structural and Multidisciplinary Optimization*, 2021.

[39] Y. Wang and O. Sigmund, "Quasiperiodic mechanical metamaterials with extreme isotropic stiffness," *Extreme Mechanics Letters*, 2020.

[40] Z. Vangelatos, K. Komvopoulos, and C. P. Grigoropoulos, "Regulating the mechanical behavior of metamaterial microlattices by tactical structure modification," *Journal of the Mechanics and Physics of Solids*, 2020.

[41] J. K. Wilt, C. Yang, and G. X. Gu, "Accelerating Auxetic Metamaterial Design with Deep Learning," *Advanced Engineering Materials*, 2020.

[42] H. Yazdani Sarvestani, A. H. Akbarzadeh, A. Mirbolghasemi, and K. Hermenean, "3D printed meta-sandwich structures: Failure mechanism, energy absorption and multi-hit capability," *Materials and Design*, 2018.

[43] M. Mohsenizadeh, F. Gasbarri, M. Munther, A. Beheshti, and K. Davami, "Additively-manufactured lightweight Metamaterials for energy absorption," *Materials and Design*, 2018.

[44] M. Naghavi Zadeh, F. Alijani, X. Chen, I. Dayyani, M. Yasaee,

M. J. Mirzaali, and A. A. Zadpoor, "Dynamic characterization of 3D printed mechanical metamaterials with tunable elastic properties," *Applied Physics Letters*, 2021.

[45] Y. Chen, L. Ye, Y. X. Zhang, and K. Fu, "Compression behaviours of 3D-printed CF/PA metamaterials: Experiment and modelling," *International Journal of Mechanical Sciences*, 2021.

[46] P. Sengsri and S. Kaewunruen, "Local failure modes and critical buckling loads of a meta-functional auxetic sandwich core for composite bridge bearing applications," *Applied Sciences (Switzerland)*, 2021.

[47] W. Guo, Y. Huang, R. O. Ritchie, and S. Yin, "Dissipative dual-phase mechanical metamaterial composites via architectural design," *Extreme Mechanics Letters*, 2021.

[48] S. Yin, W. Guo, H. Wang, Y. Huang, R. Yang, Z. Hu, D. Chen, J. Xu, and R. O. Ritchie, "Strong and Tough Bioinspired Additive-Manufactured Dual-Phase Mechanical Metamaterial Composites," *Journal of the Mechanics and Physics of Solids*, 2021.

[49] S. Sun, D. Zhang, S. Palanisamy, Q. Liu, and M. S. Dargusch, "Mechanical properties and deformation mechanisms of martensitic Ti6Al4V alloy processed by laser powder bed fusion and water quenching," *Materials Science and Engineering A*, 2022.

[50] T. Bückmann, M. Kadic, N. Stenger, M. Thiel, and M. Wegener, "On the feasibility of pentamode mechanical metamaterials," *Metamaterials '2012: The Sixth International Congress on Advanced Electromagnetic Materials in Microwaves and Optics*, 2012.

[51] G. F. Méjica and A. D. Lantada, "Comparative study of potential

pentamodal metamaterials inspired by Bravais lattices," *Smart Materials and Structures*, 2013.

[52] R. Hedayati, N. Ghavidelnia, M. Sadighi, and M. Bodaghi, "Improving the accuracy of analytical relationships for mechanical properties of permeable metamaterials," *Applied Sciences (Switzerland)*, 2021.

[53] T. Xue, T. J. Wallin, Y. Menguc, S. Adriaenssens, and M. Chiaramonte, "Machine learning generative models for automatic design of multi-material 3D printed composite solids," *Extreme Mechanics Letters*, 2020.

[54] Y. Zheng, Y. Wang, X. Lu, Z. Liao, and J. Qu, "Evolutionary topology optimization for mechanical metamaterials with auxetic property," *International Journal of Mechanical Sciences*, 2020.

[55] H. M. Kolken and A. A. Zadpoor, "Auxetic mechanical metamaterials," 2017.

[56] M. Ye, L. Gao, F. Wang, and H. Li, "A novel design method for energy absorption property of chiral mechanical metamaterials," *Materials*, 2021.

[57] T. Chatterjee, S. Chakraborty, S. Goswami, S. Adhikari, and M. I. Friswell, "Robust topological designs for extreme metamaterial micro-structures," *Scientific Reports*, 2021.

[58] W. Hu, Z. Ren, Z. Wan, D. Qi, X. Cao, Z. Li, W. Wu, R. Tao, and Y. Li, "Deformation behavior and band gap switching function of 4D printed multi-stable metamaterials," *Materials and Design*, 2021.

[59] Z. Shi, E. Tsymbalov, M. Dao, S. Suresh, A. Shapeev, and J. Li, "Deep elastic strain engineering of bandgap through machine learn-

ing," *Proceedings of the National Academy of Sciences of the United States of America*, 2019.

[60] S. M. Montgomery, S. Wu, X. Kuang, C. D. Armstrong, C. Zemelka, Q. Ze, R. Zhang, R. Zhao, and H. J. Qi, "Magneto-Mechanical Metamaterials with Widely Tunable Mechanical Properties and Acoustic Bandgaps," *Advanced Functional Materials*, 2021.

[61] O. Weeger, B. Narayanan, and M. L. Dunn, "Isogeometric shape optimization of nonlinear, curved 3D beams and beam structures," *Computer Methods in Applied Mechanics and Engineering*, 2019.

[62] W. Wu, P. Liu, and Z. Kang, "A novel mechanical metamaterial with simultaneous stretching- and compression-expanding property," *Materials and Design*, 2021.

[63] K. Bertoldi, V. Vitelli, J. Christensen, and M. Van Hecke, "Flexible mechanical metamaterials," 2017.

[64] E. G. Karpov and D. Saha, "Collective elastic properties of mechanical metamaterials," *Extreme Mechanics Letters*, 2022.

[65] M. J. Mirzaali, R. Hedayati, P. Vena, L. Vergani, M. Strano, and A. A. Zadpoor, "Rational design of soft mechanical metamaterials: Independent tailoring of elastic properties with randomness," *Applied Physics Letters*, 2017.

[66] A. A. Sabouni-Zawadzka, "Extreme mechanical properties of regular tensegrity unit cells in 3D lattice metamaterials," *Materials*, 2020.

[67] M. K. Budzik, M. Wolfahrt, P. Reis, M. Kozłowski, J. Sena-Cruz, L. Papadakis, M. Nasr Saleh, K. V. Machalicka, S. Teixeira de Freitas, and A. P. Vassilopoulos, "Testing mechanical performance of

adhesively bonded composite joints in engineering applications: an overview," 2022.

[68] L. Ren, W. Wu, L. Ren, Z. Song, Q. Liu, B. Li, Q. Wu, and X. Zhou, "3D Printing of Auxetic Metamaterials with High-Temperature and Programmable Mechanical Properties," *Advanced Materials Technologies*, 2022.

[69] K. Mnasri, A. Khrabustovskyi, C. Stohrer, M. Plum, and C. Rockstuhl, "Beyond local effective material properties for metamaterials," *Physical Review B*, 2018.

[70] C. Helgert, C. Rockstuhl, C. Etrich, C. Menzel, E.-B. Kley, A. Tünnermann, F. Lederer, and T. Pertsch, "Effective properties of amorphous metamaterials," *Physical Review B*, 2009.

[71] J. Shi, Z. Li, D. K. Sang, Y. Xiang, J. Li, S. Zhang, and H. Zhang, "THz photonics in two dimensional materials and metamaterials: Properties, devices and prospects," 2018.

[72] F. Bilotti and L. Sevgi, "Metamaterials: Definitions, properties, applications, and FDTD-based modeling and simulation (Invited paper)," 2012.

[73] V. Fokin, M. Ambati, C. Sun, and X. Zhang, "Method for retrieving effective properties of locally resonant acoustic metamaterials," *Physical Review B - Condensed Matter and Materials Physics*, 2007.

[74] A. Ibrahim, H. F. Abutarboush, A. W. Mohamed, M. Fouad, and E. S. M. El-Kenawy, "An optimized ensemble model for prediction the bandwidth of metamaterial antenna," *Computers, Materials and Continua*, 2022.

[75] E. Ashalley, C. P. Ma, Y. S. Zhu, H. X. Xu, P. Yu, and Z. M. Wang, "Recent Progress in Chiral Absorptive Metamaterials," *Journal of Electronic Science and Technology*, 2021.

[76] H. T. Kollmann, D. W. Abueidda, S. Koric, E. Guleryuz, and N. A. Sobh, "Deep learning for topology optimization of 2D metamaterials," *Materials and Design*, 2020.

[77] M. A. Bessa, P. Glowacki, and M. Houlder, "Bayesian Machine Learning in Metamaterial Design: Fragile Becomes Supercompressible," *Advanced Materials*, 2019.

[78] Y. Chang, H. Wang, and Q. Dong, "Machine learning-based inverse design of auxetic metamaterial with zero Poisson's ratio," *Materials Today Communications*, 2022.

[79] G. Moon, J. ryul Choi, C. Lee, Y. Oh, K. H. Kim, and D. Kim, "Machine learning-based design of meta-plasmonic biosensors with negative index metamaterials," *Biosensors and Bioelectronics*, 2020.

[80] W. Ma, F. Cheng, and Y. Liu, "Deep-Learning-Enabled On-Demand Design of Chiral Metamaterials," *ACS Nano*, 2018.

[81] H. Wang, S. H. Xiao, and C. Zhang, "Novel Planar Auxetic Metamaterial Perforated with Orthogonally Aligned Oval-Shaped Holes and Machine Learning Solutions," *Advanced Engineering Materials*, 2021.

[82] B. Cheng, J. Du, and Y. Yao, "Machine learning methods to assist structure design and optimization of dual darrieus wind turbines," *Energy*, vol. 244, p. 122643, 2022.

[83] R. Zhu, J. Wang, J. Jiang, C. Xu, C. Liu, Y. Jia, S. Sui, Z. Zhang, T. Liu, Z. Chu, J. Wang, T. J. Cui, and S. Qu, "Machine-learning-empowered multispectral metafilm with reduced radar cross section,

low infrared emissivity, and visible transparency," *Photonics Research*, 2022.

[84] H. E. Romeijn, F. Schoen, and A. Fallis, *Handbook of Global Optimization*. 1995.

[85] S. H. Brooks, "A Discussion of Random Methods for Seeking Maxima," *Operations Research*, 1958.

[86] R. S. Anderssen and P. Bloomfield, "Properties of the random search in global optimization," *Journal of Optimization Theory and Applications*, 1975.

[87] A. Abakuks, "THEORY OF GLOBAL RANDOM SEARCH," *Bulletin of the London Mathematical Society*, 1992.

[88] Z. B. Zabinsky and R. L. Smith, "Pure adaptive search in global optimization," *Mathematical Programming*, 1992.

[89] D. B. Fogel, *Artificial Intelligence through Simulated Evolution*, pp. 227–296. 1998.

[90] J. Koza, *Genetic programming: on the programming of computers by means of natural selection*. 1992.

[91] R. Storn and K. Price, "Differential Evolution - A Simple and Efficient Heuristic for Global Optimization over Continuous Spaces," *Journal of Global Optimization*, 1997.

[92] S. Kirkpatrick, C. D. Gelatt, and M. P. Vecchi, "Optimization by simulated annealing," *Science*, 1983.

[93] F. Glover, "HEURISTICS FOR INTEGER PROGRAMMING USING SURROGATE CONSTRAINTS," *Decision Sciences*, 1977.

[94] M. Dorigo, V. Maniezzo, and A. Colorni, "Ant system: Optimization by a colony of cooperating agents," *IEEE Transactions on Systems, Man, and Cybernetics, Part B: Cybernetics*, 1996.

[95] Z. W. Geem, J. H. Kim, and G. V. Loganathan, "A New Heuristic Optimization Algorithm: Harmony Search," *Simulation*, 2001.

[96] J. J. Lewandowski and M. Seifi, "Metal Additive Manufacturing: A Review of Mechanical Properties," 2016.

[97] T. Liu, Z. C. Deng, and T. J. Lu, "Design optimization of truss-cored sandwiches with homogenization," *International Journal of Solids and Structures*, 2006.

[98] M. F. Ashby and B. F. Dyson, "CREEP DAMAGE MECHANICS AND MICROMECHANISMS.," 1984.

[99] Z. L. Kowalewski, D. R. Hayhurst, and B. F. Dyson, "Mechanisms-based creep constitutive equations for an aluminium alloy," *The Journal of Strain Analysis for Engineering Design*, 1994.

[100] L. M. Kachanov, "Time of rupture process under creep conditions," *Isv. Akad. Nauk. SSR. Otd Tekh. Nauk.*, 1958.

[101] E. Andrews, L. Gibson, and M. Ashby, "The creep of cellular solids," *Acta Materialia*, 1999.

[102] E. W. Andrews, L. J. Gibson, and M. F. Ashby, "Overview No. 132: The creep of cellular solids," *Acta Materialia*, vol. 47, no. 10, pp. 2853–2863, 1999.

[103] T.-J. Chen and J.-S. Huang, "Creep-buckling of open-cell foams," *Acta Materialia*, vol. 57, no. 5, pp. 1497–1503, 2009.

[104] Z. G. Fan, C. Q. Chen, and T. J. Lu, "Multiaxial creep of low density open-cell foams," *Materials Science and Engineering A*, vol. 540, pp. 83–88, 2012.

[105] Y. Boonyongmaneerat and D. C. Dunand, "Effects of strut geometry and pore fraction on creep properties of cellular materials," *Acta Materialia*, 2009.

[106] J. Y. Lin and J. S. Huang, "Creep of hexagonal honeycombs with Plateau borders," *Composite Structures*, 2005.

[107] T. J. Chen and J. S. Huang, "Creep-rupturing of open-cell foams," *Acta Materialia*, 2008.

[108] H. Meng, D. Chronopoulos, and A. T. Fabro, "Numerical simulation data for the dynamic properties of rainbow metamaterials," *Data in Brief*, 2020.

[109] S. Bang, J. Kim, G. Yoon, T. Tanaka, and J. Rho, "Recent advances in tunable and reconfigurable metamaterials," 2018.

[110] M. Kim, S. Park, M. Shin, and Y. Jeong, "Noise improvement of air conditioning accumulator using acoustic metamaterials," in *Proceedings of 2020 International Congress on Noise Control Engineering, INTER-NOISE 2020*, 2020.

[111] M. Ye, L. Gao, and H. Li, "A design framework for gradually stiffer mechanical metamaterial induced by negative Poisson's ratio property," *Materials and Design*, 2020.

[112] D. W. Rosen, "Computer-Aided Design for Additive Manufacturing of Cellular Structures," *Computer-Aided Design and Applications*, 2007.

[113] A. Panesar, M. Abdi, D. Hickman, and I. Ashcroft, "Strategies for functionally graded lattice structures derived using topology optimisation for Additive Manufacturing," *Additive Manufacturing*, 2018.

[114] I. Maskery and I. A. Ashcroft, "The deformation and elastic anisotropy of a new gyroid-based honeycomb made by laser sintering," *Additive Manufacturing*, 2020.

[115] I. Maskery, A. O. Aremu, L. Parry, R. D. Wildman, C. J. Tuck, and I. A. Ashcroft, "Effective design and simulation of surface-based lattice structures featuring volume fraction and cell type grading," *Materials and Design*, 2018.

[116] P. Köhnen, C. Haase, J. Bültmann, S. Ziegler, J. H. Schleifenbaum, and W. Bleck, "Mechanical properties and deformation behavior of additively manufactured lattice structures of stainless steel," *Materials and Design*, 2018.

[117] A. Vigliotti, V. S. Deshpande, and D. Pasini, "Non linear constitutive models for lattice materials," *Journal of the Mechanics and Physics of Solids*, 2014.

[118] X. Geng, Y. Lu, C. Liu, W. Li, and Z. Yue, "Fracture characteristic analysis of cellular lattice structures under tensile load," *International Journal of Solids and Structures*, 2019.

[119] H. Alsalla, L. Hao, and C. Smith, "Fracture toughness and tensile strength of 316L stainless steel cellular lattice structures manufactured using the selective laser melting technique," *Materials Science and Engineering A*, 2016.

[120] B. Vayre, F. Vignat, and F. Villeneuve, "Metallic additive manufac-

turing: State-of-the-art review and prospects," *Mechanics and Industry*, 2012.

[121] Z. S. Bagheri, D. Melancon, L. Liu, R. B. Johnston, and D. Pasini, "Compensation strategy to reduce geometry and mechanics mismatches in porous biomaterials built with Selective Laser Melting," *Journal of the Mechanical Behavior of Biomedical Materials*, 2017.

[122] S. Arabnejad and D. Pasini, "Mechanical properties of lattice materials via asymptotic homogenization and comparison with alternative homogenization methods," *International Journal of Mechanical Sciences*, 2013.

[123] A. Vigliotti and D. Pasini, "Stiffness and strength of tridimensional periodic lattices," *Computer Methods in Applied Mechanics and Engineering*, 2012.

[124] L. Liu, P. Kamm, F. García-Moreno, J. Banhart, and D. Pasini, "Elastic and failure response of imperfect three-dimensional metallic lattices: the role of geometric defects induced by Selective Laser Melting," *Journal of the Mechanics and Physics of Solids*, 2017.

[125] S. Wehmeyer, F. W. Zok, C. Eberl, P. Gumbsch, N. Cohen, R. M. McMeeking, and M. R. Begley, "Post-buckling and dynamic response of angled struts in elastic lattices," *Journal of the Mechanics and Physics of Solids*, vol. 133, p. 103693, 2019.

[126] T. Tancogne-Dejean, A. B. Spierings, and D. Mohr, "Additively-manufactured metallic micro-lattice materials for high specific energy absorption under static and dynamic loading," *Acta Materialia*, 2016.

[127] G. Campoli, M. S. Borleffs, S. Amin Yavari, R. Wauthle, H. Weinans, and A. A. Zadpoor, "Mechanical properties of open-cell metallic

biomaterials manufactured using additive manufacturing," *Materials and Design*, 2013.

[128] I. Barsoum and J. Faleskog, "Micromechanical analysis on the influence of the Lode parameter on void growth and coalescence," *International Journal of Solids and Structures*, 2011.

[129] M. Dunand and D. Mohr, "Effect of Lode parameter on plastic flow localization after proportional loading at low stress triaxialities," *Journal of the Mechanics and Physics of Solids*, 2014.

[130] F. Scheyvaerts, P. R. Onck, C. Tekoğlu, and T. Pardoen, "The growth and coalescence of ellipsoidal voids in plane strain under combined shear and tension," *Journal of the Mechanics and Physics of Solids*, 2011.

[131] V. Tvergaard, "Ductile fracture by cavity nucleation between larger voids," *Journal of the Mechanics and Physics of Solids*, 1982.

[132] V. Tvergaard, "Shear deformation of voids with contact modelled by internal pressure," *International Journal of Mechanical Sciences*, 2008.

[133] P. M. Anderson, N. A. Fleck, and K. L. Johnson, "Localization of plastic deformation in shear due to microcracks," *Journal of the Mechanics and Physics of Solids*, 1990.

[134] I. Echeta, X. Feng, B. Dutton, R. Leach, and S. Piano, "Review of defects in lattice structures manufactured by powder bed fusion," *International Journal of Advanced Manufacturing Technology*, 2020.

[135] B. Zhang, Y. Li, and Q. Bai, "Defect Formation Mechanisms in Selective Laser Melting: A Review," 2017.

[136] D. Melancon, Z. S. Bagheri, R. B. Johnston, L. Liu, M. Tanzer, and D. Pasini, "Mechanical characterization of structurally porous biomaterials built via additive manufacturing: experiments, predictive models, and design maps for load-bearing bone replacement implants," *Acta Biomaterialia*, 2017.

[137] N. E. Romijn and N. A. Fleck, "The fracture toughness of planar lattices: Imperfection sensitivity," *Journal of the Mechanics and Physics of Solids*, 2007.

[138] B. Su, Z. Zhou, Z. Wang, Z. Li, and X. Shu, "Effect of defects on creep behavior of cellular materials," *Materials Letters*, 2014.

[139] C. Chen, T. J. Lu, and N. A. Fleck, "Effect of inclusions and holes on the stiffness and strength of honeycombs," *International Journal of Mechanical Sciences*, 2001.

[140] B. Lozanovski, M. Leary, P. Tran, D. Shidid, M. Qian, P. Choong, and M. Brandt, "Computational modelling of strut defects in SLM manufactured lattice structures," *Materials and Design*, 2019.

[141] S. Arabnejad, R. Burnett Johnston, J. A. Pura, B. Singh, M. Tanzer, and D. Pasini, "High-strength porous biomaterials for bone replacement: A strategy to assess the interplay between cell morphology, mechanical properties, bone ingrowth and manufacturing constraints," *Acta Biomaterialia*, 2016.

[142] R. C. Lin, D. Steglich, W. Brocks, and J. Betten, "Performing RVE calculations under constant stress triaxiality for monotonous and cyclic loading," *International Journal for Numerical Methods in Engineering*, 2006.

[143] ABAQUS, "Abaqus 6.14," *Abaqus 6.14 Analysis User's Guide*, 2014.

[144] W. Wu, J. Owino, A. Al-Ostaz, and L. Cai, "Applying Periodic Boundary Conditions in Finite Element Analysis," *Simulia Community Conference*, 2014.

[145] R. Hill, "A theory of the yielding and plastic flow of anisotropic metals," *Proceedings of the Royal Society of London. Series A. Mathematical and Physical Sciences*, vol. 193, no. 1033, pp. 281–297, 1948.

[146] D. Mohr, "Mechanism-based multi-surface plasticity model for ideal truss lattice materials," *International Journal of Solids and Structures*, 2005.

[147] V. S. Deshpande, M. F. Ashby, and N. A. Fleck, "Foam topology: Bending versus stretching dominated architectures," *Acta Materialia*, 2001.

[148] I. Gibson, D. W. Rosen, and B. Stucker, *Additive manufacturing technologies: Rapid prototyping to direct digital manufacturing*. 2010.

[149] H. C. Tankasala, V. S. Deshpande, and N. A. Fleck, "Tensile response of elastoplastic lattices at finite strain," *Journal of the Mechanics and Physics of Solids*, 2017.

[150] L. C. Reis, P. A. Prates, M. C. Oliveira, A. D. Santos, and J. V. Fernandes, "Anisotropy and plastic flow in the circular bulge test," *International Journal of Mechanical Sciences*, 2017.

[151] I. Rosenthal, A. Stern, and N. Frage, "Microstructure and Mechanical Properties of AlSi10Mg Parts Produced by the Laser Beam Additive Manufacturing (AM) Technology," *Metallography, Microstructure, and Analysis*, 2014.

[152] N. Cohen and K. Bhattacharya, "A numerical study of the electromechanical response of liquid metal embedded elastomers," *In-*

ternational Journal of Non-Linear Mechanics, vol. 108, no. October 2018, pp. 81–86, 2019.

[153] Z. Qin and M. J. Buehler, "Impact tolerance in mussel thread networks by heterogeneous material distribution," *Nature Communications*, 2013.

[154] P. Van Liedekerke, E. Tijskens, H. Ramon, P. Ghysels, G. Samaey, and D. Roose, "Particle-based model to simulate the micromechanics of biological cells," *Physical Review E - Statistical, Nonlinear, and Soft Matter Physics*, 2010.

[155] T. M. Ryan and C. N. Shaw, "Trabecular bone microstructure scales allometrically in the primate humerus and femur," *Proceedings of the Royal Society B: Biological Sciences*, 2013.

[156] K. Ando and H. Onda, "Mechanism for deformation of wood as a honeycomb structure I: Effect of anatomy on the initial deformation process during radial compression," *Journal of Wood Science*, 1999.

[157] H. S. Gupta, J. Seto, W. Wagermaier, P. Zaslansky, P. Boesecke, and P. Fratzl, "Cooperative deformation of mineral and collagen in bone at the nanoscale," *Proceedings of the National Academy of Sciences of the United States of America*, 2006.

[158] X. Zheng, H. Lee, T. H. Weisgraber, M. Shusteff, J. DeOtte, E. B. Duoss, J. D. Kuntz, M. M. Biener, Q. Ge, J. A. Jackson, S. O. Kucheyev, N. X. Fang, and C. M. Spadaccini, "Ultralight, ultrastiff mechanical metamaterials," *Science*, 2014.

[159] T. A. Schaedler, A. J. Jacobsen, A. Torrents, A. E. Sorensen, J. Lian, J. R. Greer, L. Valdevit, and W. B. Carter, "Ultralight metallic microlattices," *Science*, 2011.

[160] P. Fratzl, J. W. C. Dunlop, and R. Weinkamer, *Materials Design Inspired by Nature: Function Through Inner Architecture*. 2013.

[161] Z. Jia, F. Liu, X. Jiang, and L. Wang, "Engineering lattice metamaterials for extreme property, programmability, and multifunctionality," 2020.

[162] T. Liu, Z. C. Deng, and T. J. Lu, "Bi-functional optimization of actively cooled, pressurized hollow sandwich cylinders with prismatic cores," *Journal of the Mechanics and Physics of Solids*, 2007.

[163] J. B. Berger, H. N. G. Wadley, and R. M. McMeeking, "Mechanical metamaterials at the theoretical limit of isotropic elastic stiffness," *Nature*, vol. 543, pp. 533–537, mar 2017.

[164] T. Tancogne-Dejean, M. Diamantopoulou, M. B. Gorji, C. Bonatti, and D. Mohr, "3D Plate-Lattices: An Emerging Class of Low-Density Metamaterial Exhibiting Optimal Isotropic Stiffness," *Advanced Materials*, 2018.

[165] C. Chen, T. J. Lu, and N. A. Fleck, "Effect of imperfections on the yielding of two-dimensional foams," *Journal of the Mechanics and Physics of Solids*, 1999.

[166] M. S. Pham, C. Liu, I. Todd, and J. Lertthanasarn, "Damage-tolerant architected materials inspired by crystal microstructure," *Nature*, vol. 565, pp. 305–311, jan 2019.

[167] C. Liu, J. Lertthanasarn, and M. S. Pham, "The origin of the boundary strengthening in polycrystal-inspired architected materials," *Nature Communications*, 2021.

[168] R. M. Latture, M. R. Begley, and F. W. Zok, "Design and mechan-

ical properties of elastically isotropic trusses," *Journal of Materials Research*, 2018.

[169] M. C. Messner, "Optimal lattice-structured materials," *Journal of the Mechanics and Physics of Solids*, 2016.

[170] O. Ibragimova, A. Brahme, W. Muhammad, J. Lévesque, and K. Inal, "A new ANN based crystal plasticity model for FCC materials and its application to non-monotonic strain paths," *International Journal of Plasticity*, 2021.

[171] D. Goldberg, "Genetic algorithms in optimization, search and machine learning," *Addison Wesley*, 1988.

[172] A. R. Conn, N. Gould, and P. L. Toint, "A globally convergent Lagrangian barrier algorithm for optimization with general inequality constraints and simple bounds," *Mathematics of Computation*, 1997.

[173] B. Chopard and M. Tomassini, "Particle swarm optimization," in *Natural Computing Series*, 2018.

[174] L. Keviczky, R. Bars, J. Hetthéssy, and C. Bányász, "Introduction to MATLAB," 2019.

[175] Y. L. Dong and B. Pan, "A Review of Speckle Pattern Fabrication and Assessment for Digital Image Correlation," *Experimental Mechanics*, 2017.

[176] Y. Su, Z. Gao, Z. Fang, Y. Liu, Y. Wang, Q. Zhang, and S. Wu, "Theoretical analysis on performance of digital speckle pattern: uniqueness, accuracy, precision, and spatial resolution," *Optics Express*, 2019.

[177] Y. Xu, H. Zhang, B. Šavija, S. Chaves Figueiredo, and E. Schlangen, "Deformation and fracture of 3D printed disordered lattice materials: Experiments and modeling," *Materials and Design*, 2019.

[178] N. a. Fleck, "An overview of the mechanical properties of foams and periodic lattice materials," *Cellular Metals and Polymers 2004*, 2004.

[179] S. L. Sing, F. E. Wiria, and W. Y. Yeong, "Selective laser melting of lattice structures: A statistical approach to manufacturability and mechanical behavior," *Robotics and Computer-Integrated Manufacturing*, 2018.

[180] F. Wang, "Mechanical property study on rapid additive layer manufacture Hastelloy® X alloy by selective laser melting technology," *International Journal of Advanced Manufacturing Technology*, 2012.

[181] B. Song, X. Zhao, S. Li, C. Han, Q. Wei, S. Wen, J. Liu, and Y. Shi, "Differences in microstructure and properties between selective laser melting and traditional manufacturing for fabrication of metal parts: A review," 2015.

[182] R. E. Schafrik, D. D. Ward, and J. R. Groh, "Application of alloy 718 in GE aircraft engines: past, present and next five years," in *Proceedings of the International Symposium on Superalloys and Various Derivatives*, 2001.

[183] S. F. Diltemiz and S. Zhang, "Superalloys for super jobs," in *Aerospace Materials Handbook*, 2016.

[184] H. Qi, M. Azer, and A. Ritter, "Studies of standard heat treatment effects on microstructure and mechanical properties of laser net shape manufactured INCONEL 718," *Metallurgical and Materials Transactions A: Physical Metallurgy and Materials Science*, 2009.

[185] F. Liu, X. Lin, G. Yang, M. Song, J. Chen, and W. Huang, "Microstructure and residual stress of laser rapid formed Inconel 718 nickel-base superalloy," *Optics and Laser Technology*, 2011.

[186] K. N. Amato, S. M. Gaytan, L. E. Murr, E. Martinez, P. W. Shindo, J. Hernandez, S. Collins, and F. Medina, "Microstructures and mechanical behavior of Inconel 718 fabricated by selective laser melting," *Acta Materialia*, 2012.

[187] Z. Xue and J. W. Hutchinson, "A comparative study of impulse-resistant metal sandwich plates," *International Journal of Impact Engineering*, 2004.

[188] C. Bonatti and D. Mohr, "Large deformation response of additively-manufactured FCC metamaterials: From octet truss lattices towards continuous shell mesostructures," *International Journal of Plasticity*, 2017.

[189] Y. Mizokami, T. Igari, F. Kawashima, N. Sakakibara, M. Tanihira, T. Yuhara, and T. Hiroe, "Development of structural design procedure of plate-fin heat exchanger for HTGR," *Nuclear Engineering and Design*, 2013.

[190] MONKMAN F. C., "An Empirical Relationship between Rupture Life and Minimum Creep Rate in Creep-Rupture Tests," *Proc of the ASTM*, vol. 56, pp. 593–620, 1956.

[191] N. A. Fleck and X. M. Qiu, "The damage tolerance of elastic-brittle, two-dimensional isotropic lattices," *Journal of the Mechanics and Physics of Solids*, 2007.

[192] R. Firoz, S. K. Basantia, N. Khutia, H. N. Bar, S. Sivaprasad, and G. V. Murthy, "Effect of microstructural constituents on mechani-

cal properties and fracture toughness of Inconel 718 with anomalous deformation behavior at 650 °C," *Journal of Alloys and Compounds*, 2020.

[193] Y. N. Rabotnov, F. A. Leckie, and W. Prager, "Creep Problems in Structural Members," *Journal of Applied Mechanics*, 1970.

[194] T. H. Hyde, L. Xia, and A. A. Becker, "Prediction of creep failure in aeroengine materials under multi-axial stress states," *International Journal of Mechanical Sciences*, 1996.

[195] T. H. Hyde, W. Sun, and J. A. Williams, "Prediction of creep failure life of internally pressurised thick walled CrMoV pipes," *International Journal of Pressure Vessels and Piping*, 1999.

[196] W. Wen, W. Sun, and A. A. Becker, "A two-material miniature specimen test method and the associated inverse approach for high temperature applications," *Theoretical and Applied Fracture Mechanics*, 2019.

[197] M. L. Martin, J. A. Fenske, G. S. Liu, P. Sofronis, and I. M. Robertson, "On the formation and nature of quasi-cleavage fracture surfaces in hydrogen embrittled steels," *Acta Materialia*, 2011.

[198] S. P. Lynch, "A fractographic study of gaseous hydrogen embrittlement and liquid-metal embrittlement in a tempered-martensitic steel," *Acta Metallurgica*, 1984.

[199] K. Hornik, M. Stinchcombe, and H. White, "Multilayer feedforward networks are universal approximators," *Neural Networks*, 1989.

[200] M. A. Bessa, R. Bostanabad, Z. Liu, A. Hu, D. W. Apley, C. Brinson, W. Chen, and W. K. Liu, "A framework for data-driven analysis of

materials under uncertainty: Countering the curse of dimensionality," *Computer Methods in Applied Mechanics and Engineering*, 2017.

[201] M. Mozaffar, R. Bostanabad, W. Chen, K. Ehmann, J. Cao, and M. Bessa, "Deep learning predicts path-dependent plasticity," *Proceedings of the National Academy of Sciences*, vol. 116, no. 52, pp. 26414–26420, 2019.

[202] D. W. Abueidda, S. Koric, N. A. Sobh, and H. Sehitoglu, "Deep learning for plasticity and thermo-viscoplasticity," *International Journal of Plasticity*, 2021.

[203] F. Chollet, *Deep Learning mit Python und Keras: Das Praxis-Handbuch vom Entwickler der Keras-Bibliothek*. 2018.

[204] T. Moshagen, N. A. Adde, and A. N. Rajgopal, "Finding hidden-feature depending laws inside a data set and classifying it using neural network," *arXiv preprint arXiv:2101.10427*, 2021.

[205] D. P. Kingma and J. L. Ba, "Adam: A method for stochastic optimization," in *3rd International Conference on Learning Representations, ICLR 2015 - Conference Track Proceedings*, 2015.

[206] Y. E. Nesterov, "A Method of Solving a Convex Programming Problem with Convergence Rate $\mathcal{O}(1/k^2)$," *Soviet Mathematics Doklady*, 1983.

[207] J. Burgess, B. Gallagher, D. Jensen, and B. N. Levine, "MaxProp: Routing for vehicle-based disruption-tolerant networks," in *Proceedings - IEEE INFOCOM*, 2006.

Appendices

Appendix A

A.1 Results comparison - ABAQUS Standard vs. Explicit solver

For constant triaxiality, stress ratio equation for ABAQUS Standard solver can be written from Equation (4.11) as:

$$\rho = \frac{\Sigma_{11}}{\Sigma_{22}} = \text{ const } \Rightarrow \frac{\left(u_1^{N_1} - u_1^M\right)\left(\overline{W}_1 + u_1^M\right) d}{\left(u_2^{N_2} - u_2^M\right)\left(\overline{W}_2 + u_2^M\right) d} = \rho$$

$$\text{OR} \tag{A.1}$$

$$u_1^{N_1} = u_1^M + \rho \frac{\left(\overline{W}_2 + u_2^M\right)}{\left(\overline{W}_1 + u_1^M\right)} \left(u_2^{N_2} - u_2^M\right)$$

Note that above equation is independent of spring constants and $u_2^{N_2}$ is a prescribed value. For the simulation, I have taken spring constant k_i equals to $10^{-7} \times E \times W_1$ (E is parent material's Young's modulus). ABAQUS Standard calculates three unknows quantities u_1^M, u_2^M and u_2^M using MPC (multi-point constraints) user sub-routine, iteratively. Figure A.1 shows that results obtained through explicit solver are comparable with standard solver for triaxiality $T = 0.4$ and 0.66.

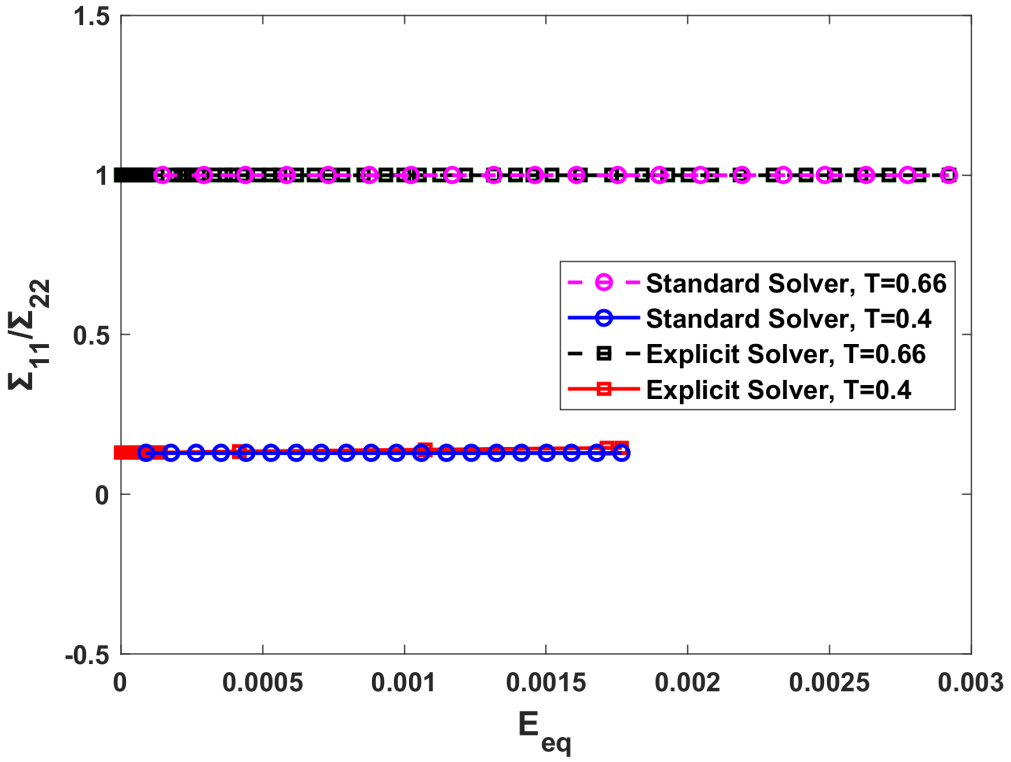

Figure A.1: Stress ratio comparison obtained via ABAQUS Standard and Explicit solvers

A.2 Continuum level FEA modelling of beam elements

The nodal displacement vectors were extracted from ABAQUS and these displacement vectors have been used as input for 2D triangular solid elements. Then strains have been mapped using the second order Gauss-Quadrature method which can be expressed as:

$$\mathbf{E}^e = \mathbf{B}^e \mathbf{a}^e \tag{A.2}$$

where $\mathbf{a}^e$ is nodal vector of the element subjected to displacement components u_1 and u_2, and $\mathbf{B}^e$ is derivatives of shape function given by:

$$\mathbf{B}^e = \begin{bmatrix} \frac{\partial N_1^e}{\partial x_1} & 0 & \frac{\partial N_2^e}{\partial x_1} & 0 & \cdots & \frac{\partial N_{en}^e}{\partial x_1} & 0 \\ 0 & \frac{\partial N_1^e}{\partial x_2} & 0 & \frac{\partial N_2^e}{\partial x_2} & \cdots & 0 & \frac{\partial N_{en}^e}{\partial x_2} \\ \frac{\partial N_1^e}{\partial x_2} & \frac{\partial N_1^e}{\partial x_1} & \frac{\partial N_2^e}{\partial x_2} & \frac{\partial N_2^e}{\partial x_1} & \cdots & \frac{\partial N_{en}^e}{\partial x_2} & \frac{\partial N_{en}^e}{\partial x_1} \end{bmatrix} \tag{A.3}$$

where n_{en} is the number of nodes of one element and N^e is the elemental shape function of the respective nodes. The strain components at Gauss points inside the band is used to calculate the average equivalent strain using Equation (4.31). To evaluate out of plane strain field, I have used standard mechanics approach within RVE. The relationship between the average strain of a triangular element and beam elements connected to the vertices of the triangular element can be expressed as:

$$E_{33}^e = \sum_{i=1}^{3} c_i \varepsilon_{33}^i \tag{A.4}$$

Similarly, for RVE the out of plane strain can be written as:

$$E_{33}^{RVE} = \sum_{j=1}^{N} c_j E_{33}^e \tag{A.5}$$

where c_i and c_j are volume fractions of the i^{th} beam element and the j^{th} triangular element respectively; N the total number of the triangular elements and ε_{33}^i the out of plane strain for the i^{th} beam element which can be calculated using volume conservation.

Appendix B

B.1 Artificial neural network

In recent studies, various ANN models are now being used. Among the suggested ANN types are multilayer perceptron feed-forward neural networks (FFNN), Convolutional Neural Networks (CNN), and recurrent neural networks (RNN). Each ANN model generally relates to a specific type of issue. FFNN, for example, is widely utilized in many fields and is well-known as "universal approximators" [199–201]. Compared to CNN and RNN, FFNN has a simpler architecture (only layers and neurons in hidden layers are vulnerable to modification) and is thus easier to evaluate in its diversity. The current study has employed tabular data to relate the input dataset (spatial coordinate perturbations and strut thickness variations) to the relevant output dataset (normalised macroscopic stress-strain response). As a result, an FFNN with a backpropagation algorithm was adopted in this work, as shown in Fig. B.1A and B.

B.1.1 Activation function and scaling

The rectified linear activation function (ReLU) was used in this study. ReLU has been widely used in feed-forward neural networks as an activation function [202]. In this work, the input was scaled between [-1, 1] for the spatial coordinate perturbation dataset and [0, 1] for the strut thickness

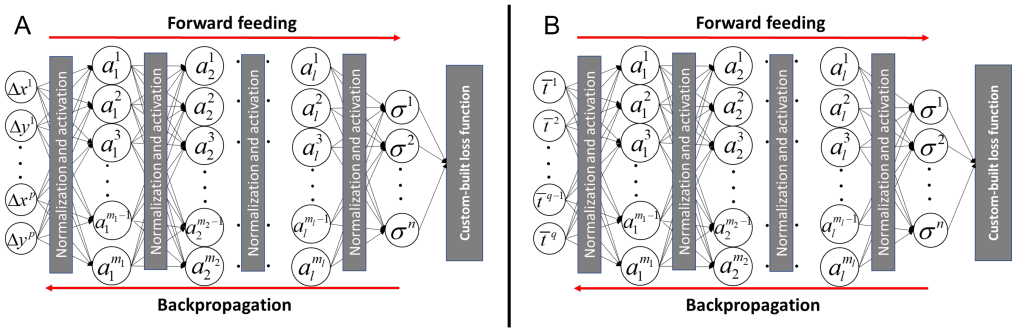

Figure B.1: An illustration of feed-forward neural network with backpropagation used in this work (A) spatial coordinate perturbation (B) strut thickness variation.

variation dataset. The ReLU activation function was found to perform better with this scaling technique. To scale the ith input data, the following mathematical transformation was applied to it:

$$\Psi^{(i)}_{\text{norm.[-1 1]}} = 2\frac{\Psi^{(i)} - \min \Psi^{(i)}}{\max \Psi^{(i)} - \min \Psi^{(i)}} - 1, \quad \Psi^{(i)}_{\text{norm.[0 1]}} = \frac{\Psi^{(i)} - \min \Psi^{(i)}}{\max \Psi^{(i)} - \min \Psi^{(i)}}, \tag{B.1}$$

where $min\Psi^{(i)}$ is the minimum and $max\Psi^{(i)}$ is the maximum value of the ith component of the input vector $\boldsymbol{\Psi}$ in the dataset.

B.1.2 Evaluation of ANN

The cost function, $J(\boldsymbol{\theta}^{[ii]}, \boldsymbol{b}_{ii})$, and loss function, $\mathcal{L}(\boldsymbol{\sigma}^m_{pred}, \boldsymbol{\sigma}^m_{true})$, are used to assess the "goodness" of the trained network. The loss function evaluates the model performance based on the real stresses, $\boldsymbol{\sigma}_{true} = [\sigma^1, \sigma^2, ..., \sigma^n]^{\mathrm{T}}_{true}$, and the predicted stresses, $\boldsymbol{\sigma}_{pred} = [\sigma^1, \sigma^2, ..., \sigma^n]^{\mathrm{T}}_{pred}$. During training, an optimisation algorithm minimises the value of the loss function by updating the weights and biases values in the "right" direction [203]. The cost function is dependent on the loss function in the following way:

$$J(\boldsymbol{\theta}^{[ii]}, \boldsymbol{b}_{ii}) = \frac{1}{h}\sum_{m=1}^{h} \mathcal{L}(\boldsymbol{\sigma}^m_{pred}, \boldsymbol{\sigma}^m_{true}) \tag{B.2}$$

where h is the number of samples in an evaluated dataset. The most commonly used loss function is the Mean Square Error (MSE) for regression analysis problems [204]. The equation is expressed as:

$$\mathcal{L}_{MSE}(\boldsymbol{\sigma}^m_{pred}, \boldsymbol{\sigma}^m_{true}) = \frac{1}{n}\sum_{k=1}^{n}\left(\sigma^k_{pred} - \sigma^k_{true}\right)^2 \tag{B.3}$$

The "logcosh" loss function for neural networks was developed to combine the advantage of the absolute error loss function of not overweighting outliers with the advantage of the mean square error of continuous derivative near the mean, which makes the last phase of learning easier, which can be expressed as:

$$\mathcal{L}_{\log\cosh}(\boldsymbol{\sigma}^m_{pred}, \boldsymbol{\sigma}^m_{true}) = \frac{1}{n}\sum_{k=1}^{n}\log(\cosh(\sigma^k_{pred} - \sigma^k_{true})) \tag{B.4}$$

As shown in Fig. B.2, numerical experiments on quasi-disordered FCC lattices have suggested that the stress data in the three groups (Zones) have significantly different variances across the QTM samples. Hence, I have proposed a custom-built loss function based on the "quantile regression loss function" to accurately predict stress-strain responses. The loss function used is given as:

$$\mathcal{L}_{custom}(\boldsymbol{\sigma}^k_{pred}, \boldsymbol{\sigma}^k_{true}) = \frac{1}{3n}\sum_{i=1}^{3}\left[\sum_{\substack{k=1 \\ \sigma^k_{true}<\sigma^k_{pred}}}^{n}(\lambda_i - 1)\left(\sigma^k_{pred} - \sigma^k_{true}\right)^2 + \sum_{\substack{\mathrm{k=1} \\ \sigma^k_{true}\geq\sigma^k_{pred}}}^{n}\lambda_i\left(\sigma^k_{pred} - \sigma^k_{true}\right)^2\right] \tag{B.5}$$

where λ_i, $i = 1, ..., 3$, are the chosen quantiles for the three groups of the stress data and have values between 0 and 1. The quantile loss function is

an extension of the MSE that has the quantile $\lambda_i = 0.5$.

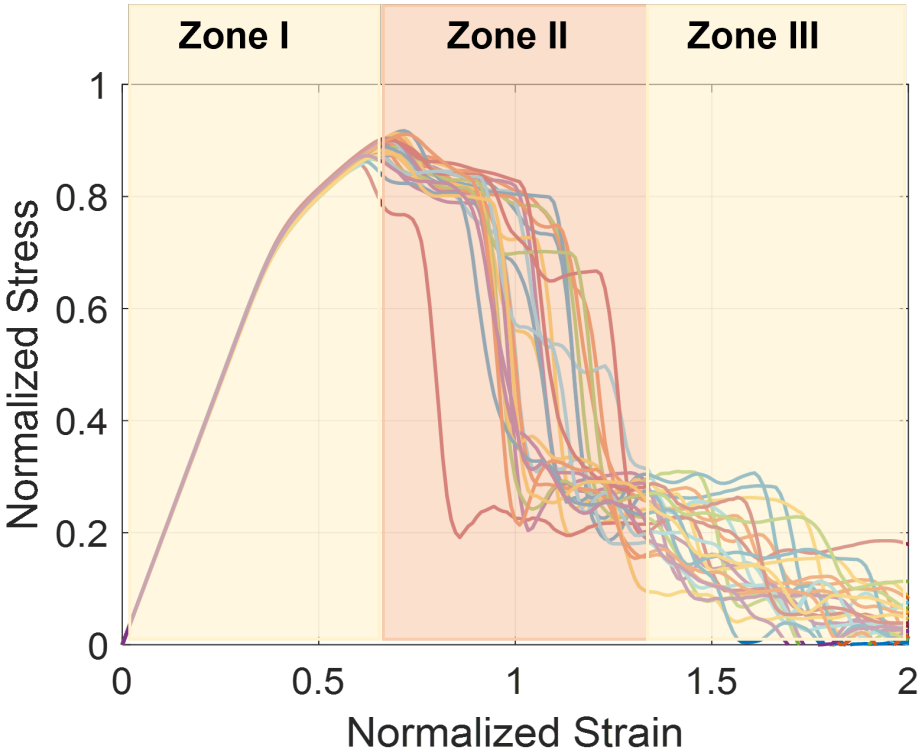

Figure B.2: Three zones in the stress-strain relation for the QTM samples under uniaxial tension.

B.1.3 ANN Optimisation algorithm

Adaptive Moment Estimation (Adam) [205] is a widely used gradient descent-based backpropagation optimisation algorithm. In our study, this algorithm was used to train ANN models. For each parameter, the algorithm computes adaptive learning rates. It keeps an exponentially decaying average of previously squared gradients $\boldsymbol{\upsilon}_t$, like Nesterov's accelerated gradient method [206], MaxProp [207], and others. However, it differs in the way it updates an exponentially decaying average of past gradients:

$$\begin{aligned} \boldsymbol{\zeta}_t &= \omega_1 \boldsymbol{\zeta}_{t-1} + (1-\omega_1)\, g_t, \\ \boldsymbol{\upsilon}_t &= \omega_2 \boldsymbol{\upsilon}_{t-1} + (1-\omega_2)\, g_t^2, \end{aligned} \tag{B.6}$$

where g_t the gradient; $\boldsymbol{\zeta}_t$ and $\boldsymbol{\upsilon}_t$ are approximations of the gradient's first moment (the mean) and second moment (the non-centred variance) at tth step. To compensate for moments that are biased towards zero, bias-corrected first and second moment estimates are computed:

$$\begin{aligned} \hat{\boldsymbol{\zeta}}_t &= \frac{\boldsymbol{\zeta}_t}{1-\omega_1^t} \\ \hat{\boldsymbol{\upsilon}}_t &= \frac{\boldsymbol{\upsilon}_t}{1-\omega_2^t} \end{aligned} \tag{B.7}$$

Eventually, parameters are updated according to:

$$\boldsymbol{\theta}_{t+1} = \boldsymbol{\theta}_t - \frac{\chi}{\sqrt{\hat{\boldsymbol{\upsilon}}_t} + \epsilon}\hat{\boldsymbol{\zeta}}_t \tag{B.8}$$

Where ω_1, ω_2, χ, and ϵ are the algorithm hyperparameters and are subject to tuning.

B.1.4 ANN architecture - hyperparameters

In this section, I have given the hyperparameters used to train our ANN model. Each ANN model received a total of 1000 training iterations. The initial learning rate, χ, is 0.0009. It decreases by the factor 0.2427 when no training progress is made for 18 consecutive training epochs. The other optimiser hyperparameters were used as their default settings in MATLAB: $\omega_1 = 0.9$, $\omega_2 = 0.999$, and $\epsilon = 10^{-8}$ Early stopping was used for deep learning to stop training if the change in learning metrics did not exceed over ten consecutive training iterations. A batch size of 16 was used to train the networks. The hyperparameters to tune the neural networks are obtained using Bayesian optimisation from MATLAB ('bayesopt') [174].

B.1.5 ANN architecture analysis

To demonstrate an example of the improvements in the ANN architecture using our custom built loss function. The ANN model was analyzed based on hyperparameters mentioned above for the three loss functions mentioned in Eqs. B.3 to B.5. The geometries of 5000 QTM samples were used with irregularity, $\alpha = 0.2$, at constant relative density $\bar{\rho} = 0.2$. I used an ANN architecture consisting of 7 hidden layers with $4096, 2048, 1024, 1024, 1024, 512$, and 512 neurons, in sequence from input to output layers in our architecture. Further increase in hidden layers did not show any improvement in the efficiency of deep learning process. The dataset was split into three sub-datasets 75% for training, 15% for validations and 15% for tests. The evaluation of the three loss functions mentioned in Eqs. B.3 to B.5 are presented in the Fig. B.3 based on the training and validation datasets. It can be observed that, our custom-built loss function ($\lambda_1 = 0.5, \lambda_1 = 0.45$ and $\lambda_3 = 0.1$) has minimum loses compared to the other two loss functions (Eqs. B.3 and B.4).

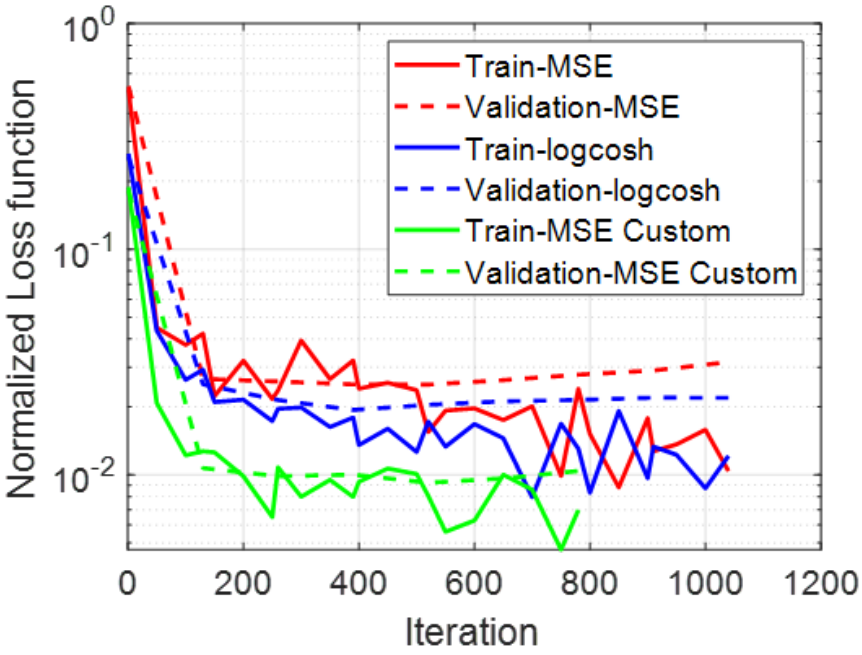

Figure B.3: The effects of loss functions on deep learning rate, which shows that the costom built loss function has the best performance.